Winter 2005

Sensing the human alpha rhythm using a non-contact electroencephalographic (EEG) electrode

Wayne J. Smith II.
University of New Hampshire, Durham

SENSING THE HUMAN ALPHA RHYTHM USING A NON-CONTACT ELECTROENCEPHALOGRAPHIC (EEG) ELECTRODE

BY

WAYNE J. SMITH, II

B.S., University of New Hampshire, 1986
M.S., University of New Hampshire, 1998

DISSERTATION

Submitted to the University of New Hampshire
in Partial Fulfillment of
the Requirements for the Degree of

Doctor of Philosophy
in
Electrical and Computer Engineering

December, 2005

To

My wife, Briceida

and

My son, Ean Wesley Smith, born on March 25, 2005

ACKNOWLEDGEMENTS

Many thanks go to my advisor and friend, Dr. John R. LaCourse, for his personal and professional support during my PhD years. I would also like to thank my other committee members who dedicated time from their busy schedules to offer advice and to review this dissertation. Many thanks also go out to the department technician, Adam Perkins, and to the department secretary, Kathy Reynolds, for always being helpful.

TABLE OF CONTENTS

LIST OF TABLES

LIST OF FIGURES

ABSTRACT

MEASUREMENT OF THE HUMAN ALPHA RHYTHM USING A NON-CONTACT ELECTROENCEPHALOGRAPHIC (EEG) ELECTRODE

by

Wayne J. Smith, II

University of New Hampshire, December, 2005

The electroencephalogram is the recording of bioelectrical potentials on the scalp due to neural current sources in the brain and are typically recorded using wet surface electrodes that make ohmic contact with the scalp surface using an electrolyte gel. Unfortunately, wet electrodes are intrusive to the user, problematic for EEG studies requiring high spatial resolution, and are unsuitable for long-duration EEG recordings. Wet electrodes ultimately limit spatial resolution since the gel can short neighboring electrodes. They also do not meet long-duration recording demands since the gel can dry out over time.

This dissertation explores the feasibility of measuring the EEG at room temperature, through hair, without scalp contact using two capacitive probe techniques. This is achieved by focusing on measurement of the alpha rhythm, an oscillatory EEG signal that is common among the population and is easily elicited with eye closure. Research results suggest that it is possible to sense the alpha rhythm within 4.0mm of scalp-probe spacing and that the ultra-high impedance fieldmeter probe technique is the most promising. Non-contact recordings are compared to wet electrode recordings and issues related to hair and motion artifact are discussed. Areas critical to the development of this technology are suggested.

CHAPTER I

INTRODUCTION

1.1 Surface Electrodes for Bioelectrical Measurement

Bioelectrical measurement refers to the recording of electrical signals in a biologic system due to electrophysiological events. Many signals from the human body can be recorded on the body surface and are of diagnostic significance. These signals originate from muscle and nervous tissue and include the electroencephalogram (EEG), electrocardiogram (ECG), and electromyogram (EMG). The ability to measure these signals is made possible by sensors or electrodes on the body that serve to transduce ionic current into electronic current for external amplification. These electrodes are more specifically referred to as surface electrodes to distinguish them from invasive types.

Surface electrodes are classified as "wet" or "dry". Wet electrodes are metal disks that rely on making adequate ohmic contact to the body with an electrolyte gel(sometimes called a "saline bridge"). Dry electrodes are placed directly on the skin without an electrolyte gel. The transducing mechanism for dry electrodes depends on whether or not they are insulated. A dry **non**-insulated electrode is a metal disk with direct contact to the skin. In this case, as with a wet electrode, a metal/electrolyte interface still exists (electrolyte in skin perspiration) creating an ohmic contact with the body but the electrode resistance is substantially higher. With an insulated electrode, there is no metal/electrolyte interface. Instead, a surface oxide film (dielectric) is grown on the metal. These electrodes are capacitive in nature and rely on the displacement of charge as opposed to the conducted charge in the wet and non-insulated types.

Both wet and dry electrodes may be passive or active. The distinguishing characteristic of active electrodes is that electronic amplification is located at the sensing site. Wet electrodes are usually passive. Dry electrodes, on the other hand, are always active due to the high electrode impedance. This high source impedance requires a high impedance amplifier which can be problematic if placed away from the recording site. Diagrams of dry insulated and non-insulated electrodes are shown in figure 1.1. A summary and scientific comparison of wet, dry and insulating electrodes may be found in the literature [1].

This research embodies insulated electrode technology. More specifically, it is an investigation into a high-sensitive, **non-contact** type of electrode. In principle, no contact is necessary with the insulated type of electrode since air can serve as a dielectric. The electrode could therefore be referred to as an electric field sensor or perhaps, more appropriately, as a bioelectric-field sensor. The remaining sections of this chapter explain the motivation for non-contact measurement technology, current research in this area, and the specific objectives of this research.

1.2 Motivation for Non-Contact Bioelectrical Measurement

The electroencephalogram (EEG) is the recording of bioelectrical potentials on the scalp due to neuronal current sources in the brain. These potentials are typically measured using wet surface electrodes as described previously. In the past decade, EEG science has seen new and interesting applications which will ultimately require advancement in electrode technology to meet the promising potential of these applications. One area of study is the functional brain mapping of cognitive function. In order to accurately map the cognitive electrical activity over the scalp requires a minimum number of electrodes to avoid spatial

aliasing. Current theoretical and experimental evidence indicates that 128 electrodes should be the minimum [2]. Wet electrode technology ultimately limits electrode density since the gel has the potential to short out neighboring electrodes [3]. The accurate spatial mapping of electrical activity is linked to solutions of the inverse problem which serves to image a 3D source from external surface measurements. The inverse problem of brain imaging (or heart imaging as in the ECG) is highly underdetermined in that the number of unknowns is much more than the number of available sensors so maximizing measurement points improves the solvability of the inverse problem.

In addition to the high electrode count of cognitive studies, many EEG studies require long recording times. Epilepsy monitoring is one example of a long-term EEG recording application. The EEG continues to be the most important diagnostic tool in the management of patients with epilepsy. Of particular importance is the ambulatory EEG that allows the patient to maintain some degree of normal mobility while being monitored for an interictal epileptiform discharge (IED) [4]. In this way, the prolonged EEG recording may increase the ability to detect IED's. Another long-term EEG recording example is alertness monitoring. It is well known that retaining a constant level of alertness is difficult or impossible for operators of automated systems who perform monotonous but attention-demanding monitoring tasks. This can lead to severe consequences for people working as air traffic controllers, nuclear power plant operators, pilots, truck drivers, and many other occupations. The EEG holds promise for alertness monitoring since significant signal changes occur related to alertness and arousal which can be detected in real time [5,6]. EEG biofeedback, or neurofeedback, the process by which one conditions or trains brainwave patterns, is another example. It has been used to treat attention-deficit/hyperactivity disorder, autism, chronic

fatigue syndrome, mood disorders, addictions, and learning disabilities to name a few. A wealth of information on neurofeedback may be found in the Journal of Neuropathy, the official publication for the International Society of Neuronal Regulation[7]. Finally, many laboratories have begun to develop brain computer or machine interface(BCI/BMI) systems that provide communication and control capabilities to people with severe motor disabilities [8,9]. BCI systems would require almost continuous monitoring of brain activity. Wet electrode technology limits the development of these EEG applications requiring long-duration recordings since the required electrolytic gel will dry out over time. The gel could obviously be reapplied but is encumbering to the user.

Of particular importance to the alertness monitoring and communication applications is the issue of user intrusiveness. These are areas where the electrodes would be applied every day and, for obvious reasons, renders wet electrodes practically unusable. Practically, the power plant worker or truck driver is not going to place electrode gel on his or her scalp before work. In fact, driver fatigue has recently received increased attention in the road safety field [10]. However, the consensus is that this technology will not be publicly accepted without advancement in EEG-based electrode technology [11].

In summary, wet electrode technology does not meet the EEG demands of high electrode density, long-duration recordings, and user intrusiveness. Insulated electrode technology has the potential to solve these problems [12-14]. However, current EEG insulated electrodes still require adequate contact with the scalp for sufficient capacitive coupling of the EEG signal and this makes hair a major obstacle for ease of application[12]. Due to the small footprint of these electrodes, an adequate contact force is required which may become uncomfortable over time. This research investigates the potential to measure

EEG signals through the hair to an electrode **without scalp contact**. This would be the ideal electrode since there would be no preparation time and recordings could take place indefinitely. Actually, superconducting quantum interference devices(SQUID) approach this ideal recording method by recording the brain's magnetic field with coils about 2 cm from the scalp[15,16]. The instrumentation, however, is extremely expensive due to the required cryogenic operation of the coils (4^0 Kelvin) and the necessary magnetically shielded rooms. The cost of the entire MEG system, including shielded room, is in the range of $2-$3 million (US)[16]. The shielded rooms and the large liquid helium dewars also make this technology immobile which is not acceptable for the brain monitoring applications outlined above.

1.3 Background Information on Insulated Electrode Technology

Research in insulated electrode technology began in 1969 with several papers being published prior to 1972[17-20]. This research focused on electrocardiogram (ECG) applications and it was demonstrated that high quality ECG recordings could be obtained. No published reports on EEG applications occurred until 1994 when Babak Taheri published his dissertation at the University of California in Davis demonstrating that high quality EEG recordings could be made with an insulated electrode[12]. Two subsequent papers were published following his dissertation [13, 14]. He was subsequently hired as a consultant with Electrical Geodesics, Inc.(EGI) to commercially develop this technology [21,22]. The EGI insulated electrode is 5mm X 5mm and supports four recording sites of $1.5mm^2$ in area. The four sites are used to assure that at least one of them is making adequate contact with the scalp. A silicon nitride (relative permittivity = 8) layer of 0.8um in thickness is deposited on the electrodes to obtain capacitance values between 150 and 300 picofarads. EGI is the world

leader in high-resolution EEG measurement. They manufacture the geodesic sensor nets (GSN 200 & HydroCel GSN) which are dense electrode array caps consisting of up to 256 wet electrodes (See Figure 1.2) [21]. For recordings of up to 2 hours, application and clean-up time is only about 30 minutes for an experienced individual. For recordings up to 8 hours, cleanup time increases due to the type of electrolyte utilized. For recordings up to 12 hours, individual filling of electrodes is required dramatically increasing application time [23].

The first publication on non-contact bioelectrical measurement occurred in 1991 from the University of Sussex in England [24]. They used a high-impedance voltage probe to record the ECG at 2 cm and 5 cm from the chest. It is difficult, however, to determine from the traces as to whether or not the presumed ECG signal is induced by motion artifact. This group continues to conduct research in this area [25-29]; their most recent report, associated with non-contact EEG measurement, being published in October 2002[27]. In the same year, this group also published results showing non-contact ECG recordings at 5 cm, 30 cm and 1 m from the body [29]. The significance of this paper is that the authors also included an additional SaO2 recording along with the ECG recordings that hints of the 30 cm and 1 m recordings as being artifact induced.

A novel optical technique of non-contact bioelectrical measurement is being explored at SRICO, Inc. [30-33]. The optical electrode or Photrode™ employs an integrated Mach-Zehnder Intensity electro-optic modulator (interferometer) to detect the ECG through clothing (non-contact) or the EEG with dry skin contact. The basic Photrode™ system and a schematic of the Photrode™ device can be seen in figures 1.3 and 1.4. The Photrode™ receives light from a source and changes the light intensity in response to a biopotential.

1.4 Objectives of Research and Organization of Chapters

The primary objective of this research is to determine if the EEG can be measured without scalp contact. Secondary to this objective is how the following limiting factors affect the reliability of the measurement: scalp-to-probe distance, environmental noise, motion artifact, and hair.

Chapter 2 introduces the EEG and the applicable non-contact measurement methodologies. It concludes with a description of the low-impedance and high-impedance capacitive probes used in this research. Chapter 3 provides a detailed analysis and design description of the two probes and summarizes the use of the alpha rhythm as the EEG signal of interest. Chapter 4 summarizes the experimental results of the two non-contact methodologies with measurements of the EEG alpha rhythm at 2.5mm, 3.0mm, 3.5mm, and 4.0mm from the scalp. These measurements are compared to a standard silver-silver chloride wet electrode used in typical EEG studies. Chapter 5 concludes this dissertation with a discussion of the limitations for the non-contact methods used and provides some direction for future research.

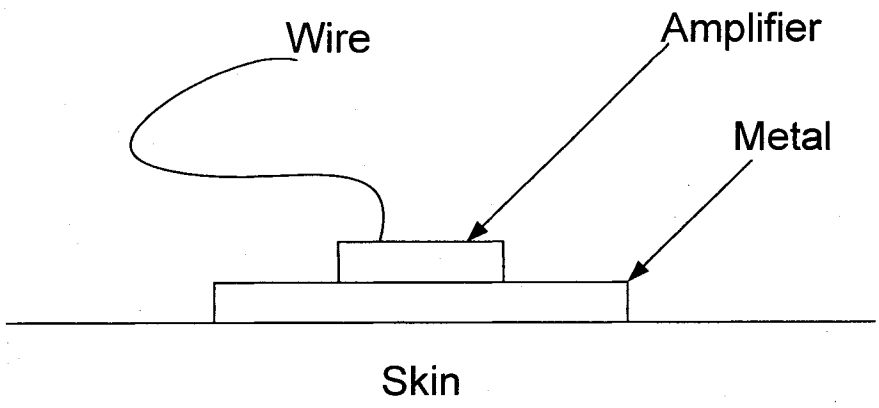

(a)

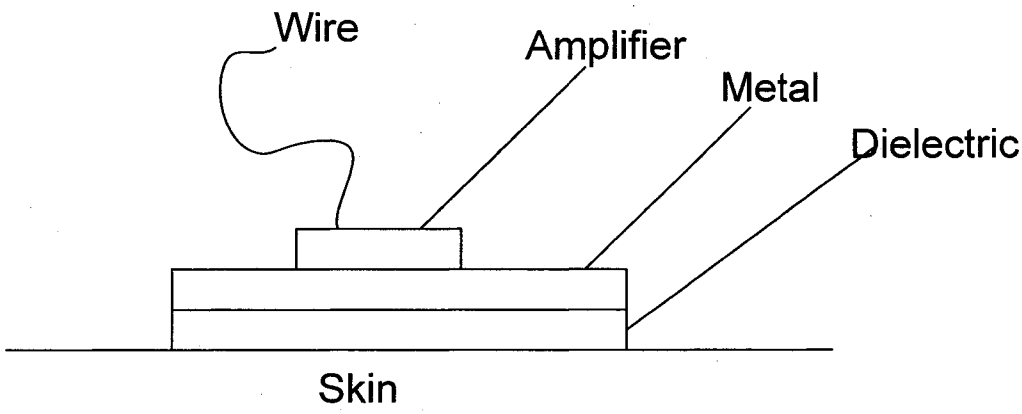

(b)

Figure 1.1 Diagram of (a) Dry Non-Insulated Electrode and (b) Dry Insulated Electrode

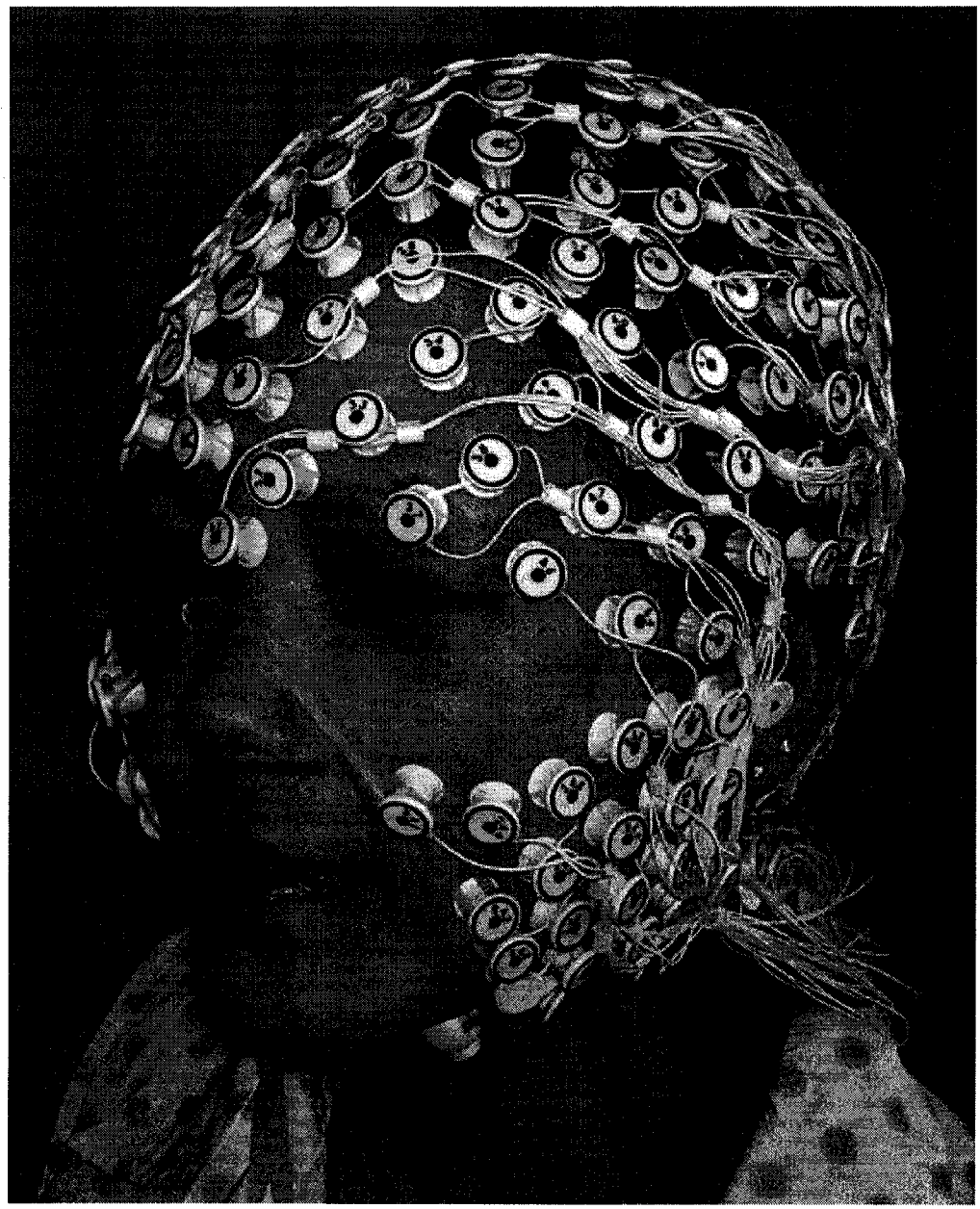

Figure 1.2 Photo of 256 channel Hydrocel Geodesic Sensor Net.
Courtesy of Electrical Geodesics, Inc.

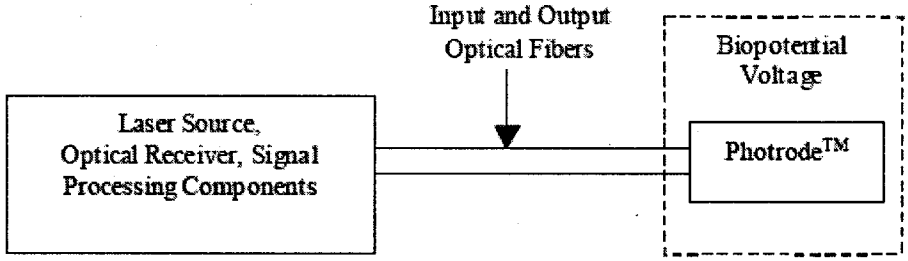

Figure 1.3 The SRICO, Inc. Photrode™ System

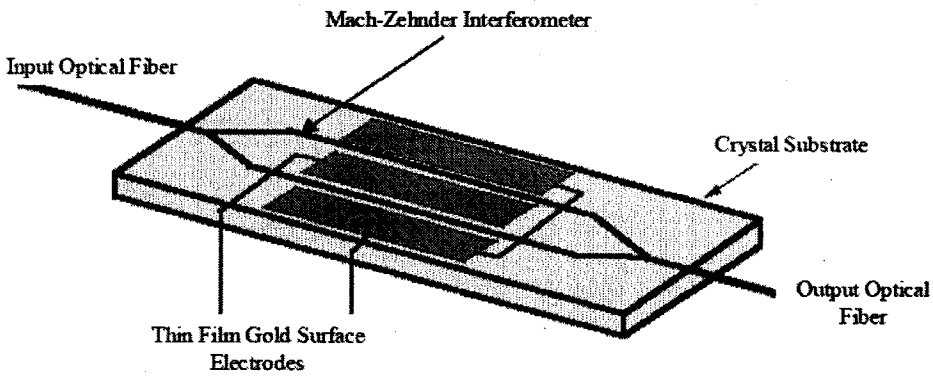

Figure 1.4 The SRICO, Inc. Photrode™

CHAPTER II

EEG AND NON-CONTACT ELECTROQUASISTATIC MEASUREMENT

2.1 Bioelectrical Field Sources of the Brain

Bioelectrical and biomagnetic fields of the brain are generated by ionic current sources from neurons in the cerebral cortex. These current sources arise due to cell membrane permeability changes of the neuron upon stimulation. As opposed to the intercellular current that is confined to the cell, the extracellular current flow is free to flow throughout the volume conductor containing the cell bathing media resulting in small potential differences, or alternatively, an electric field, within the volume (See Fig 2.1). The recording of these small potential differences on the surface (scalp) of the head volume conductor is referred to as the electroencephalogram or EEG. The recording of the small magnetic fields due to brain current sources is referred to as the magnetoencephalogram or MEG. A brief description on the neurophysiological basis of the EEG is provided below.

Although neurons throughout the body vary in size and shape, they all have certain features in common. They all have a soma(cell body) where the nucleus is located with two kinds of nerve fibers, dendrites and axons, extending from the soma(See figure 2.2). The dendrites and soma collect incoming information from other neurons in which the dendrites greatly increase the neuron surface area making more space available to receive contacts from other neurons. The dendrites are the primary receptors for the neuron and most of the interneuronal connections are found here. The axon hillock is the junction of the soma and axon which serves as the trigger zone for the nerve action potential (described below). The axon, emerging from the soma at the axon hillock, is specialized to carry the action

potential away from the soma and may develop collaterals to make contact with more cells [34, 35].

The flow of information between neurons is conveyed by two types of brief changes to the resting membrane potential: the action potential and the postsynaptic potential. The different spatial and temporal characteristics of these two events are important to the discussion of EEG. Any type of stimulation may alter the resting membrane potential of the neuron creating a hyperpolarized or depolarized effect. If this transmembrane potential is sufficiently depolarized to a certain threshold, an action potential or impulse will be initiated at the axon hillock and propagate down the axon. The principal membrane property in action potential generation is the voltage gated sodium channel which upon activation creates a membrane permeability change allowing sodium ions to enter the cell. This will further depolarize the membrane and more sodium channels will open. This continues in a positive feedback manner until all the voltage gated sodium channels have opened. Within a fraction of a millisecond, these same sodium channels close and voltage gated potassium channels open allowing an outward diffusion of potassium ions resulting in a rapid repolarization process of the cell membrane. This whole process lasts about 1 to 2 milliseconds and creates an action potential magnitude of approximately 110 mV. The active site of current flow on the membrane will depolarize adjacent portions of the membrane due to local transmembrane current flow causing these portions to change from a passive site of current flow to an active site of current flow with activation of the voltage gated channels. This new active site of current flow will again depolarize adjacent regions and the cycle is repeated. This regenerative process allows the action potential to be conducted down the entire length of the axon in an all-or-none fashion without a decrease in amplitude. Figure 2.3 shows the

propagation of membrane depolarization and repolarization during an action potential. Note that the active current site moves and the local current loop is confined to this active site.

When an action potential reaches the end of the axon at the presynaptic terminals, the impulse is transmitted to the dendritic or somal membrane of the post-synaptic neuron through the synapse(figure 2.2b) causing local conductance changes on the post-synaptic neuron at the synapse site. This results in a depolarization or hyperpolarization of the postsynaptic membrane called the postsynaptic potential(PSP) which will increase or decrease a neurons ability to generate an action potential and is accordingly referred to as an excitatory postsynaptic potential(EPSP) or an inhibitory postsynaptic potential (IPSP). As opposed to the propagation of the action potential which is a local phenomena of the axon membrane due to active membrane permeability changes, the postsynaptic potential occurs over the entire soma and dendritic membranes due to passive membrane properties (See Figure 2.4). This spatial characteristic of postsynpatic potentials plays an important role in the summation of EPSP's and IPSP's. A typical neuron has many synapses on the dendritic and soma membranes and it is the summation of the excitatory and inhibitory effects on the membrane that determines if the transmembrane potential at the axon hillock has reached the threshold necessary to trigger an action potential. Postsynaptic potentials generally vary from 10-250 msec with an amplitude of 0.1 to 10 mV. The postsynaptic potential is the primary current source of the EEG and to further characterize its importance, a basic understanding of brain anatomy and neocortical structure is necessary. The reader interested in more detail on neurophysiology is referred to the literature[36,37].

The three primary divisions of the human brain are the cerebrum, brainstem, and cerebellum which occupy the cranial cavity of the skull and are surrounded by meninges

and cerebrospinal fluid for protection(See figure 2.5a). The cerebrum, the largest structure of the mature brain, is divided into two equal halves called cerebral hemispheres which are connected by a bridge of nerve fibers called the corpus callosum (See figure 2.6a). The outermost layer of the cerebrum, the cerebral cortex or neocortex, is about 2 to 5 mm thick. It is also often referred to as "gray matter", so called because of the predominance of cell bodies. The neocortex is highly convoluted and folded, consisting of sulci(grooves) and gyri(bulges between sulci), dramatically increasing the overall surface area of this structure inside the head. The neocortex is divided into four lobes, named after the bones of the skull that overlie them(See figure 2.5b). In general, the frontal lobe is largely concerned with the planning for future action and with the control of movement, the parietal lobe with somatic sensation, the occipital lobe with vision, and the temporal lobe with hearing as well as aspects of learning, memory and emotion. Just beneath the cerebral cortex are masses of "white matter", so called because of the predominance of myelinated nerve fibers(axons). These fibers connect neuron cell bodies of the neocortex with other parts of the nervous system[38].

The neocortex contains several different types of nerve cells that fall into two major classes: pyramidal and stellate (star-like). Recent estimates suggest that approximately 85% of cortical neurons are pyramidal cells[39]. Pyramidal cells tend to occupy cylindrical volumes and are characterized by axon and apical dendrites aligned perpendicular to the cortical surface. Stellate cells occupy more spherical volumes and are characterized by dendrites surrounding the cell body(See figure 2.6b)[40]. Recall that, as opposed to the action potential, the postsynaptic potential is distributed over the entire dendritic and soma membrane. If this concept is applied to these two classes of cells, an open field that is dipole

in nature and a closed field can be represented [41]. The open field potential due to the pyramidal cell is far more reaching than the closed field of the stellate cell and is a likely candidate for extracellular currents on the scalp. Of course, these dipole-like sources may be considered radial or tangential depending if the source lies in the gyri or sulci of the cortex. Although scalp currents due to cortical dipoles are confined to the conductive head, the electric field extends outside of the head into the non-conductive air. Figure 2.7 is a simulation of this situation with a steady dipole source located just beneath the head surface.

In an attempt to measure the extracellular field of the pyramidal cell on the scalp, we might consider what the magnitude would be with a sensor that is 1 cm from the cortical surface(through cerebrospinal fluid and scalp). If a single pyramidal cell is modeled as a dipole which is valid at a distal recording point, the signal magnitude could be expected to fall off with the square of the distance. If, for example, a voltage of 100uV was measured at the cortical surface approximately 1 mm from the dipole of interest, we should expect a potential of 1 uV at 1 cm. This, however, contradicts experiments that show a reduction of 1/3 to 1/2 of the magnitude at the cortical surface[42,43]. It is obvious that the single dipole source is an incorrect model for the EEG current source and that this problem should be reexamined with the realization that we are actually recording the summation of extracellular currents from billions of brain cells. Furthermore, with the strong interconnectivity of pyramidal cells, many can also be synchronously active. In other words, we are really looking at the summated longitudinal(parallel to main axes of cells) PSP field components of a synchronously active pyramidal cell population distributed over an area of cortex which more closely resembles a dipole layer. The reduction in magnitude with distance from a dipole layer is much less than a single dipole. This theoretical model is consistent with

experimental results that indicate a 1/3 to 1/2 reduction in magnitude from cortex to scalp and that several square centimeters of cortical surface must be synchronously active for the same potentials to be recorded on the scalp without averaging. The ratio of scalp-to-cortical recorded potentials for various dipole layer areas has been theoretically developed by Nunez[44]. In general, the action potential contributes little to EEG signals for two reasons: First, the depolarized portion of membrane caused by an action potential at any instant of time is small which attenuates with distance more rapidly than the PSP occurring over a large portion of the membrane. Secondly, the short duration of action potentials(1-2 msec) tend to overlap much less than longer duration PSP's(10-250msec)[45].

The electrical activity of the brain is divided into two categories: spontaneous potentials and evoked potentials. Spontaneous potentials represent the continuous activity of the brain. Evoked potentials represent brain activity elicited by a certain stimulus (visual, auditory, somatic) or response (motor activity). Detection of evoked potentials is more challenging since they suffer from a low signal-to-noise ratio where spontaneous potentials represent the brain "noise.

The spontaneous EEG typically exhibits oscillatory properties and is often referred to as EEG rhythms or "brainwaves" that are not sinusoidal but stochastic in nature. In general, the normal spontaneous EEG of any particular person has considerable temporal and spatial variability that depends on the person's behavioral state. This state varies from maximum levels associated with maximum cognitive processing, intermediate levels of relaxation and stages of sleep, to a minimum level representing brain death[46]. Spatial variability of the spontaneous EEG is studied by mapping the scalp distribution of amplitude and coherence. Temporal variability is normally quantified by specifying spectral power: delta band

representing 0.5 to 4 Hz activity, theta band representing 4 to 8 Hz activity, alpha band representing 8 to 13 Hz activity, and beta band representing 13 to 30 Hz activity [47]. In general there is a relationship between frequency content and cognitive state of the individual. The delta and theta bands are most prominent during sleep with the delta band more commonly associated with deep sleep stages (stages 3 and 4), moderate to deep anesthesia, and coma. The alpha band is normally associated with relaxed wakefulness. Rhythms in this band are primarily distributed over posterior and central portions of the head and have been found to be associated with the "idling" of many cortical areas. This includes the well known "alpha wave", distributed over posterior regions of the head, which is most evident with eye closure and attenuated with eye opening. It also includes the "mu wave", distributed over central regions of the head, which is attenuated with contralateral movement but unresponsive to eye opening. This attenuation of idling rhythms is often called "alpha blocking" or desynchronization. Attenuation in the alpha band has also been shown to correlate with cognitive load which may be accompanied by changes in intercortical coherency [48, 49]. No neurophysiological theory on the origin of alpha rhythms has yet found general acceptance [50]. The beta band correlates of cognitive state are different with the lower beta frequencies exhibiting a desynchronization with mental activity and higher beta frequencies elicited with mental activity. Beta activity is normally recorded from the parietal and frontal regions of the head.

Typical amplitudes for the spontaneous EEG lie between 10 and 100uV for the adult. In the alpha band, Simonova et. al. found an amplitude distribution between 20 and 60 uV in 66% of subjects; values below 20uV were found in 28% of subjects and above 60uV in 6% of subjects[51]. Higher amplitudes are typically found in association with slower frequencies.

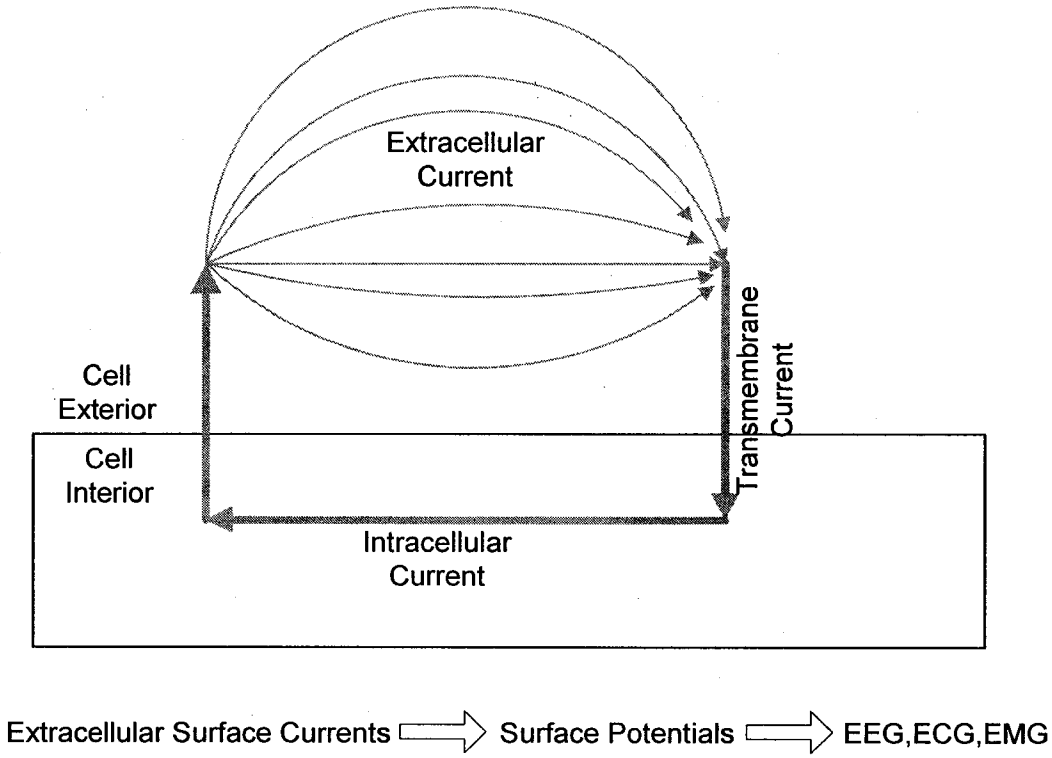

Figure 2.1 Current loop of excitable cell

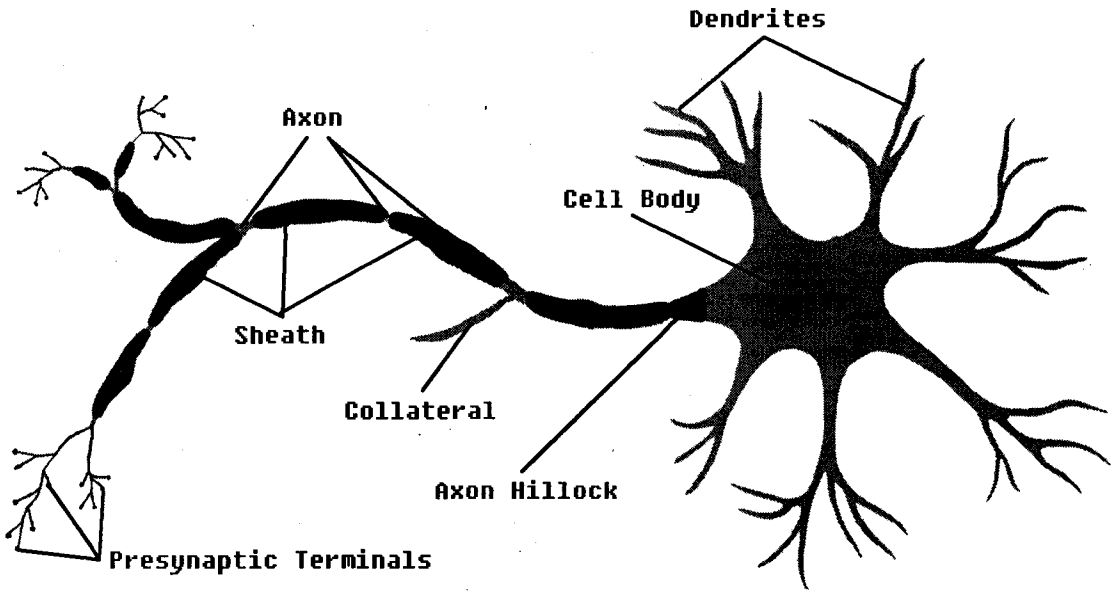

(a)

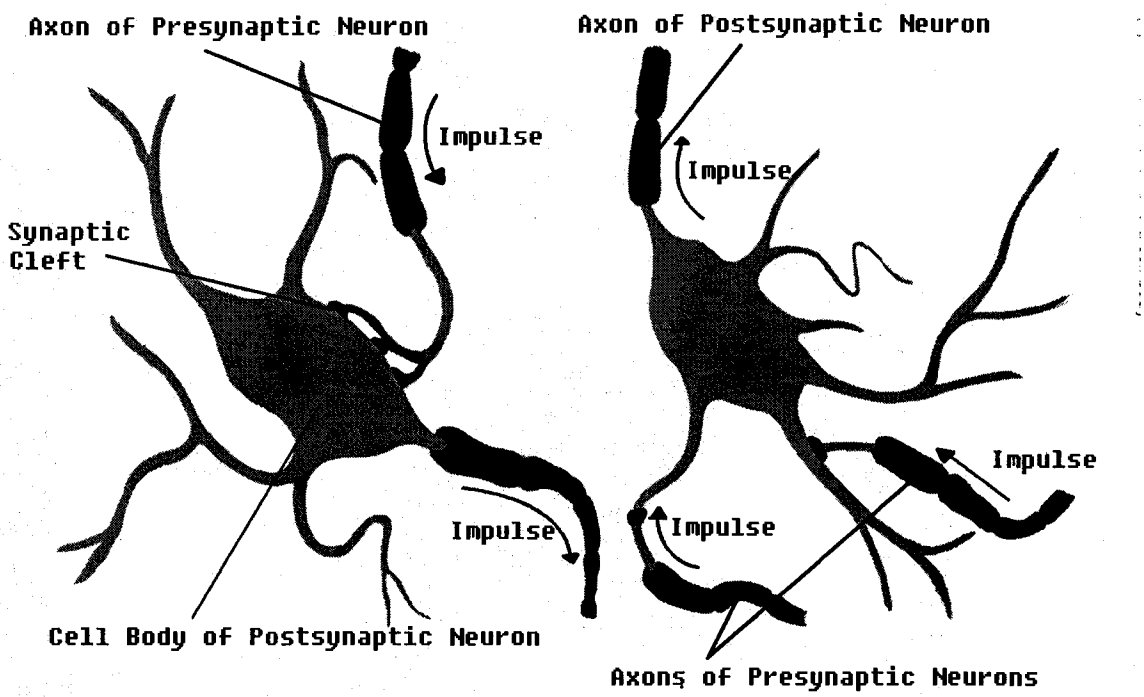

(b)

Figure 2.2 (a) Typical Neuron structure **(b)** Synaptic connections between neurons

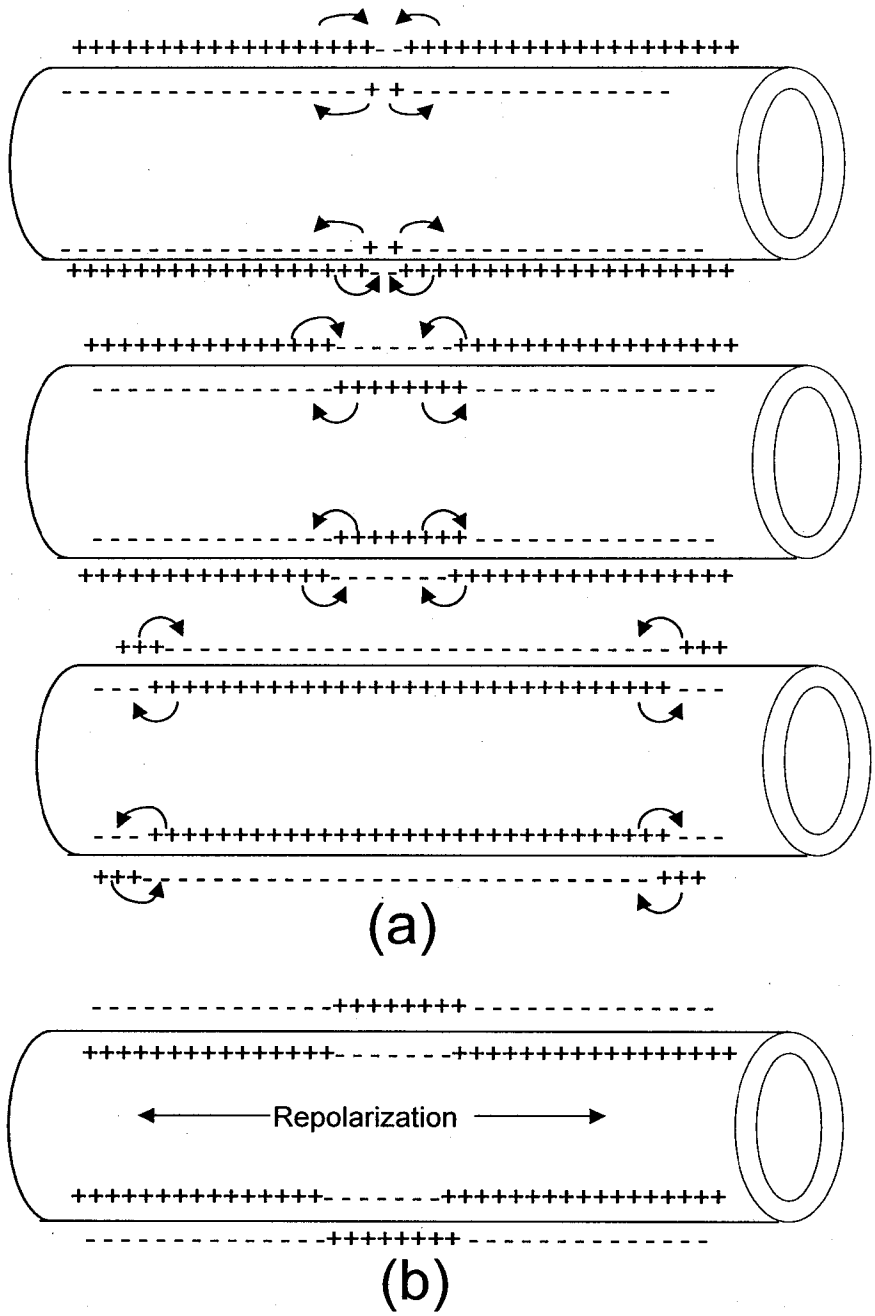

Figure 2.3 **(a)** Propagation of membrane depolarization in both directions due to localized current loops **(b)** Propagation of repolarization process in both directions.

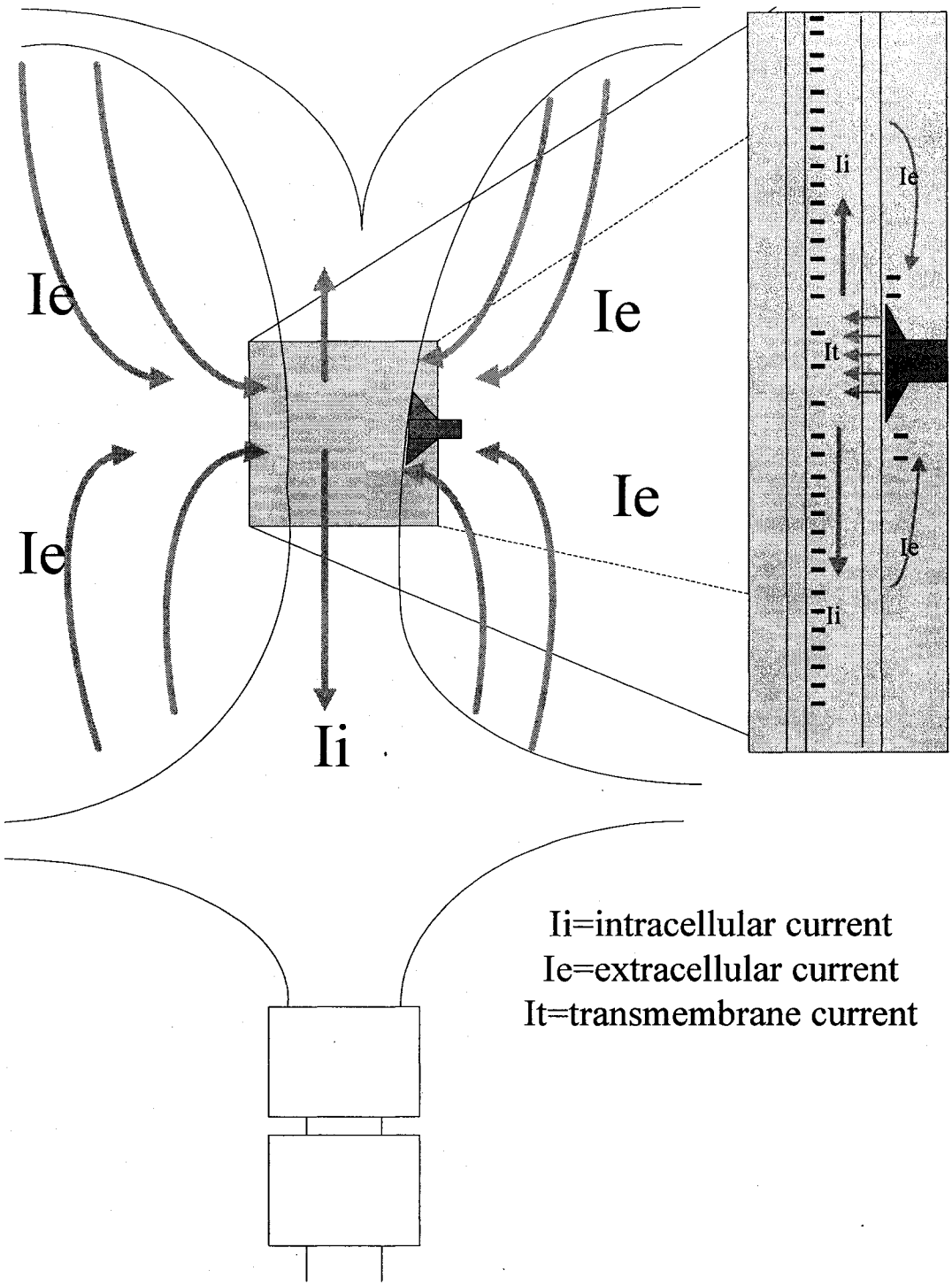

Figure 2.4 Postsynaptic current distribution over soma and dendritic membrane.

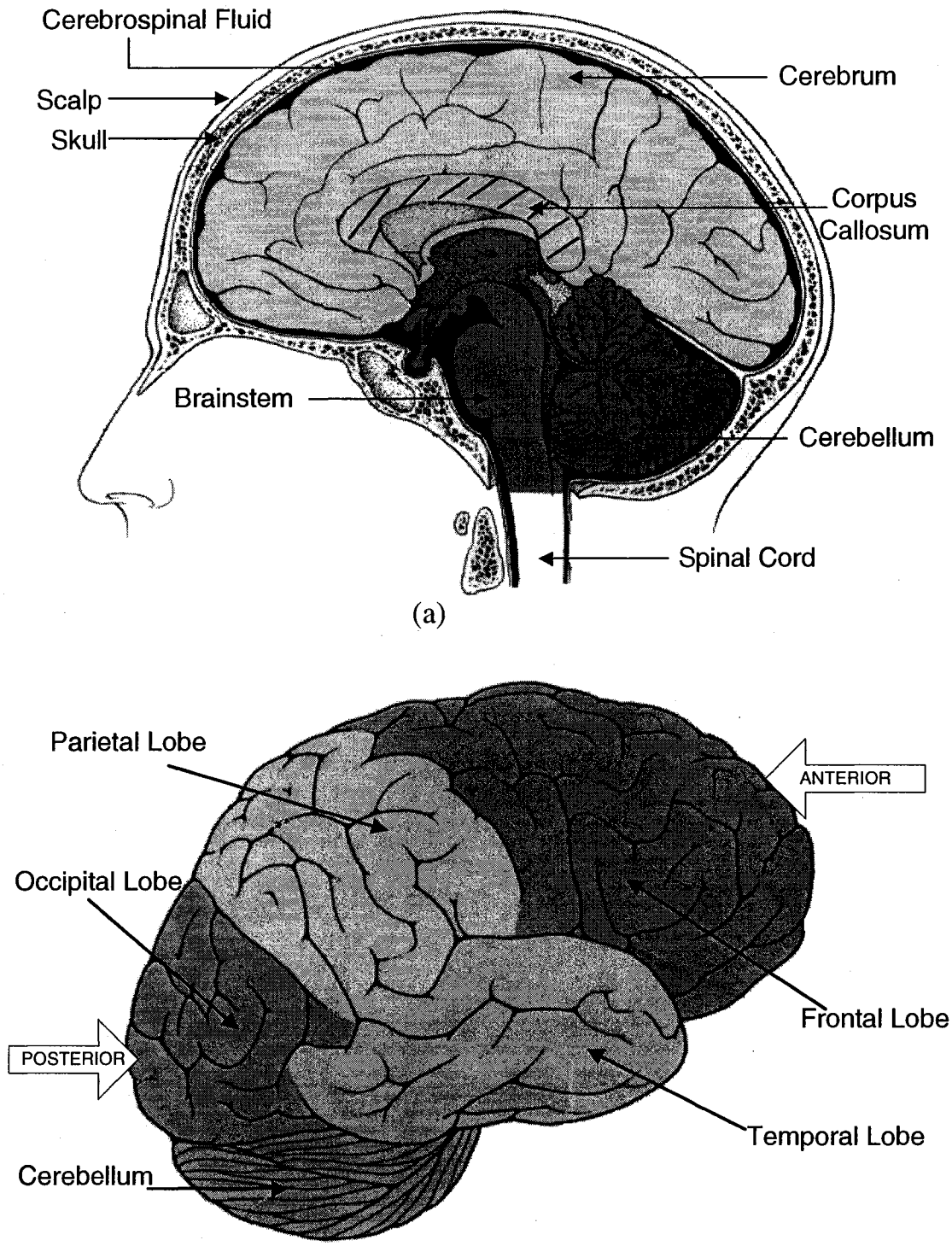

Figure 2.5 **(a)** Medial slice of head **(b)** Lateral view of brain showing primary lobes of cortex. The alpha rhythm of interest is distributed in the occipital lobe region.

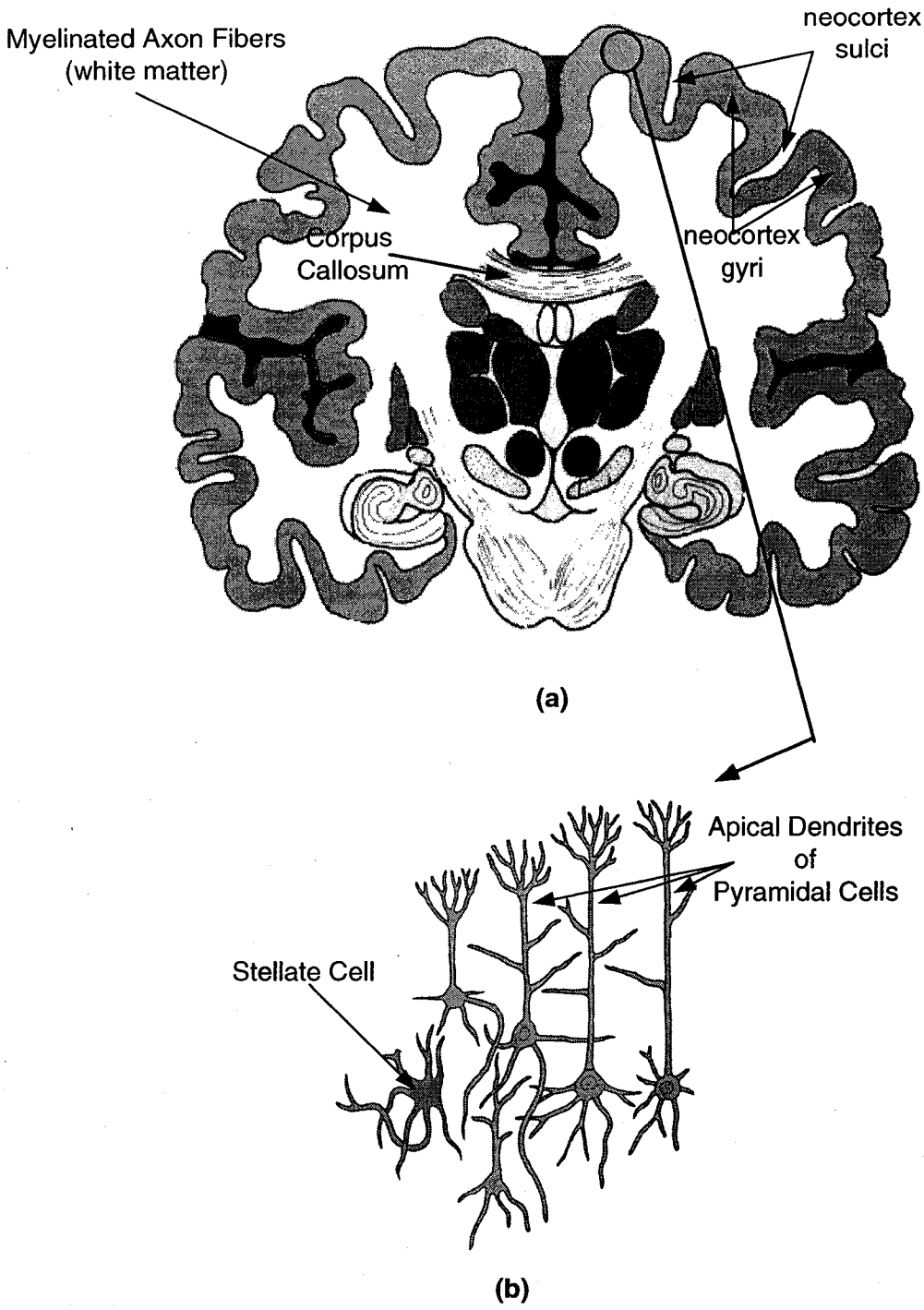

Figure 2.6 **(a)** Transverse section of brain indicating neocortex and white matter **(b)** Section of neocortex showing stellate and pyramidal cell structure. Pyramidal cells are oriented perpendicular to cortical surface.

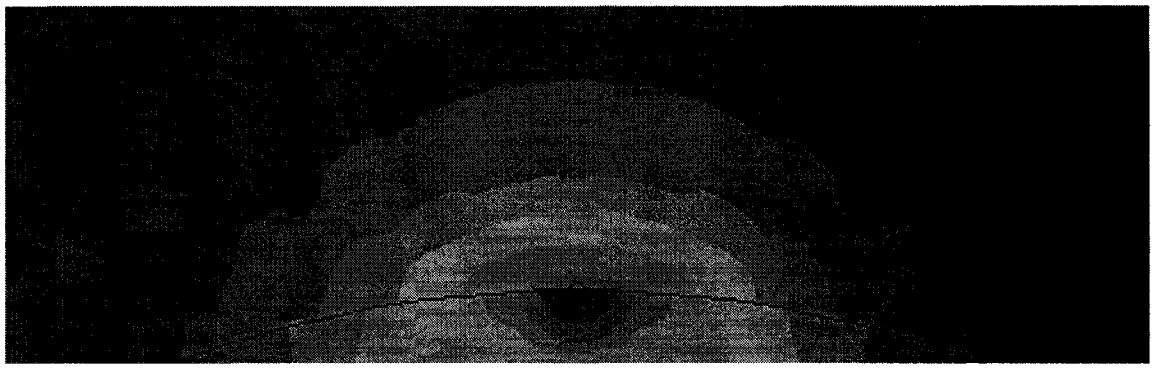

(a)

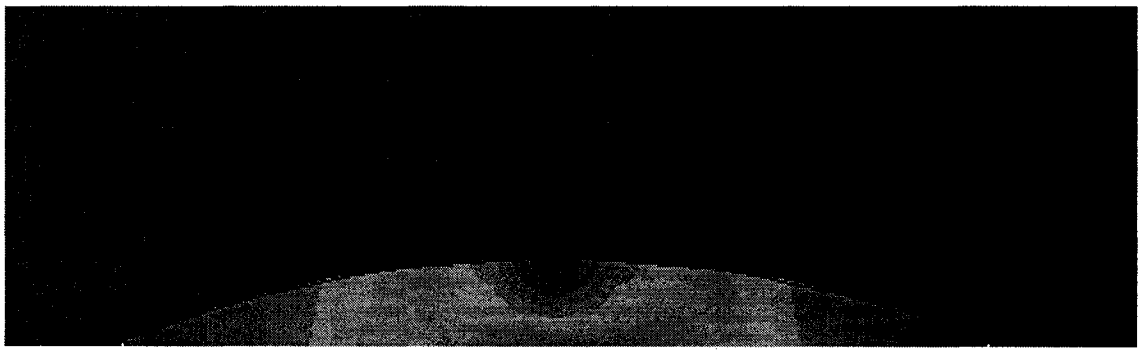

(b)

Figure 2.7 **(a)** Electric field magnitude plot due to a dipole located inside a conductive sphere surrounded by a medium of zero conductivity **(b)** corresponding current density magnitude. Red is minimum and dark green is maximum.

2.2 Non-Contact Electroquasistatic Measurement

Non-contact electroquasistatic measurement refers to the measurement of low-frequency fields and surface charge/potentials without making contact with the source. Surface charge is emphasized where non-contact instrumentation is most applicable as opposed to the measurement of a volume charge distribution. In the literature, electroquasistatic measurement is usually referred to as simply electrostatic measurement with the low-frequency capability implied and the instrument optimized for 0.0 Hz (DC).

Given the associated electric field that is produced by the abundance of positive or negative charge in any particular area, one does not have to make contact with the source but instead can rely on the electric field to make determinations on surface charge/potential or potential in space near the charge. There are three main types of non-contact sensing devices: mechanical types based on Coulombs law, electro-optical methods, and capacitive probe methods.

Coulombs law techniques date back to 1785 when Charles Augustin Coulomb described a torsion balance that he used to prove that charges exert a force on each other and that this force is inversely proportional to the square of the separation distance[52]. This approach is the fundamental principle of the atomic force microscope [53]. A group at Cal Tech has recently designed a nanometer scale mechanical charge detector using Micro-Electrical-Mechanical Systems (MEMS) technology[54].

Electro-optical methods are based on the fact that, in certain transparent solids and liquids, the effective refractive index can be modified by an electric field. The two effects observed are the Pockels effect in crystalline materials and the Kerr effect in dielectric

liquids[55]. The SRICO Photrode introduced in chapter 1 takes advantage of the Pockels effect.

Capacitive probe techniques are based on the charge induction or capacitive coupling principle whereby a source charge and its inherent electric field cause a charge to be induced on a proximal conductor. In the literature, the instrument is often referred to as an induction (charges induced) probe[56]. In figure 2.8, an ellipsoidal conductor is placed in an electric field which is horizontal and uniform. As shown, there are two extreme cases with the conductor floating in figure 2.8a and connected to the reference potential in figure 2.8b. Note in figure 2.8a that the electric field continues on both sides of the conductor due to equal but opposite charges existing on the conductor surface. In this case, the conductor forms an equipotential surface at the potential existing in space. In contrast, the electric field terminates on the conductor in figure 2.8b since it is held at the reference potential. As such, the probe now contains an abundance of charge on its surface. One should see from these two figures that the floating conductor causes minimal distortion of the electric field. However, it should also be noted that complete lack of distortion is impossible with a conductor in an electric field since all field lines terminate at right angles on the conductor surface. Intermediate cases exist between figures 2.8a and 2.8b depending on the resistive path to the reference potential (Note in figure 2.8a we are considering infinite ohms and in 2.8b, zero ohms). Varying resistance causes a time rate of discharge from the probe surface. If the resistance is to low, the probe cannot maintain an equipotential for slowly varying signals. The capacitive probe may be part of a high-impedance circuit, commonly called a buffer, or a low-impedance circuit, commonly called a current-to-voltage converter, as shown in figures 2.9 and 2.10. In these figures, one side of Cs is the source plate and the other side is the

detection plate. For the high-impedance circuit, the current flowing into the positive input is ideally zero and, as such, is usually employed as a field meter since it causes minimal distortion to the e-field. In comparison, the low-impedance circuit, by its very nature, cannot be used as a field meter since the probe potential is forced to be at the reference potential (hence the distinction "low-impedance") by feedback to the negative input of the amplifier which distorts the e-field. It is, however, perfectly suitable as a non-contacting surface voltmeter since a current is established flowing away from the input plate and into C_f creating a voltage. More specifically, a change in potential on the source plate causes the charge on the detector plate to change in order to maintain the reference potential. This flow of charge changes the voltage on C_f from the Q=CV relationship. Practically, both of these circuits will not work at DC, that is, they are not static instruments. There are two reasons for this: DC bias currents of the amplifier and finite impedance. DC bias currents will change the charge stored on the input plate of figure 2.9 and the feedback capacitor of figure 2.10. Finite impedance means that some current will flow into the positive and negative inputs of the amplifiers changing the charge stored. In order for these two methods to be truly static measuring instruments, methods are employed to modulate the input capacitance, Cs, using field mill or vibrating probe techniques [57].

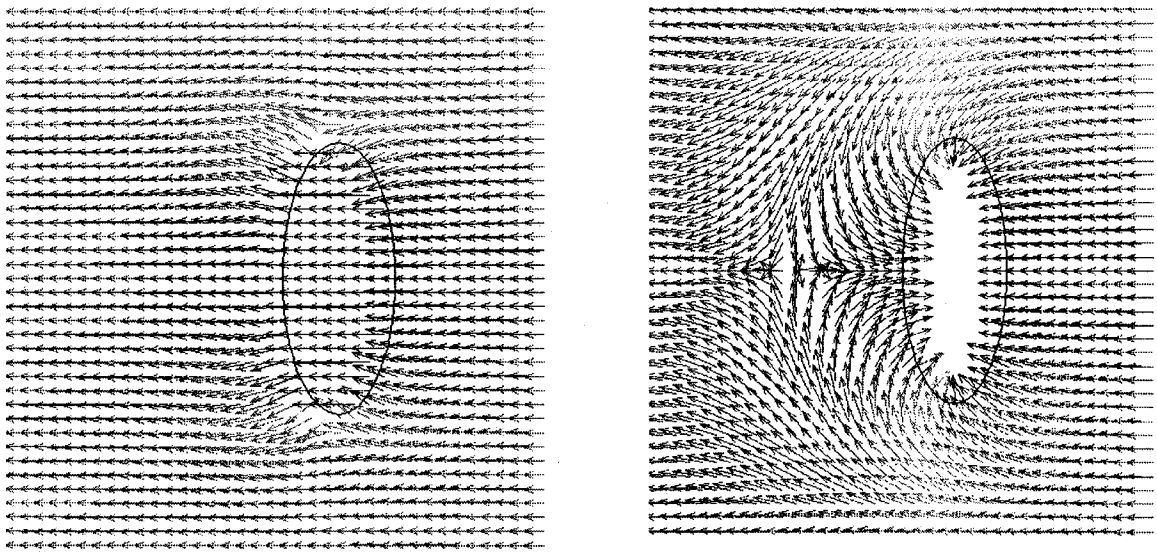

(a) (b)

Figure 2.8 Conductor in electric field (a) floating and (b) tied to reference potential.

2.3 Non-Contact EEG Measurement Using a Capacitive Probe

This research focuses on the use of the two capacitive probe techniques to remotely measure surface charge/ electrical fields due to brain activity. This section provides details of these techniques in regards to signal-to-noise (S/N), bandwidth, and linearity.

The source capacitance of the probe will in general be very small due to the fact that we are using a small probe diameter with an air dielectric. A reasonable value of source capacitance can be obtained noting the limitations on maximum electrode area and maximum distance from the scalp. The maximum electrode *area* is set by the spatial frequency of the EEG. If the electrode area is too large, then spatial resolution is lost and the EEG measurements introduce spatial aliasing. The standard for the spatial sampling of the EEG is 128 electrode sites evenly distributed over the head [58]. Assuming 128 samples, the maximum electrode area is calculated by first determining the average surface area of the

adult head as half of a sphere. Given that the average radius of the adult head is approximately 9 cm [58], an average adult head surface area is

$$1/2 * 4\pi r^2 = 2\pi (8.9\text{cm})^2 = 508\ \text{cm}^2$$

Therefore, the maximum sensor area = $508\text{cm}^2/128=3.97\ \text{cm}^2$. For a circular electrode, since $\pi r^2=3.97\text{cm}^2$, the maximum diameter of the electrode is approximately 2.2cm.

The maximum *distance* from the scalp to the electrode is limited by noise. Less charge is induced on the electrode as we move further from the scalp. Eventually, the small signal charge is below the system noise floor. For example, assume that the electrode is 0.5cm from the scalp, which should allow enough space for hair. The capacitance of this arrangement can be calculated as follows:

$$\varepsilon_0 * \text{area/gap distance} = 8.85\text{e-}12 * 3.91\text{e-}4\text{m}^2/.005\text{m}=0.7\text{pf}$$

Now consider the signal displacement current magnitude, in a certain EEG band, through a purely capacitive source of such low value. Considering that the low-end alpha rhythm amplitude is typically 10uVrms, the signal displacement current through the electrode at 10uVrms and 8 Hz is $(10\text{uV})2\pi(8\text{Hz})(0.7\text{pF}) = 0.35\text{fA}$ rms. This is an extremely low level of current and dictates an extremely low-noise system for the front-end amplifier. The signal-to-noise ratio of the front-end amplifier turns out to be the critical specification and is described more thoroughly below. As discussed in section 2.2, the capacitive probe may be one of two possible configurations: the high-impedance (HI) and low-impedance (LI) probe configurations. Figures 2.10 and 2.11 show the two circuits with voltage and current noise sources included where the voltage noise sources of the differential input stage is replaced by

a single source. Current noise sources related to the – input for the HI probe and the + input for the LI probe have no affect on the output noise level since they are connected to low impedance points. E_n is the voltage noise spectral density and I_n is the current noise spectral density. The derived signal-to-noise expressions are ratios of power spectral densities (S/N_{PSD}) where the noise expression must be integrated over the bandwidth to obtain total noise power.

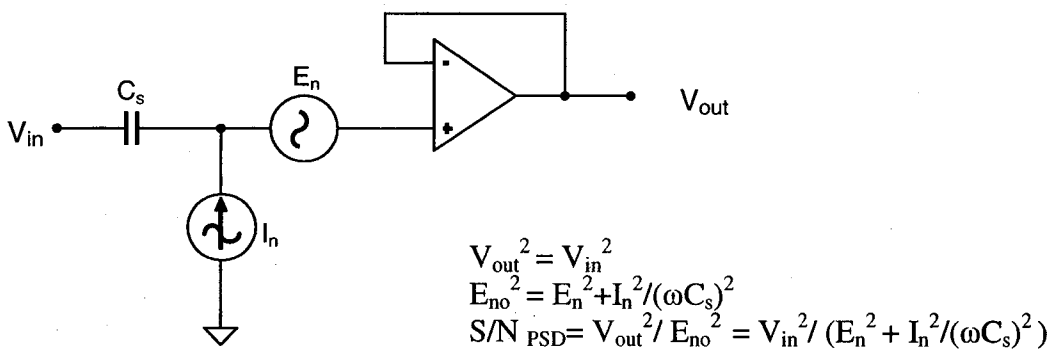

Figure 2.9 High-Impedance Capacitive Probe

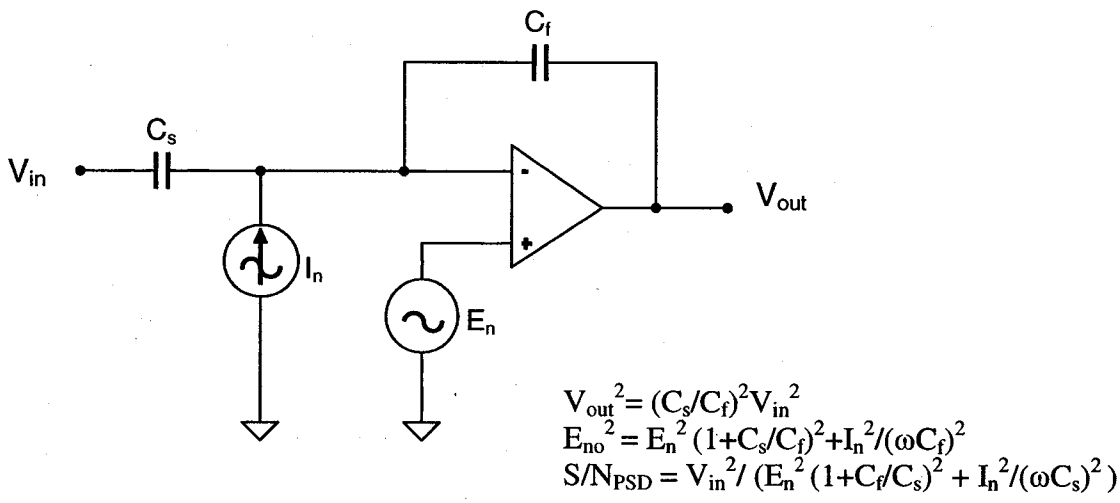

Figure 2.10 Low-Impedance Capacitive Probe

Note that the HI probe has a better S/N ratio because of the voltage noise, E_n. C_f can be made small to maximize the S/N ratio for the LI probe but this will result in a loss of bandwidth as discussed below.

Practically, the circuits of figures 2.9 and 2.10 will not function without some way to set the DC operating point. In order to provide a DC path to the appropriate input, a biasing resistor, R_b, is used as shown in figures 2.11 and 2.12 below. The transfer function for both circuits is also indicated.

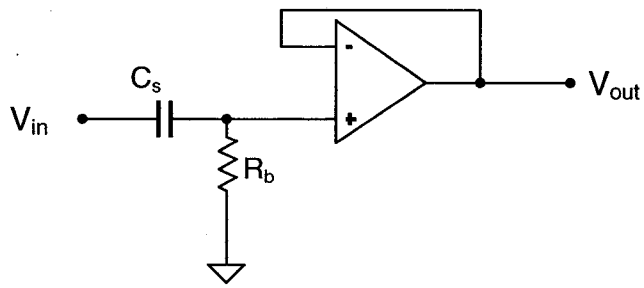

$Vo(s)/Vi(s) = sR_bC_s / (1+sR_bC_s)$
1st order pole at $s = -1/R_bC_s$

Figure 2.11 High--Impedance probe with biasing resistor R_b.

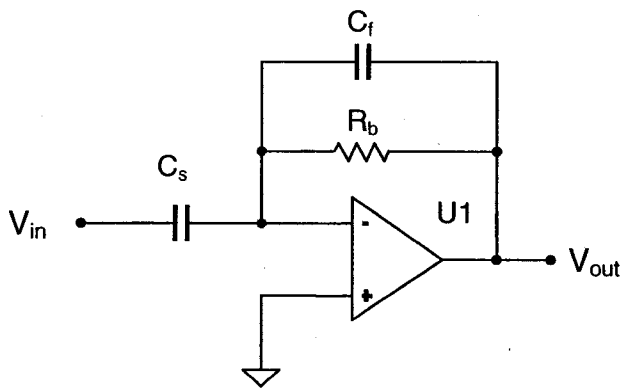

$Vo(s)/Vi(s) = sC_sR_b / (1+sR_bCf)$
1st order pole at $s = -1/R_bC_f$

Figure 2.12 Low-Impedance probe with biasing resistor R_b.

As shown above, the biasing resistor establishes the bandwidth. In the LI case, there is a trade-off between low-noise and bandwidth for C_f. Assuming C_s=C_f, with a range of 0.5 to 1.0 picofarads, an R_b of 320 to 640 gigaohms (Gohms) is required to meet the EEG low-frequency response of 0.5 Hz. This high value of resistance may be obtained with a single resistor or by using feedback (See figures 2.16 and 2.17).

In addition to the high resistance value for the two probes, the extremely low value of source capacitance accentuates problems with parasitic capacitance. In order to obtain a more accurate picture of signal-to-noise ratio, the signal and noise gains must be examined with important parasitic capacitances included in the analysis. Figures 2.13 and 2.14 below show the HI and LI probes with associated parasitic capacitances, amplifier noise sources, and resistor thermal noise sources included where

C_{Rb} is capacitance of resistor R_b

C_{icmn} is the internal op amp common mode capacitance of negative input

C_{icmp} is the internal op amp common mode capacitance of positive input

C_{id} is the internal op amp differential mode capacitance

C_{io} is op amp input-output capacitance

C_g is guard capacitance of the amplifier shield

Note that we are neglecting stray resistances with the op amp because these are typically very high, in the 10^{14} range. Other stray capacitance and resistance related to the circuit board can be minimized with suitable guarding techniques (See below and chapter 3).

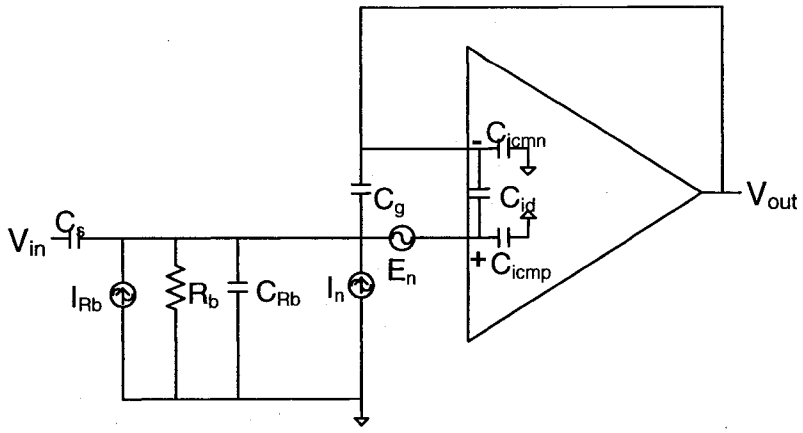

Figure 2.13 High-Impedance Probe with associated stray capacitance and noise sources

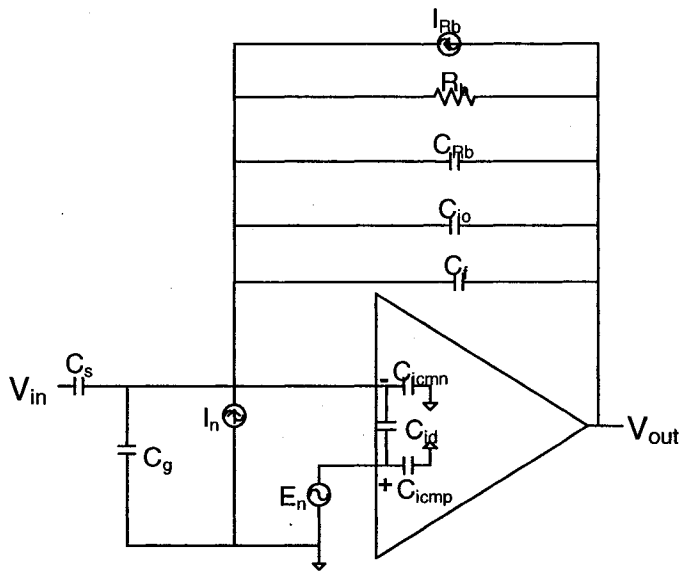

Figure 2.14 Low-Impedance Probe with associated stray capacitance and noise sources

Not all of the stray capacitances associated with the HI and LI probes play a significant role in the signal or noise gains. For the LI case, C_{icmp} is eliminated by the reference connection on the positive input. C_{icmn} is eliminated by the virtual short on the input terminals. For both the HI and LI probes, the C_{id} does not affect the signal due to the virtual short.

Shields (guards) are always used when measuring small signals from high-impedance sources. This is necessary to prevent capacitive coupling of environmental noise to the pick up plate. In general, the primary noise source is 60 Hz power line interference. Figure 2.15 illustrates the principle. As long as a conductor surrounds the pick-up electrode and is driven at a constant potential, no signal can couple to the electrode. As shown in figure 2.15, the shield is driven differently depending on the probe configuration. In both cases, it is driven to minimize loss of signal gain. For the LI probe, the shield is driven at the reference potential. For the HI probe, the shield is driven by the amplifier output. Driving the shield with the amplifier output is referred to as bootstrapping and is a useful technique with an amplifier of unity gain. In both cases, since the potential on both terminals of Cg is the same, no displacement current can flow through C_g and is thus eliminated.

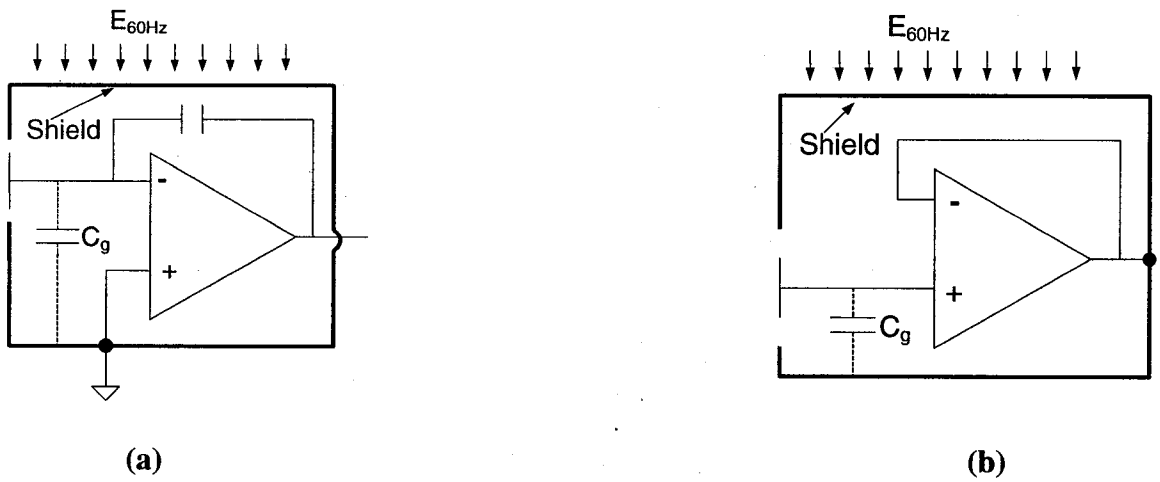

Figure 2.15 Line interference eliminated with shield driven at **(a)** reference potential for LI probe and **(b)** amplifier output for HI probe.

Signal-to-noise power spectral density (S/N_{PSD}) ratios are derived below for the HI and LI probes. It should be noted that the expressions are derived assuming a homogeneous field at the sensing capacitor, C_s .

For the HI probe, the signal output, V_{out}^2, is

$$V_{out}^2 = V_{in}^2 \left| \frac{Z_{in}(s)}{Z_{in}(s) + X_s(s)} \right|^2$$

where $X_s(s)$ is source reactance, $1/\omega C_s$

and Z_{in} is impedance looking into amplifier after C_s

The PSD noise output, E_{no}^2, is

$$E_{no}^2 = E_n^2 + I_n^2 \left| Z_{in}(s) \| X_s(s) \right|^2 + I_{Rb}^2 \left| Z_{in}(s) \| X_s(s) \right|^2$$

Since $Z_{in}(s) = \frac{R_b}{1 + sR_bC_i}$ then $\frac{Z_{in}(s)}{Z_{in}(s) + X_s(s)} = \frac{sR_bC_s}{sR_b(C_i + C_s)}$ where $C_i = C_{Rb} + C_{icmp}$

and the magnitude squared, $\left| \frac{Z_{in}(s)}{Z_{in}(s) + X_s(s)} \right|^2 = \frac{\omega^2 R_b^2 C_s^2}{1 + \omega^2 R_b^2 (C_i + C_s)^2}$

and since $Z_{in}(s) \| X_s(s) = \frac{R_b}{1 + sR_b(C_i + C_s)}$

and the magnitude squared, $\left| Z_{in}(s) \| X_s(s) \right|^2 = \frac{R_b^2}{1 + \omega^2 R_b^2 (C_i + C_s)^2}$

Then the signal-to-noise power spectral density ratio becomes

$$\left(\frac{Signal}{Noise} \right)_{PSD} = \frac{V_{out}^2}{E_{no}^2} = \frac{V_{in}^2 \left(\frac{\omega^2 R_b^2 C_s^2}{1 + \omega^2 (C_i + C_s)^2 R_b^2} \right)}{E_n^2 + I_n^2 \left(\frac{R_b^2}{1 + \omega^2 R_b^2 (C_i + C_s)^2} \right) + I_{Rb}^2 \left(\frac{R_b^2}{1 + \omega^2 R_b^2 (C_i + C_s)^2} \right)}$$

$$= \frac{V_{in}^{\ 2}}{E_n^{\ 2}\left(\frac{1+\omega^2(C_i+C_s)^2 R_b^{\ 2}}{\omega^2 C_s^{\ 2} R_b^{\ 2}}\right) + I_n^{\ 2}\left(\frac{1}{\omega^2 C_s^{\ 2}}\right) + I_{Rb}^{\ 2}\left(\frac{1}{\omega^2 C_s^{\ 2}}\right)}$$

and letting $X_s = 1/\omega C_s$, and $I_{Rb} = \sqrt{4kT/R_b}$

$$\left(\frac{Signal}{Noise}\right)_{PSD} = \frac{V_{in}^{\ 2}}{E_n^{\ 2}\left(\frac{(C_i+C_s)^2}{C_s^{\ 2}} + \frac{1}{\omega^2 C_s^{\ 2} R_b^{\ 2}}\right) + I_n^{\ 2} X_s^{\ 2} + \left(4kT/R_b\right) X_s^{\ 2}}$$

where $C_i = C_{Rb} + C_{icmp}$

For the LI probe, the signal output, $V_{out}^{\ 2}$, is

$$V_{out}^{\ 2} = V_{in}^{\ 2}\left|\frac{Z_f}{X_s}\right|^2$$

The PSD noise output, $E_{no}^{\ 2}$, is

$$E_{no}^{\ 2} = E_n^{\ 2}\left|1 + \frac{Z_f(s)}{X_s(s) + X_i(s)}\right|^2 + I_n^{\ 2}\left|Z_f(s)\right|^2 + I_{Rb}^{\ 2}\left|Z_f(s)\right|^2$$

where $Z_f(s)$ is the feedback impedance given by $Z_f(s) = \frac{R_b}{1 + sR_bC_{ft}}$

and Xs(s) and Xi(s) are, respectively, the source and input reactances given by $1/\omega Cs$ and $1/\omega Ci$ where $C_i = C_g + C_{id} + C_{icmn}$

$\frac{Z_f(s)}{X_s(s)} = \frac{sR_bC_s}{1 + sR_bC_{ft}}$ and the magnitude squared, $\left|\frac{Z_f}{X_s}\right|^2 = \frac{w^2 R_b^{\ 2} C_s^{\ 2}}{1 + w^2 R_b^{\ 2} C_{ft}^{\ 2}}$

$$1+\frac{Z_f(s)}{X_s(s)+X_i(s)}=1+\frac{R_b \Big/ 1+sR_bC_{ft}}{1 \Big/ s(C_i+C_s)}=\frac{1+sR_b(C_{ft}+C_i+C_s)}{1+sR_bC_{ft}}$$ and the magnitude squared

is $$\left|1+\frac{Z_f(s)}{X_s(s)+X_i(s)}\right|^2=\frac{1+\omega^2R_b{}^2(C_{ft}+C_i+C_s)^2}{1+\omega^2R_b{}^2C_{ft}{}^2}$$

Then the signal-to-noise ratio becomes

$$\left(\frac{Signal}{Noise}\right)_{PSD}=\frac{V_{in}{}^2\left(\omega^2C_s{}^2R_b{}^2 \Big/ 1+\omega^2C_{ft}{}^2R_b{}^2\right)}{E_n{}^2\left(\frac{1+\omega^2R_b{}^2(C_{ft}+C_i+C_s)^2}{1+\omega^2R_b{}^2C_{ft}{}^2}\right)+I_n{}^2\left(\frac{R_b{}^2}{1+\omega^2R_b{}^2C_{ft}{}^2}\right)+I_{Rb}{}^2\left(\frac{R_b{}^2}{1+\omega^2R_b{}^2C_{ft}{}^2}\right)}$$

$$=\frac{V_{in}{}^2}{E_n{}^2\left(\frac{1+\omega^2R_b{}^2(C_{ft}+C_i+C_s)^2}{\omega^2R_b{}^2C_s{}^2}\right)+I_n{}^2\left(\frac{1}{\omega^2C_s{}^2}\right)+I_{Rb}{}^2\left(\frac{1}{\omega^2C_s{}^2}\right)}$$

$$\boxed{\left(\frac{Signal}{Noise}\right)_{PSD}=\frac{V_{in}{}^2}{E_n{}^2\left(\frac{(C_{ft}+C_i+C_s)^2}{C_s{}^2}+\frac{1}{\omega^2R_b{}^2C_s{}^2}\right)+I_n{}^2X_s{}^2+\frac{4kT}{R_b}X_s{}^2}}$$

where $C_i=C_g+C_{id}+C_{icmn}$.

The noise expressions in the denominator of the above S/N PSD equations for both probes are composed of three terms: the voltage noise term associated with E_n, a current noise term associated with I_n, and a thermal noise term associated with $4kT/R_b$. Note the similarities of the two above signal-to-noise expressions for the LI and HI probes. The

difference lies in the multiplication of the voltage noise, E_n. Note that if C_i=0 for both amplifiers (no parasitic capacitance) and if C_{ft}=0 for the LI probe, then the S/N is the same for both probes. However, this is not reality since shields must be used to eliminate interference and some feedback capacitance (C_{ft}) is necessary for stability. Therefore, it can be stated that the HI probe has a better S/N ratio than the LI probe even though the LI probe has greater signal gain. Although, as further discussed in chapter three, the voltage noise is very small in comparison to the current noise and resistor thermal noise components. The following comments can be made in regards to the S/N for both probes:

1) Maximize C_s for maximal S/N

2) Maximize R_b for maximal S/N

3) At low frequencies, S/N is degraded

4) Minimize C_i (Stray capacitance) for maximal S/N

5) Current noise specification, I_n, important due to high-impedance source, C_s.

As discussed earlier, a resistor value in the range of 320 to 640 Gohms will be necessary to meet bandwidth requirements. This can be accomplished with a single high-valued resistor or with feedback. Surface mount resistors in the Gohm and Tohm range are available commercially [59]. Figures 2.16 and 2.17 show the HI and LI probe configurations using feedback to obtain a high resistor value.

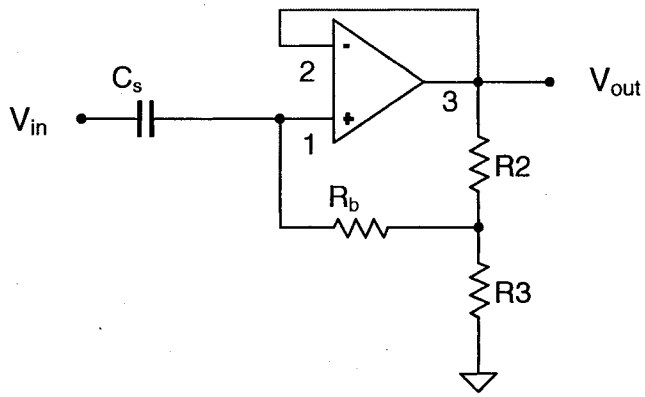

Figure 2.16 High-Impedance probe using feedback to achieve a high value for R_b.

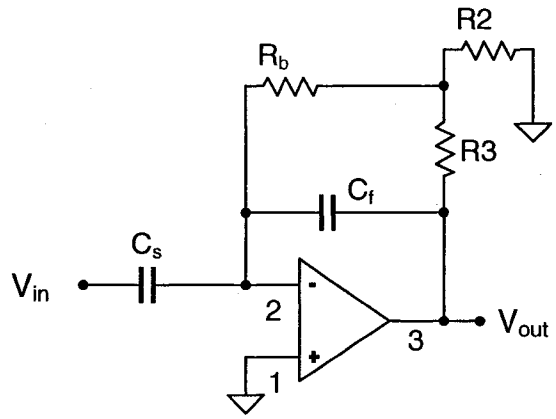

Figure 2.17 Low-Impedance probe using feedback to achieve a high value for R_b.

It can be shown that the signal-to-noise expressions are almost the same as those derived earlier with some additional noise terms due to the feedback network. In practice, this may be a better solution than a high-valued resistor due to surface contamination of the board and resistor. However, to minimize noise, this feasibility study uses a single biasing resistor without feedback.

The LI and HI probes have different sensitivities to area and spacing variation of the sensor. Assuming that the frequency of interest is higher then the 1st order pole, the transfer functions for the two probes are as follows

$$\frac{V_{out}(s)}{V_{in}(s)} = \frac{sR_bC_s}{sR_b(C_i + C_s)} = \frac{C_s}{C_i + C_s}$$ for the HI probe.

and

$$\frac{V_{out}(s)}{V_{in}(s)} = \frac{sR_bC_s}{1 + sR_bC_{ft}} = \frac{C_s}{C_{ft}}$$ for the LI probe.

Now substituting the ideal parallel-plate equation for capacitance, $\varepsilon A/d$, the transfer functions become

$$\frac{V_{out}(s)}{V_{in}(s)} = \frac{\varepsilon A/d}{\left(\varepsilon A/d + C_i\right)}$$ for the HI probe.

and

$$\frac{V_{out}(s)}{V_{in}(s)} = \frac{\varepsilon A}{dC_f}$$ for the LI probe.

Note from the two expressions that the LI probe is directly proportional to area variation and inversely proportional to spacing sensitivity. In comparison, the HI probe can be made more immune from area and spacing variation by making C_{in} very small. These effects are demonstrated in chapter four.

CHAPTER III

Experimental Materials and Methods

3.1 Noise Analysis for High-Impedance and Low-Impedance Probes

In chapter two, a description of the LI and HI probes was developed for S/N and bandwidth. The S/N_{PSD} expressions could be optimized by maximizing C_s and R_b and by minimizing I_n, E_n and stray capacitance. The necessary large biasing resistance, R_b, and low current noise, I_n, dictate the use of an op amp with an ultra-low bias current specification. As noted in chapter two, a signal current level of 0.35fA rms was obtained with a source capacitance of 0.7 pF which provides a guideline for our current noise specification. There are two op amps currently available with a current noise specification under 0.35fA rms: the OPA129 from Texas Instruments and the AD547 from National Semiconductor both of which have a current noise specification of $0.1fA/\sqrt{Hz}$ [60,61]. This research used the OPA129 since it is available in an SO-8 surface mount package. The package is also optimized for minimal stray capacitance by placing the power supply pins on the opposite side of the signal pins. A diagram of the OPA129 is shown in figure 3.1.

From the S/N_{PSD} expressions in chapter two, compare the contributions of the three noise terms to the total output voltage noise of the OPA129. We will assume $C_i=0$ (Ideal case) for both LI and HI probes and that $C_f=C_s=0.7pF$ for equal gains. Note that E_n for the OPA129, shown in figure 3.2, has the 1/f characteristic. If an R_b of 500 Gohms is used to meet the low-end frequency response of 0.5 Hz, the noise contributions from each source at 1 Hz and 2 Hz are as shown in table 3.1 ($4kT=1.61x10^{-20}$ at 17°C,room temp).

The thermal noise of the 500 Gohm resistor contributes the most noise followed closely by the op amp current noise. The op amp voltage noise, E_n, is negligible compared to the thermal and op amp current noise components. Figure 3.3 is a plot of the current noise and thermal noise terms from 0.5 to 30 Hz. If R_b is increased further, the noise is pushed further towards DC.

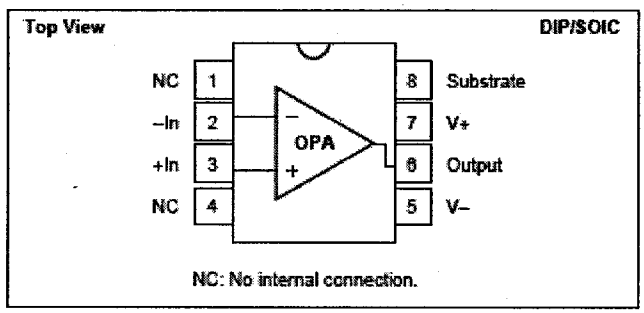

Figure 3.1 OPA129 Package [62]

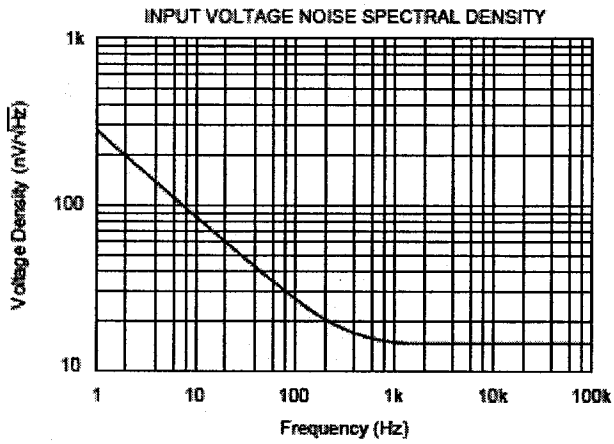

Figure 3.2 OPA129 Input Voltage Noise Spectral Density [63]

Freq.	Noise Source	Noise contribution in Vrms/√Hz
1 Hz	$\sqrt{E_n^2\left(\frac{(C_i+C_s)^2}{C_s^2}+\frac{1}{\omega^2 C_s^2 R_b^2}\right)}$ for HI	$300\text{x}10^{-9}$ for HI
	$\sqrt{En^2\left(\frac{(C_{ft}+C_i+C_s)^2}{C_s^2}+\frac{1}{\omega^2 C_s^2 R_b^2}\right)}$ for LI	$600\text{x}10^{-9}$ for LI
	$\left(\sqrt{4kT/R_b}\right)\left(1/\omega C_s\right)$	$0.41\text{x}10^{-4}$
	$I_n\left(1/\omega C_s\right)$	$0.23\text{x}10^{-4}$
2 Hz	$\sqrt{E_n^2\left(\frac{(C_i+C_s)^2}{C_s^2}+\frac{1}{\omega^2 C_s^2 R_b^2}\right)}$ for HI	$200\text{x}10^{-9}$ for HI
	$\sqrt{En^2\left(\frac{(C_{ft}+C_i+C_s)^2}{C_s^2}+\frac{1}{\omega^2 C_s^2 R_b^2}\right)}$ for LI	$400\text{x}10^{-9}$ for LI
	$\left(\sqrt{4kT/R_b}\right)\left(1/\omega C_s\right)$	$0.21\text{x}10^{-4}$
	$I_n\left(1/\omega C_s\right)$	$0.12\text{x}10^{-4}$

Table 3.1 A comparison of thermal, current, and voltage noise contributions at 1 and 2 Hz.

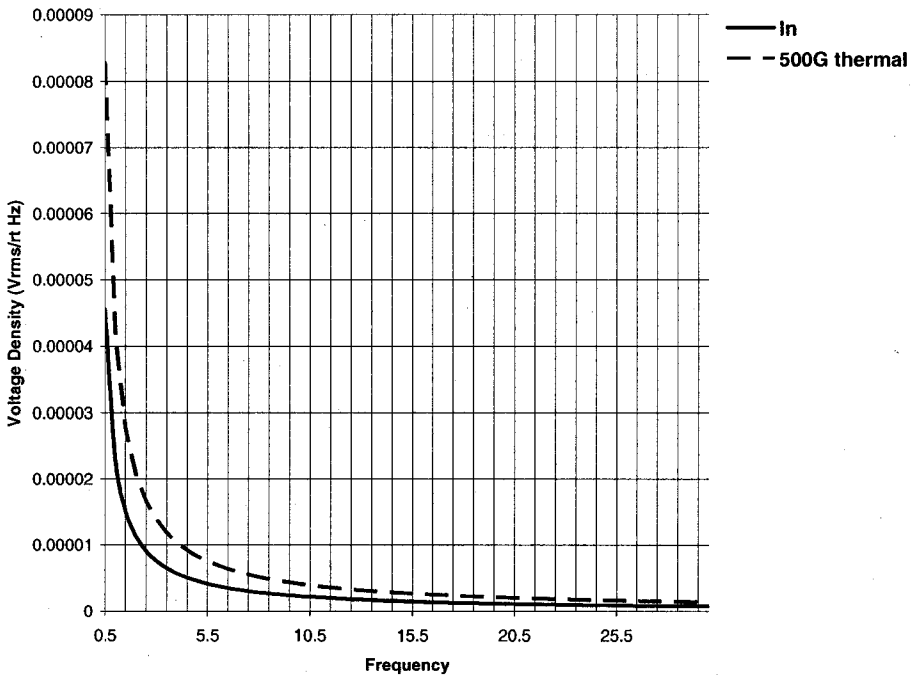

Figure 3.3 $I_n\left(1/\omega C_s\right)$ and $\left(\sqrt{4kT/R_b}\right)\left(1/\omega C_s\right)$ versus frequency for the case with a 0.7 pf source capacitance and 500 Gohm biasing resistance.

In order to obtain total RMS output noise, we can either integrate the output noise expression over frequency or we can approximate it from the above figure by dividing it into 1 Hz bandwidth sections and summing. With the summing approximation, total RMS output noise over the 0.5 to 30 bandwidth is 104 x 10^{-6}Vrms or 104uVrms. This is indeed a lot of noise which would saturate a 10uV signal in the alpha band. However, it is obvious from the above figure that most of this noise occurs at frequencies less than 2 Hz. As a comparison, if the delta range of the EEG band (0.5 to 4 Hz) is excluded the total output noise now becomes 23.6 uVrms. The inability to apply this non-contact electrode to delta band EEG measurement is one of its fundamental limitations. Further reduction in output noise level can be accomplished if the capacitive coupling of the source is increased by decreasing the

scalp-to-electrode distance. Table 3.2 provides output noise figures for various values of Cs and corresponding S/N ratios for an alpha band signal of 10uVrms. Chapter 4 will provide results for EEG readings at various distances from the scalp.

Distance from scalp	Source capacitance assuming a 3.9 cm^2 electrode	Total Output Noise level in 4 to 30 Hz band	Signal to Noise Ratio with 10uVrms signal
5.0 mm	0.69 pF	23.6 uVrms	-7.82dB
4.5 mm	0.77 pF	21.5 uVrms	-6.65 dB
4.0 mm	0.87 pF	19.0 uVrms	-5.58 dB
3.5 mm	0.99 pF	16.5 uVrms	-4.35 dB
3.0 mm	1.15 pF	14.4 uVrms	-3.17 dB
2.5 mm	1.38 pF	12.0 uVrms	-1.58 dB

Table 3.2 Theoretical Output Noise Levels and S/N Ratios for Varying Cs

3.2 High-Impedance and Low-Impedance Probe Design

Figure 3.5 shows the circuit board structures for the two probes. Both probes are 3 layered devices with a surface mount circuit layer on top, a guard layer in the middle and the pick-up plate on the bottom. In both cases, C1 and C2 are supply decoupling capacitors of 0.1uF each. C_f for the LI probe, which is mounted on top of R1, is a 1.0 pF NP0 dielectric capacitor with a tolerance of +/- 0.25 pF. R1 is a size 1206, +/-20%, 500G resistor made by Ohmcraft, Inc., part number SM1206M5009LB [64]. The serpentine layout of the resistor, shown in figure 3.4, helps minimize stray capacitance. Four insulating standoffs of less than 4.0 mm^2 are mounted underneath the probe sensing plate.

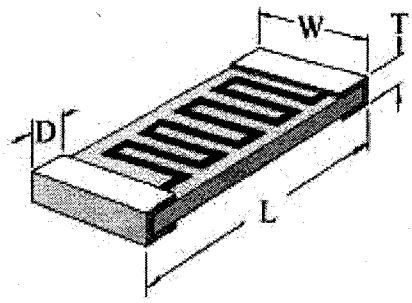

Figure 3.4 Size 1206, $500x10^9$ ohm resistor manufactured by Ohmcraft.
(L=126 mils, W=63 mils, T=30 mils)

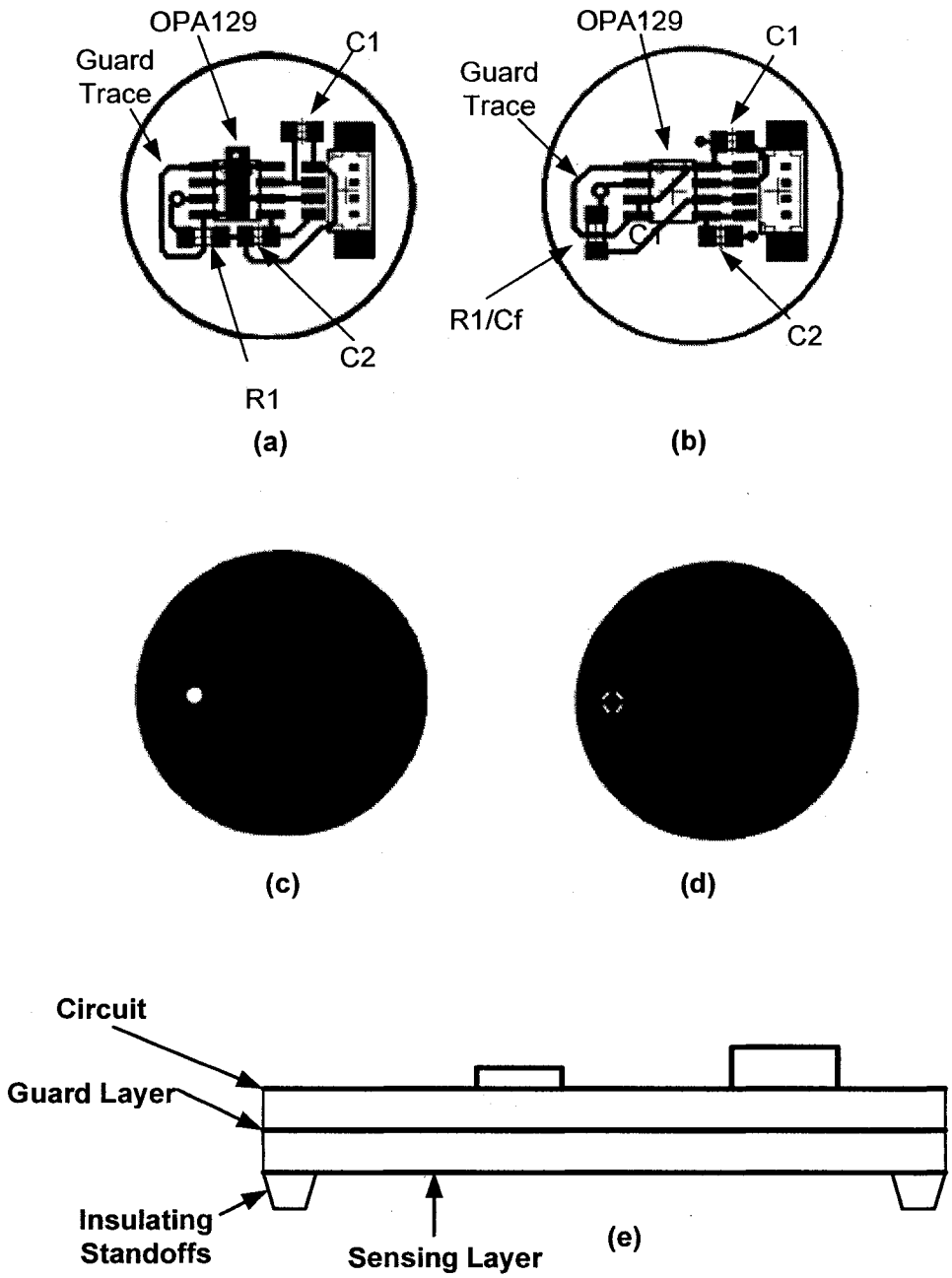

Figure 3.5 HI and LI Probe Circuit Board Layout (Enlarged for clarity).(a) HI Signal Layer (b) LI Signal Layer (c) Inner guard layer (d) Bottom sensing layer (e) 3 layered probe structure

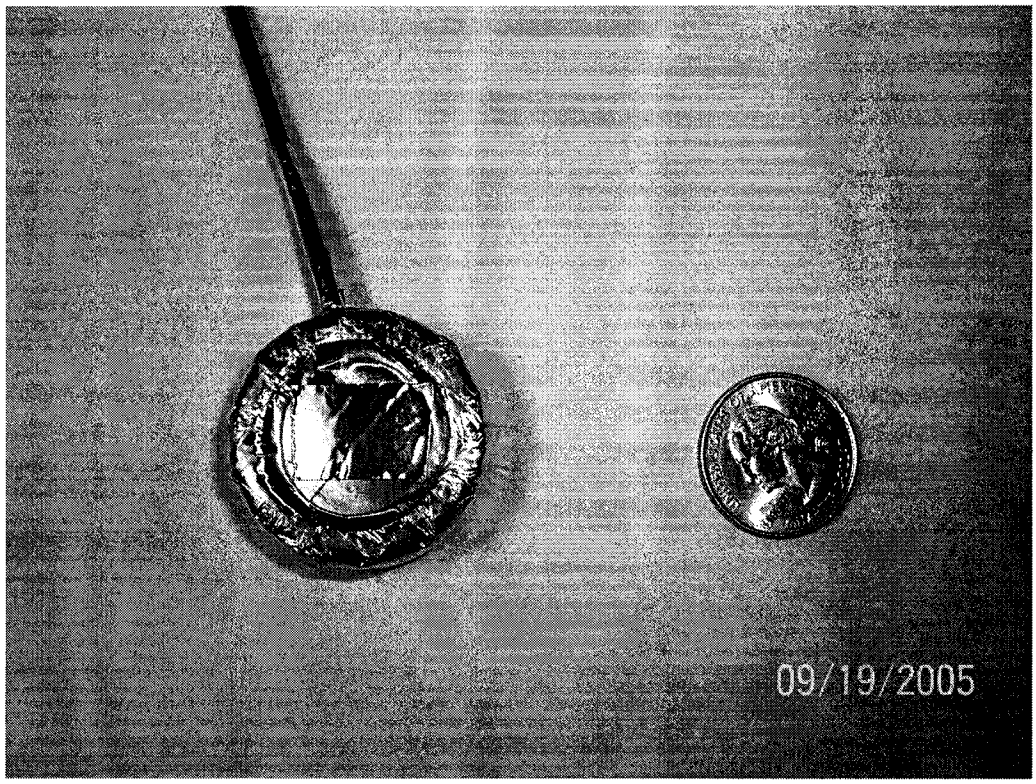

Figure 3.6 Top view photo of probe

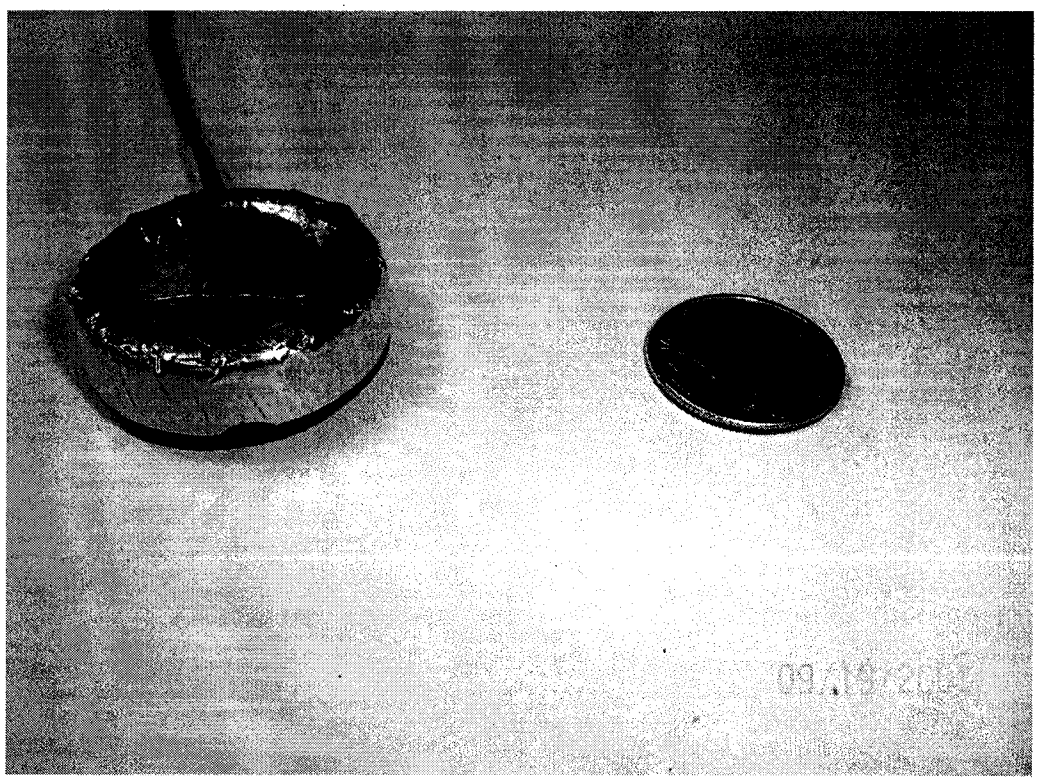

Figure 3.7 Side view photo of probe

3.3 Measurement of the Alpha Rhythm

This research focuses on the non-contact electroquasistatic measurement of the alpha rhythm for two reasons: firstly, the alpha rhythm is well documented and is common throughout the population. In fact, approximately 95% of humans produce a clearly identifiable alpha rhythm [65]. Secondly, the alpha rhythm recorded from the occipital areas is easily elicited and controlled with eye opening and closure. In this study, the alpha rhythm is recorded from the O1 and/or O2 sites of the 10-20 electrode placement system (Figure 3.8) with a reference electrode on the A1 site [66]. Measurements are made at 2.5mm, 3.0mm, 3.5mm and 4.0mm from the scalp using insulating standoffs of appropriate length. The standoffs make contact with the scalp and probes are held in place using a cotton headband using the smallest pressure to maintain probe stability. Signals from the non-contact probes are further processed with a post-gain of 25,000 and post-filtering of 4 to 30 Hz. This filter is suitable for theta and alpha band detection while also minimizing system noise to suitable levels. The high pass filter is an 8^{th} order Bessel type while the low pass is an 8^{th} order Butterworth. In order to minimize overshoot and ringing which may occur with probe movement, the Bessel filter has a more suitable transient response. The Butterworth has a sharper cutoff frequency response to minimize 60 Hz interference. Post-filter frequency and transient responses are shown in figure 3.9. All signals are sampled at 250 Hz and acquired with a National Instruments DAQ board run by Labview (See system diagram in figure 3.10). Due to the low signal-to-noise ratio of the measurement, the inherent processing gain of the FFT is utilized to obtain improved estimates of power in the EEG alpha band [68]. In the calculation of the FFT, 3 seconds of data are used with a 1 second Hamming window. Using 3 seconds of data is simply a compromise between having enough data to improve detection and not being excessively long to make the technique unusable in near real time.

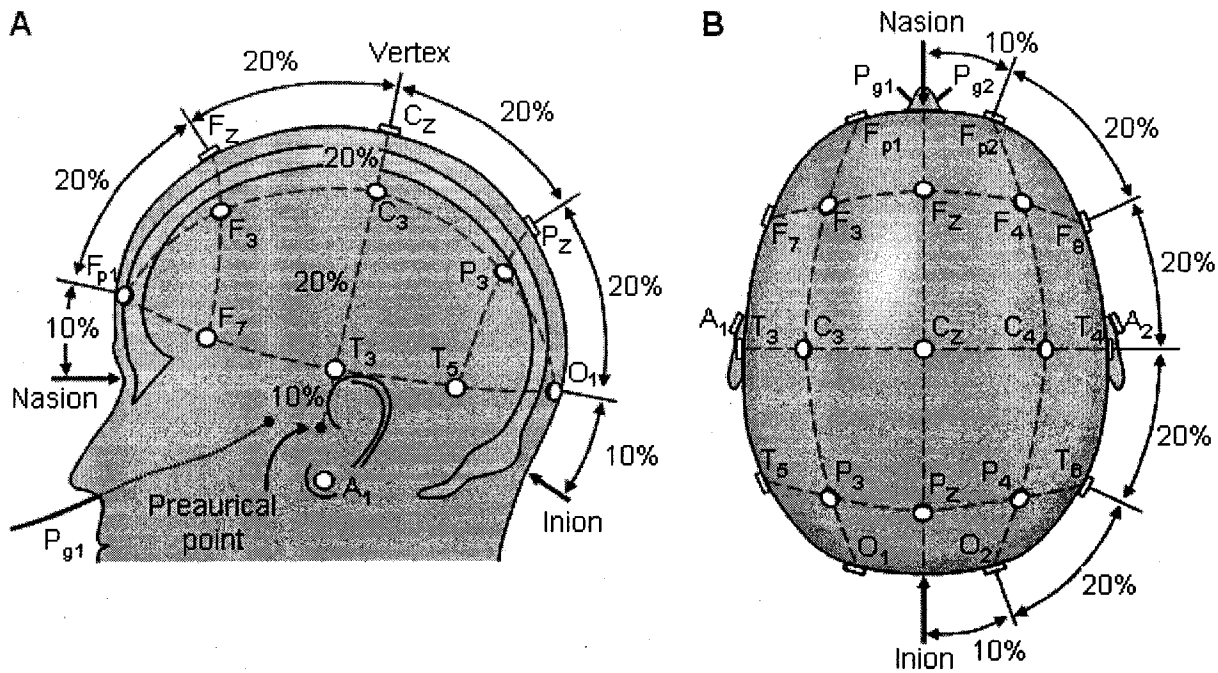

Figure 3.8 The 10-20 EEG Electrode Placement system of the International Federation [67].

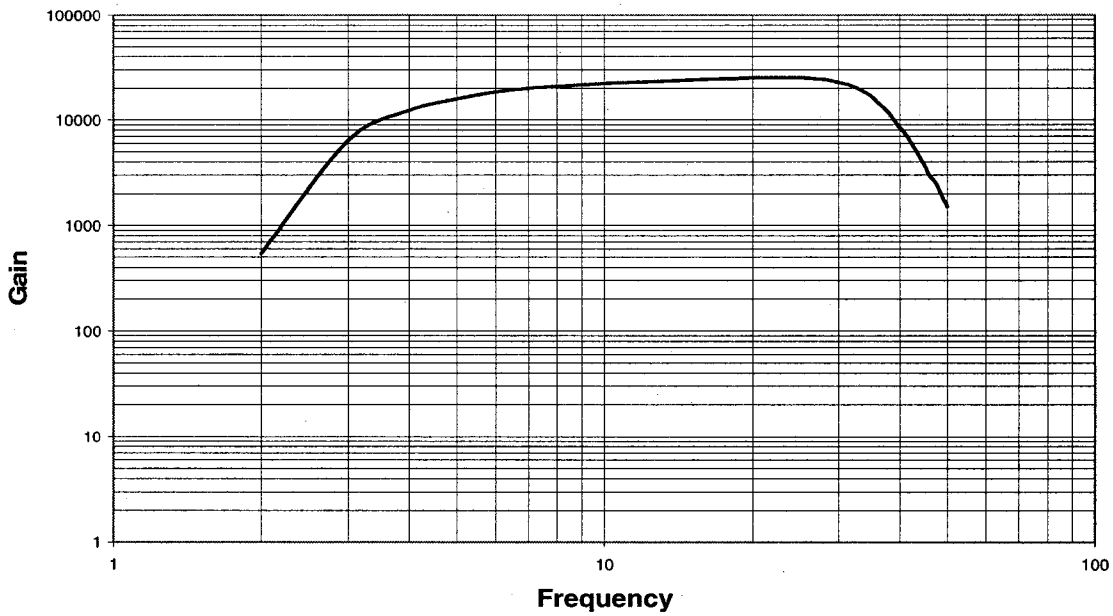

(a)

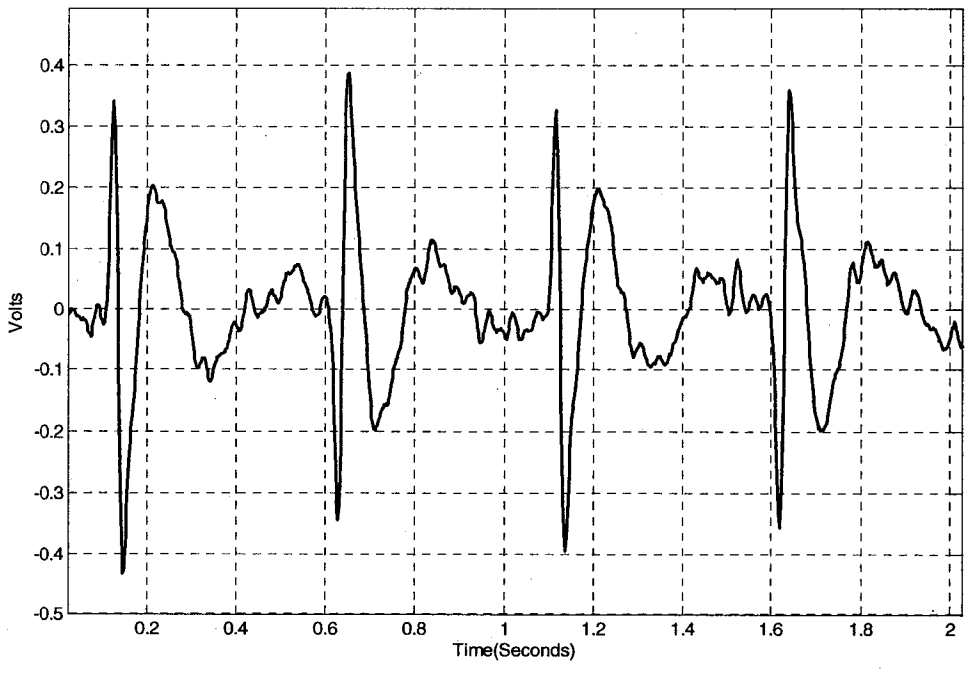

(b)

Figure 3.9 Post filtering **(a)** frequency response and **(b)** transient response using a 1 Hz square wave. Same response for both measurement channels.

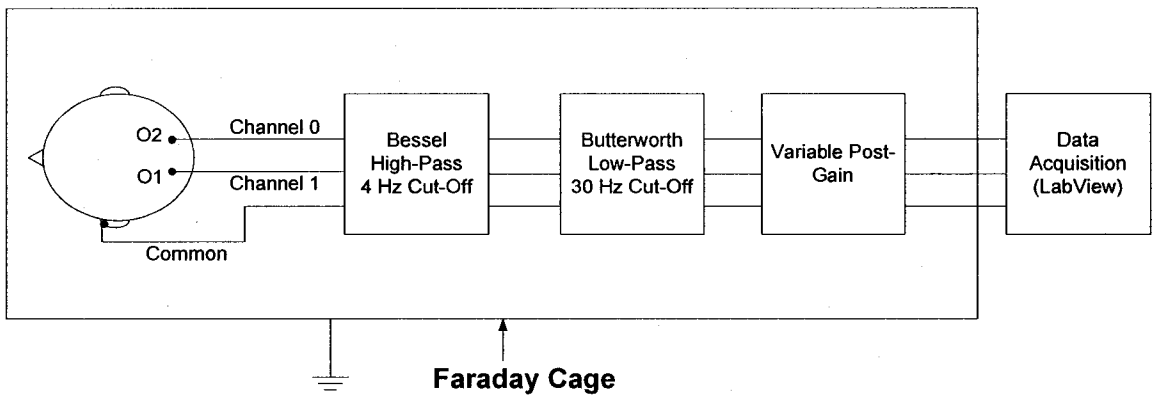

Figure 3.10 Block diagram of instrumentation system

CHAPTER IV

EXPERIMENTAL RESULTS

4.1 Electrical Characterization of HI and LI Probes at 3.5 mm Spacing

Initial tests of the high-impedance (HI) and low-impedance (LI) probes were made for the following parameters at a distance of 3.5mm from a circular conductive input plate of 4.0 cm^2: output noise, low frequency cut-off, and gain. These parameters, along with the resulting signal-to-noise ratio for a 10uVrms input signal, are documented in table 3.1. The DC output was also measured for all probes to investigate electrode saturation. The specified bias current for the OPA129UB is a maximum of 100fA meaning that the maximum offset should be 500 Gohm*100fA= 50 mV plus or minus the DC offset of the amplifier which is specified at 2mV DC[68]. The electrode DC output simply provides an indicator of how well the amplifier is behaving. A large deviation from 50 mV could indicate unwanted leakage currents in the electrode circuitry or it may indicate a significant change in bias current due to temperature. In all cases, probe DC output remained within 30 mV after 20 minute application of power.

	HI Probe	LI Probe
Output Noise	16.5 uVrms	32 uVrms
Cut-off Freq	0.09 Hz	0.19 Hz
Gain at 10 Hz	0.91	1.45
Signal-to-Noise	-5.17 dB	-6.9 dB

Table 4.1 High-Impedance (HI) and Low-Impedance (LI) Probe Parameters at 3.5mm spacing.

Note from the above test parameters that an extremely low input capacitance is obtained for the HI probe since the source capacitance is 1 picofarad at a 3.5mm distance using the probe plate area. Therefore, since

$$Cs/(Cs+Ci) = 0.91,\ C_i = 98 \text{ femptofarads}$$

This is a very good result considering that no elaborate bootstrapping techniques are being utilized to reduce C_{Rb} and C_{icmp} [69].

Probe sensitivity was also measured using a test signal of 8 Hz, the low end of the EEG alpha band, at amplitude of 10uVrms. Figure 4.1 shows the PSD estimates for the HI and LI probes at 3.5 mm spacing.

4.2 Motion Stability Tests for HI and LI probes

Area and spacing variation sensitivity for both probes was described in chapter 2. As one may expect, both probes are susceptible to motion artifact but the LI probe is more prone to this as described in chapter 2. Recall that the LI probe is directly proportional to area variation and inversely proportional to spacing variation. Tests were implemented to investigate both probes response to motion artifact. Using a reference electrode on the left wrist, one can measure the ECG on the scalp. This is beneficial in this case since the gain of the two channels can be equalized and the response compared. Both probes were placed in close proximity on the head for cases with and without hair. Tests were taken on the forehead

at approximately the Fp1 and Fp2 sites (see figure 3.8) for the no-hair case and at O1 and O2 for the with-hair case. For both cases, two movements were investigated: forward/backward head movement and left/right head movement. The results are shown in figures 4.2 and 4.3 for a 3.5mm probe-scalp distance (The LI probe detected ECG is inverted as it should be) Note that hair makes the probes more susceptible to motion artifact but is more pronounced with the LI probe.

4.3 Alpha Rhythm Detection

Although the probes at 3.5mm can reliably detect a 10uVrms sinusoidal signal, EEG rhythms are hardly this clean and stationary. They constantly vary in amplitude and are further buried in other "brain noise" and other signals not of brain origin. Figure 4.6 shows several sample EEG time traces recorded with a standard wet electrode at scalp site O1 for eyes open and eyes closed. Evident in the eyes closed cases is the dominant alpha rhythm showing its "bursty" characteristic. In an effort to investigate probe reliability for alpha rhythm detection, the ability to classify based on a discriminating feature of total 9-12 Hz power was compared to a standard Ag-AgCl wet electrode. This was studied based on the response of a test data set to features extracted from a training data set. In all experiments, the test set was acquired 24 hours after the training set. For all training and test data sets, 20 ten-second samples of eyes-closed and 20 ten-second samples of eyes-open data were acquired. The eyes-open and eyes-closed samples were alternated during the testing session with one trial representing one sample of eyes-closed and one sample of eyes-open data. Each test session lasted approximately 25 minutes and was performed on and by the author who did not take part in any EEG biofeedback training. Figures 4.4a and 4.4b show training

and test data scatter plots acquired using a wet electrode. Figure 4.5 shows PSD estimates from the 20 trial training set and figure 4.6 shows 3 sample time traces of eyes open and eyes closed data. Figures 4.5 and 4.6 are included for the reader to compare to results obtained using the non-contact probes. The distinct spectral peak around 10 Hz for O1 recordings with eyes closed and the waxing and waning rhythmic nature evident in the eyes closed time traces are two typical characteristics of the alpha rhythm.

For all training data sets the discriminating threshold value was determined as halfway between the means. For example, in figure 4.4a, the discriminating threshold value is determined to be -18.25 dB. After using this threshold as a discriminating feature for the test data set shown in figure 4.4b, a classification accuracy of 100% for total alpha power is obtained. As expected, a high accuracy is obtained with stable recordings from a wet contact electrode. It is these results with which the classification accuracy of the non-contact probes will be compared.

Figures 4.7-4.9 summarize the data obtained using the LI probe at a probe-scalp distance of 3.5mm. The results using a -8.5 dB discriminating threshold, shown in figure 4.7, indicate an 82.5% classification rate. Obtaining these results required the subject to remain absolutely still which made the testing very difficult. Further testing of the LI probe at other distances was abandoned for movement-related issues.

Figures 4.10-4.21 summarize the data obtained using the non-contact HI probes at distances of 4.0mm, 3.5mm, 3.0mm, and 2.5mm. A distance smaller than 2.5mm was considered impractical, compromising its usefulness as a non-contact probe (i.e., room for hair). Note the low SNR and the prevalence of high theta band power in the non-contact electrode cases. Discriminating threshold values for the 4.0 mm, 3.5mm, 3.0mm, and 2.5

mm cases are -14.7 dB, -15.1 dB, -14.8 dB, and -16 dB, respectively. Classification accuracy for the four HI probe cases and the one LI probe case is tabulated in table 4.2. Table 4.2b is an attempt to obtain a more accurate PSD estimate by using overlapping time windows in the three second sample.

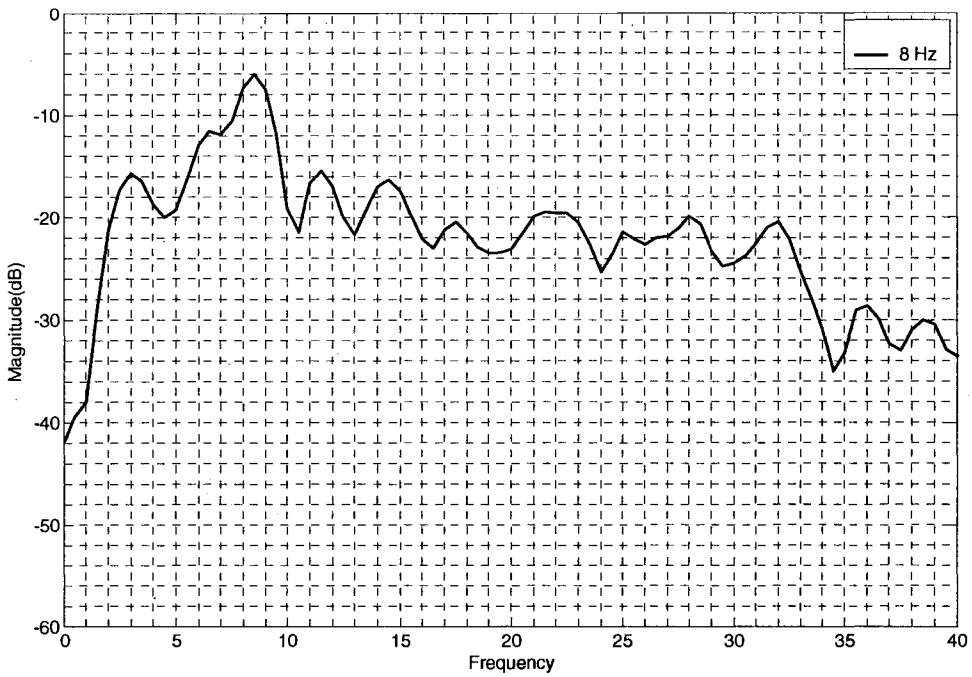

(a)

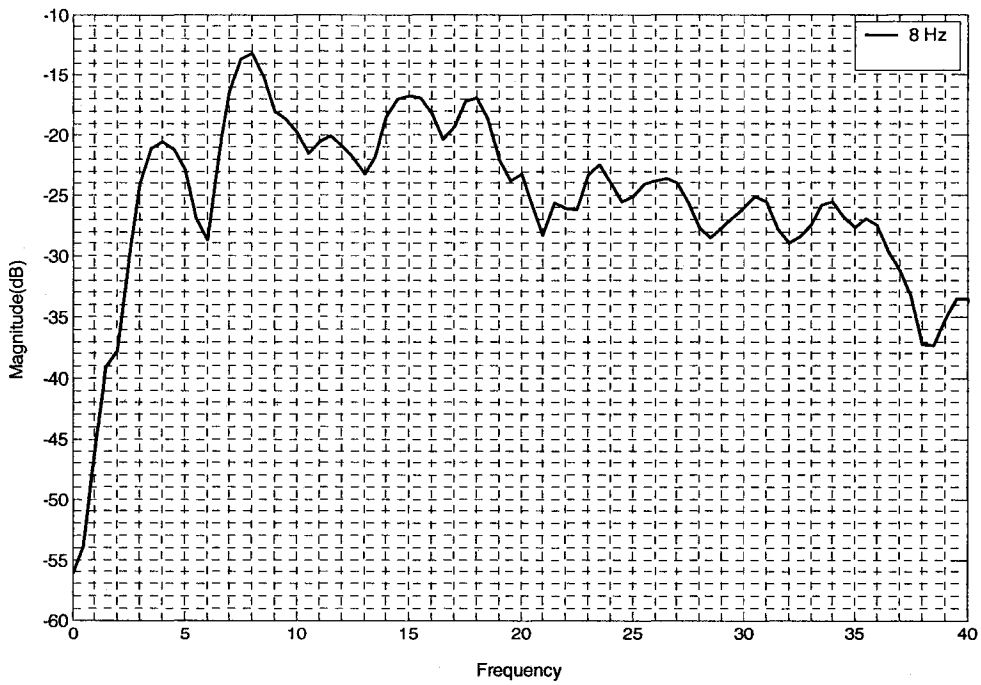

(b)

Figure 4.1 Power Spectral Estimates for an 8 Hz reference signal at amplitude of 10 uVrms using (a) LI Probe and (b) HI probe at a distance of 3.5 mm.

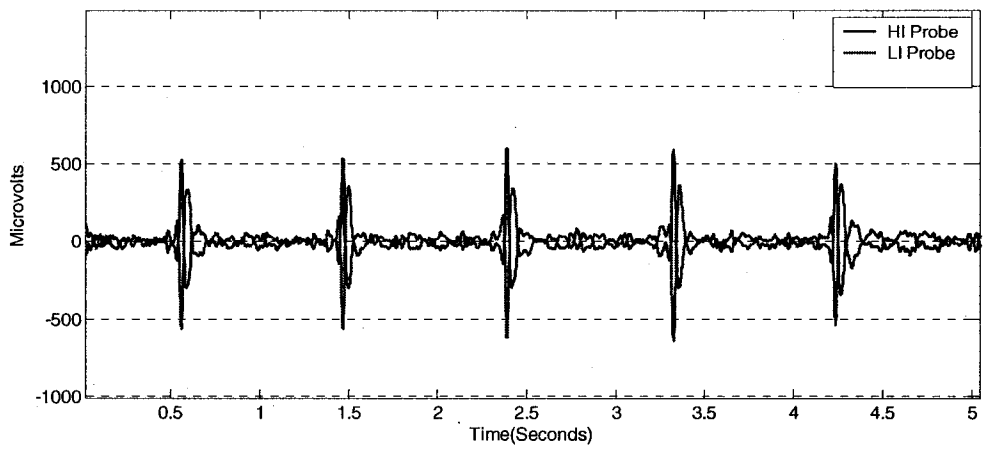

(a)

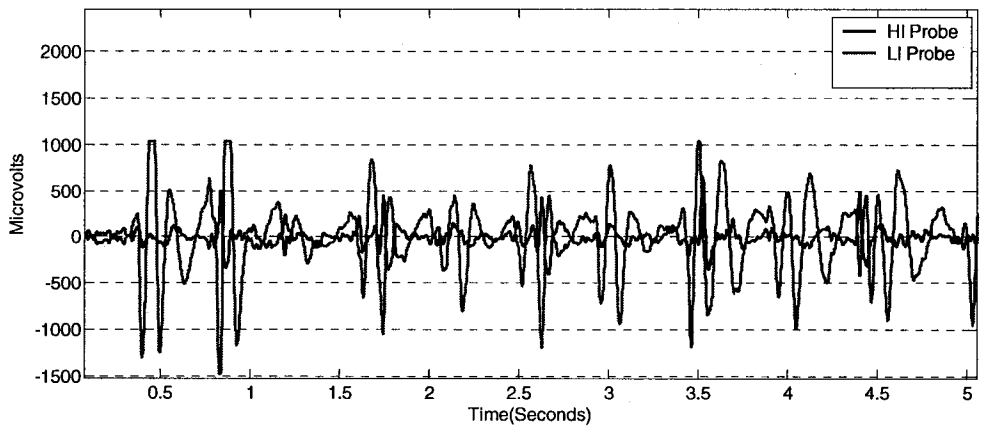

(b)

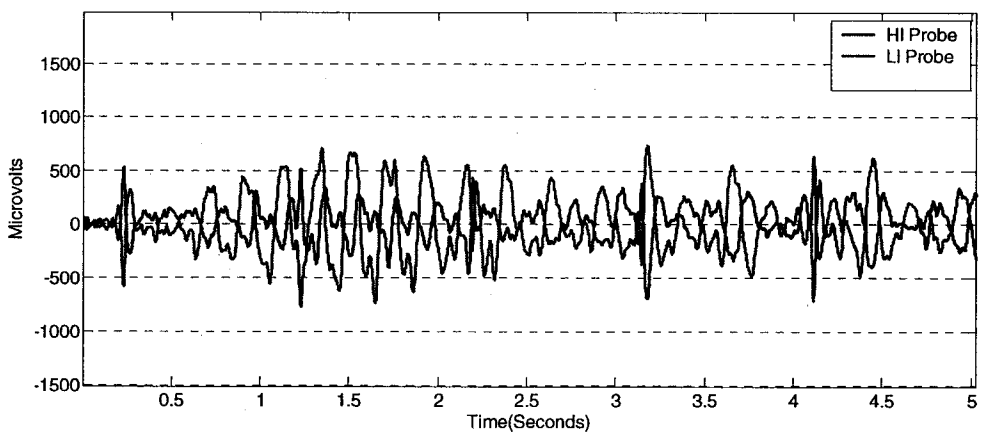

(c)

Figure 4.2 Comparison of HI and LI probes to head motion with LI probe at Fp1 and HI probe at Fp2 (a) Resting ECG (b) forward and backward head movement (c) left and right head movement

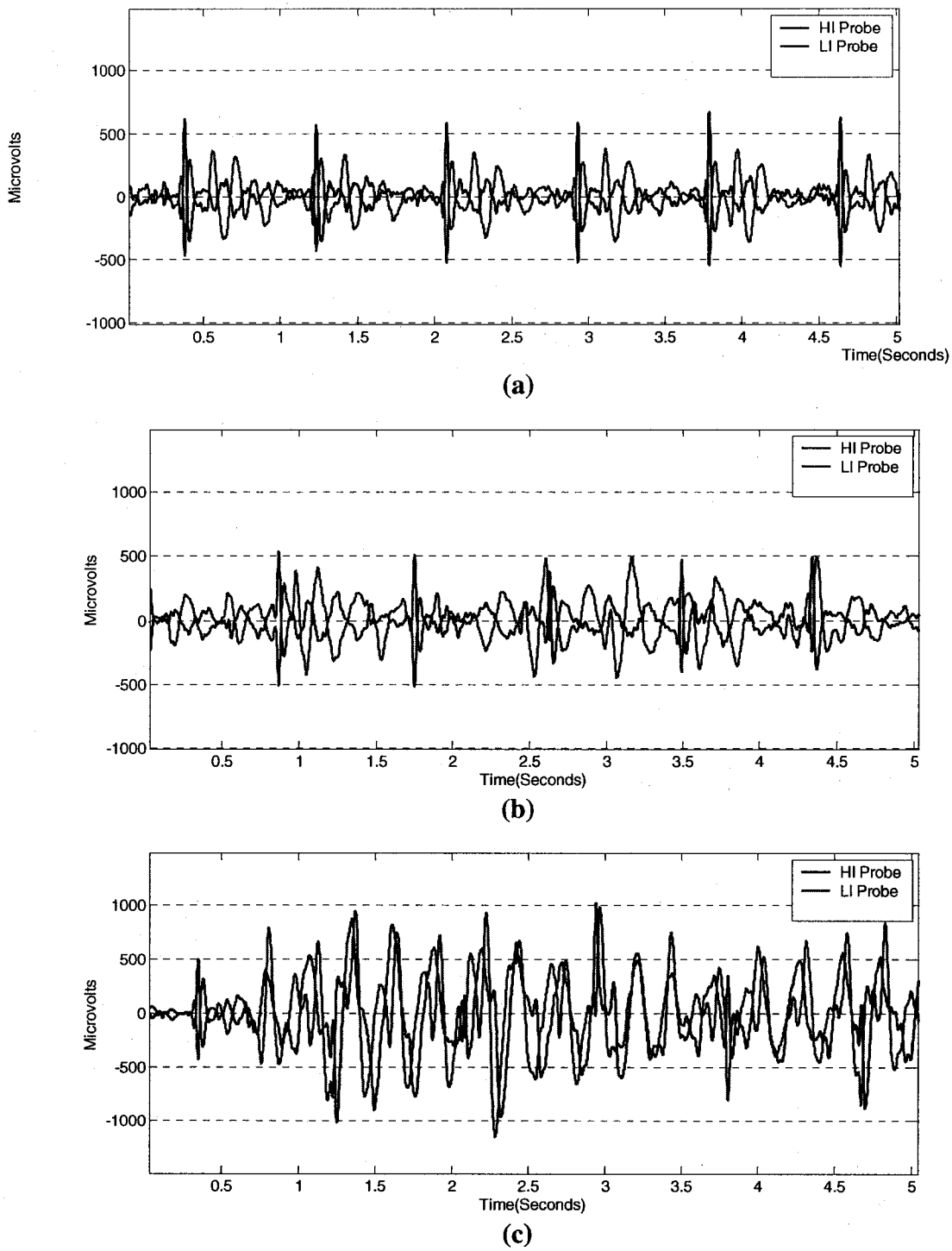

Figure 4.3 Comparison of HI and LI probes to head motion with LI probe at O1 and HI probe at O2 (a) Resting ECG (b) forward and backward head movement (c) left and right head movement

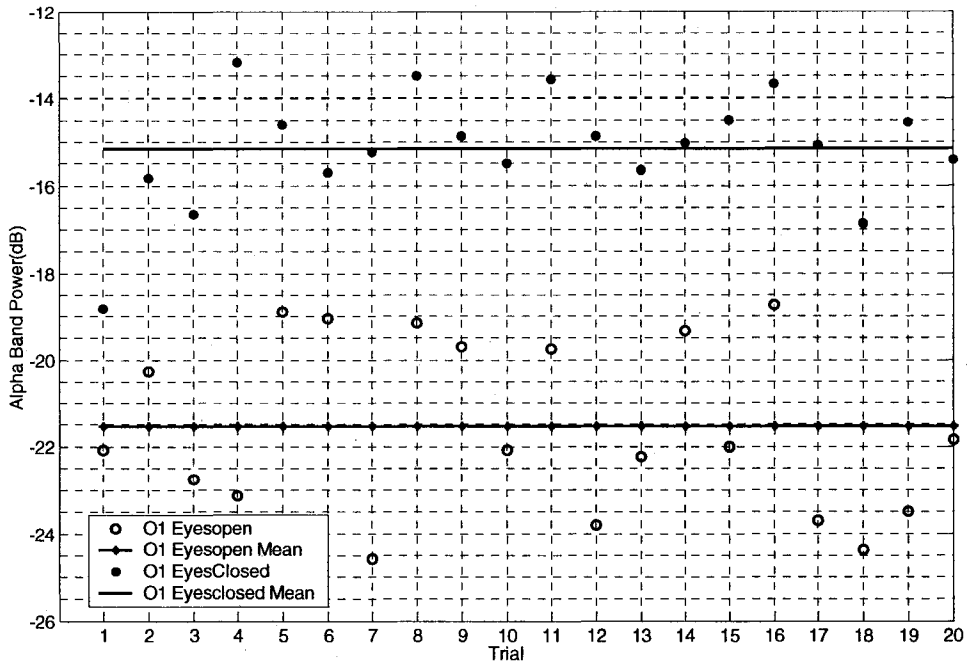

(a)

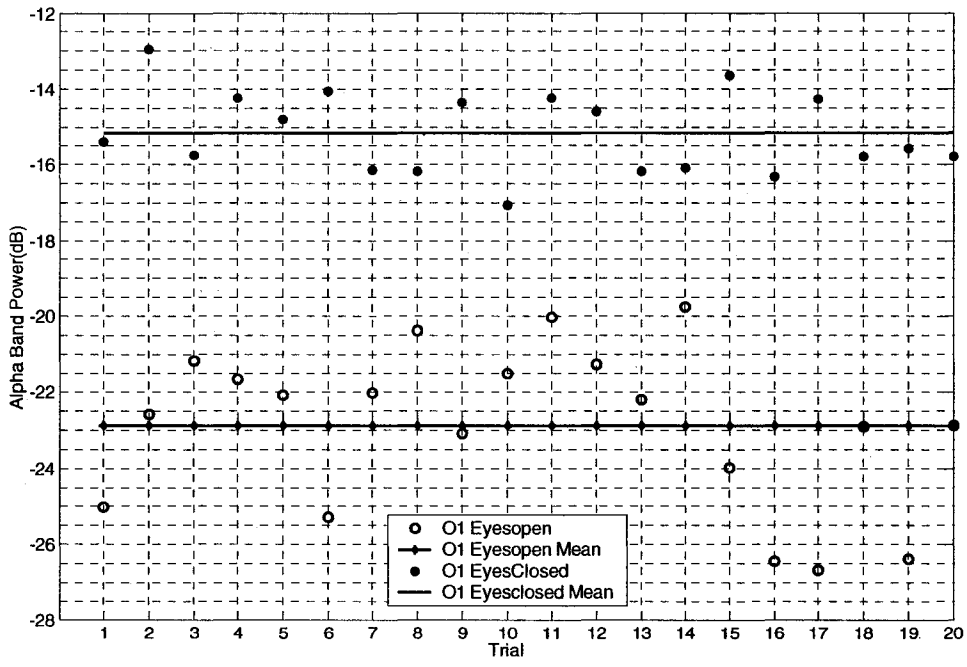

(b)

Figure 4.4 Total Alpha Band Power vs. Trial recorded at O1 with wet electrode. **(a)** Training Set **(b)** Test Set

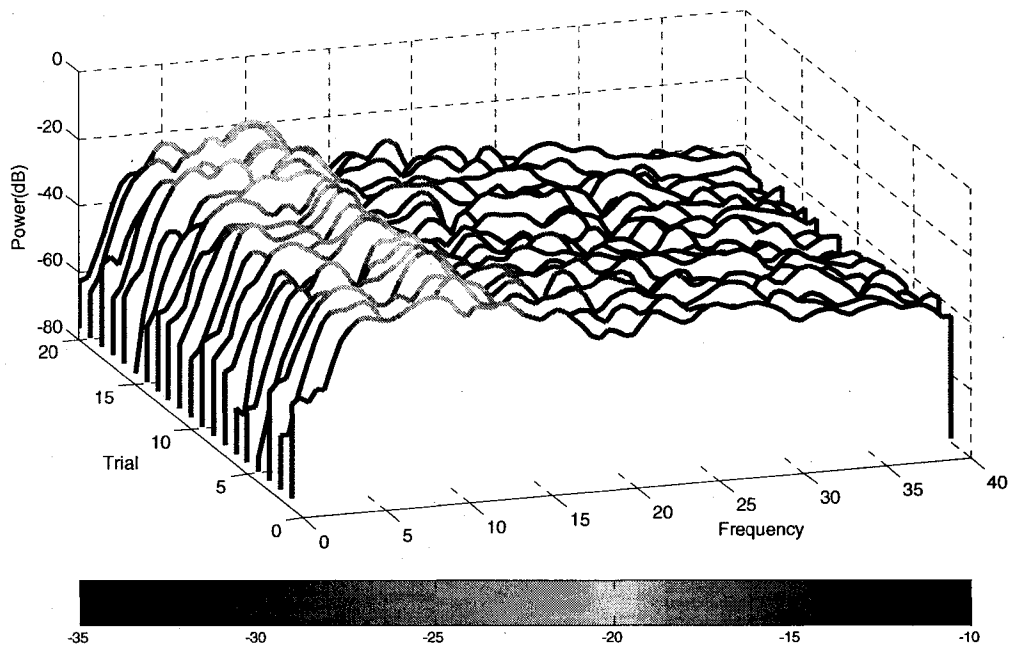

(a)

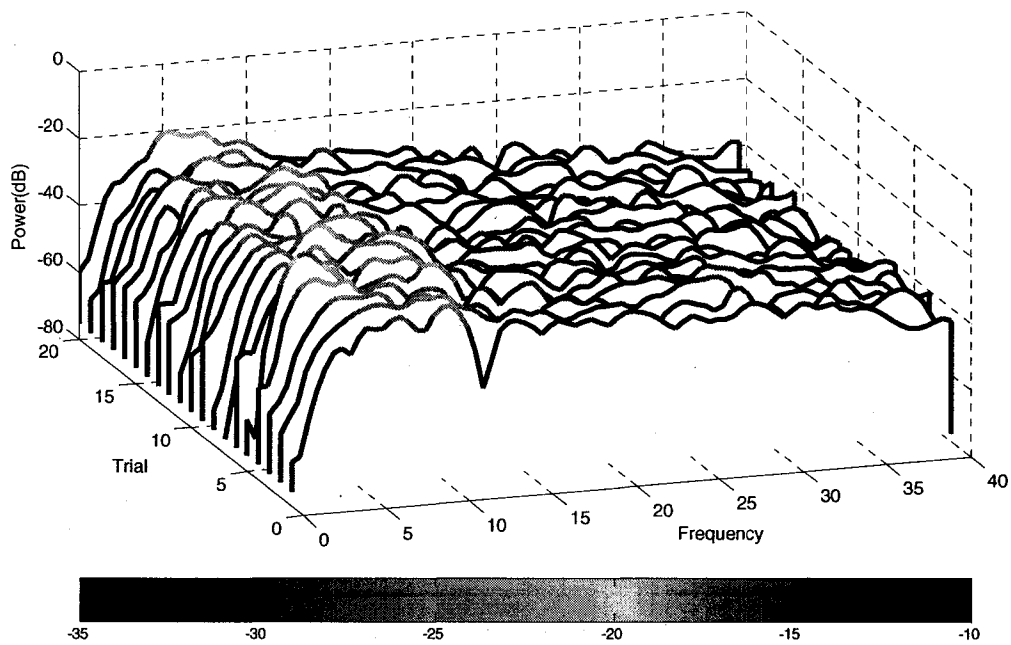

(b)

Figure 4.5 PSD estimates vs. Trial recorded at O1 with Wet Electrode.
(a) Eyes Closed **(b)** Eyes Open

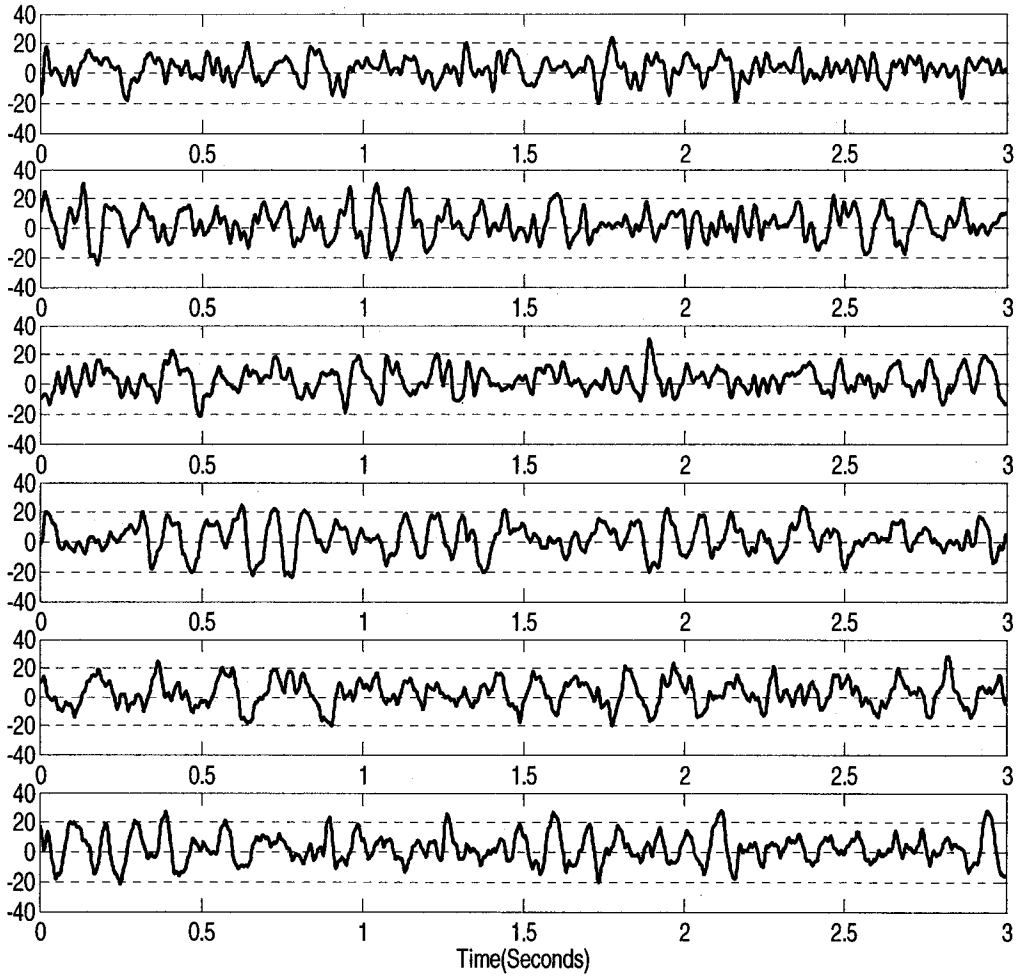

Figure 4.6 Sample time traces for 3 trials of eyes open and eyes closed data recorded at O1 with wet electrode. From the top: eyes open trial 1, eyes closed trial 1, eyes open trial 10, eyes closed trial 10, eyes open trial 20, eyes closed trial 20.

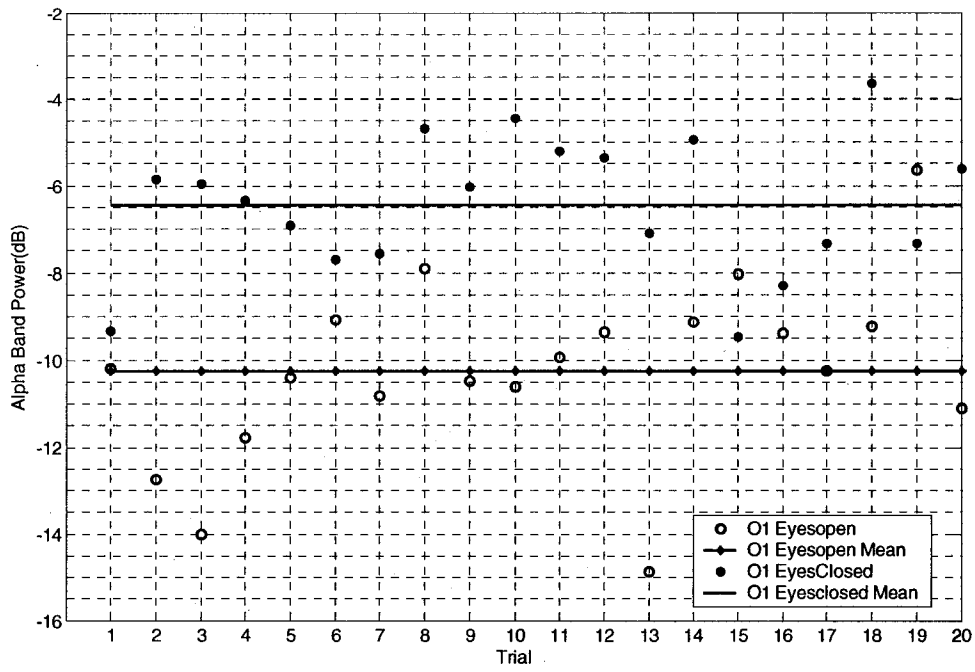

(a)

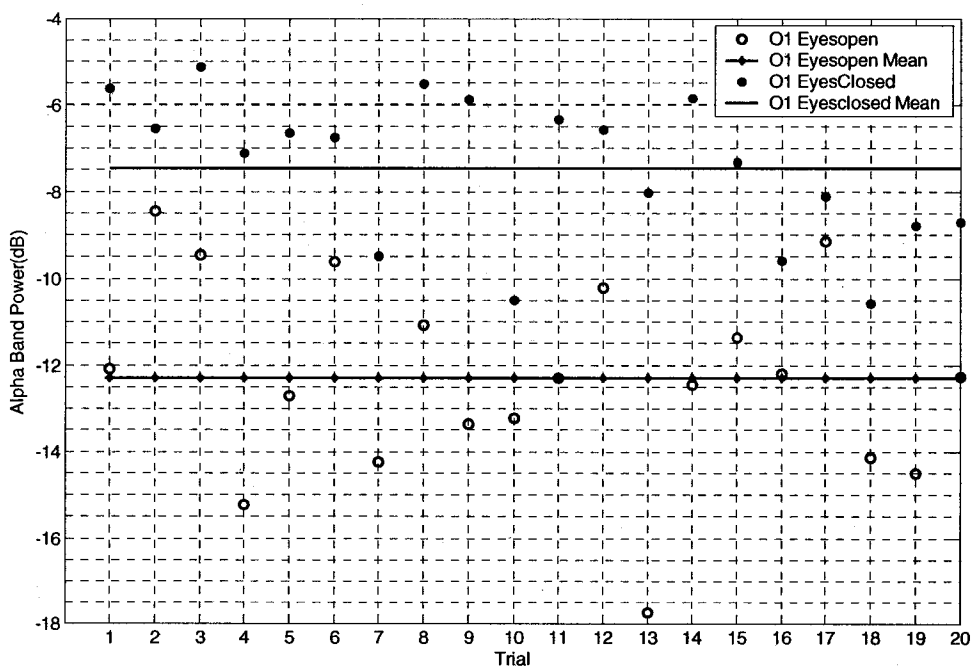

(b)

Figure 4.7 Total Alpha Band Power vs. Trial recorded at O1, 3.5 mm from scalp with LI probe **(a)** Training Set **(b)** Test Set

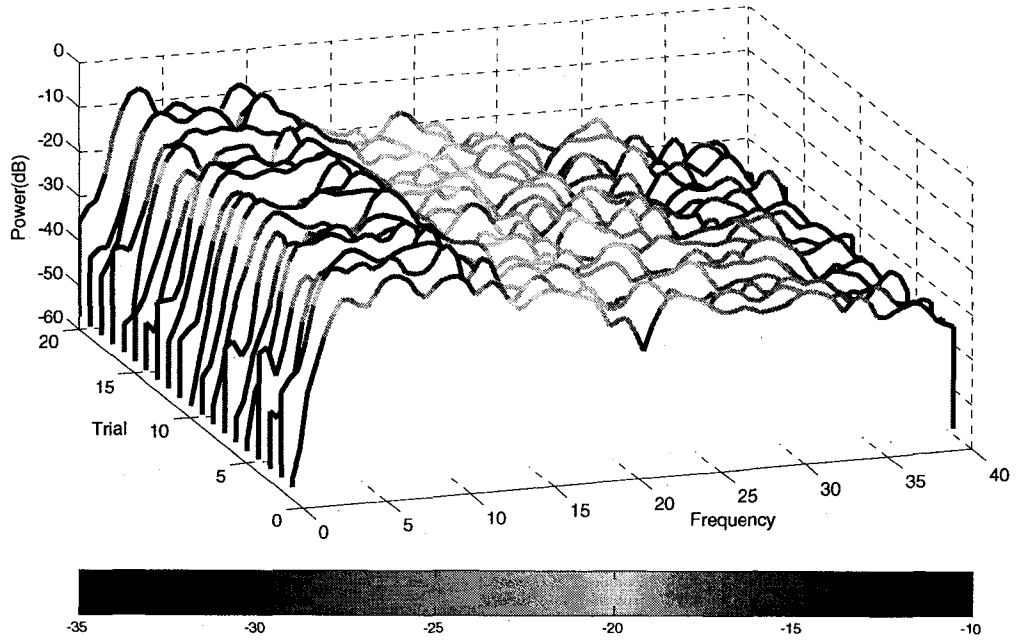

(a)

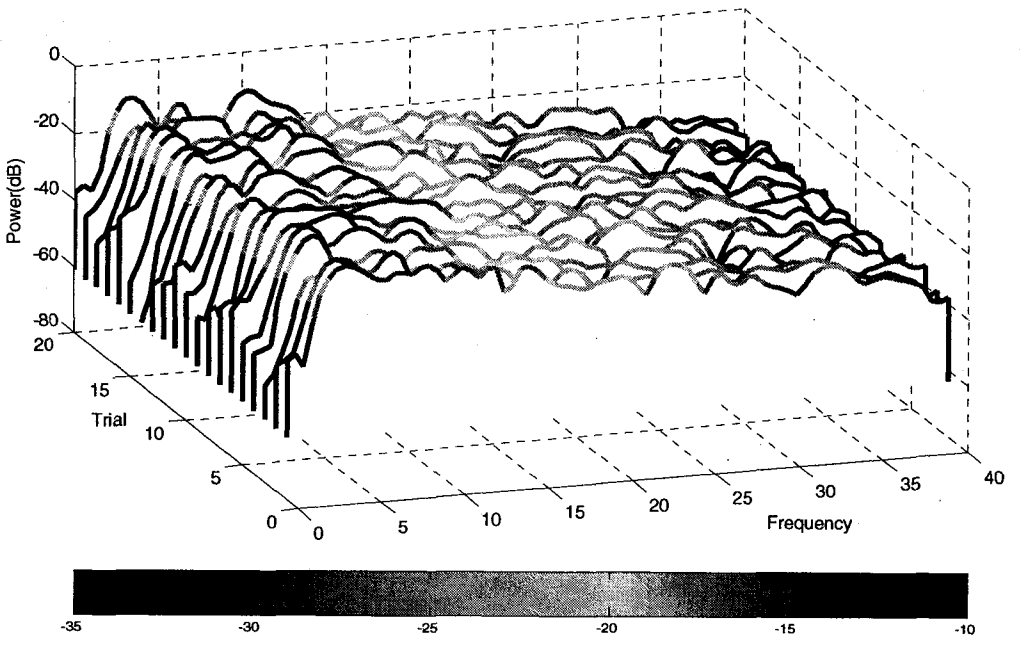

(b)

Figure 4.8 PSD Estimates vs. Trial recorded at O1, 3.5 mm from scalp with LI probe **(a)** Eyes Closed **(b)** Eyes Open

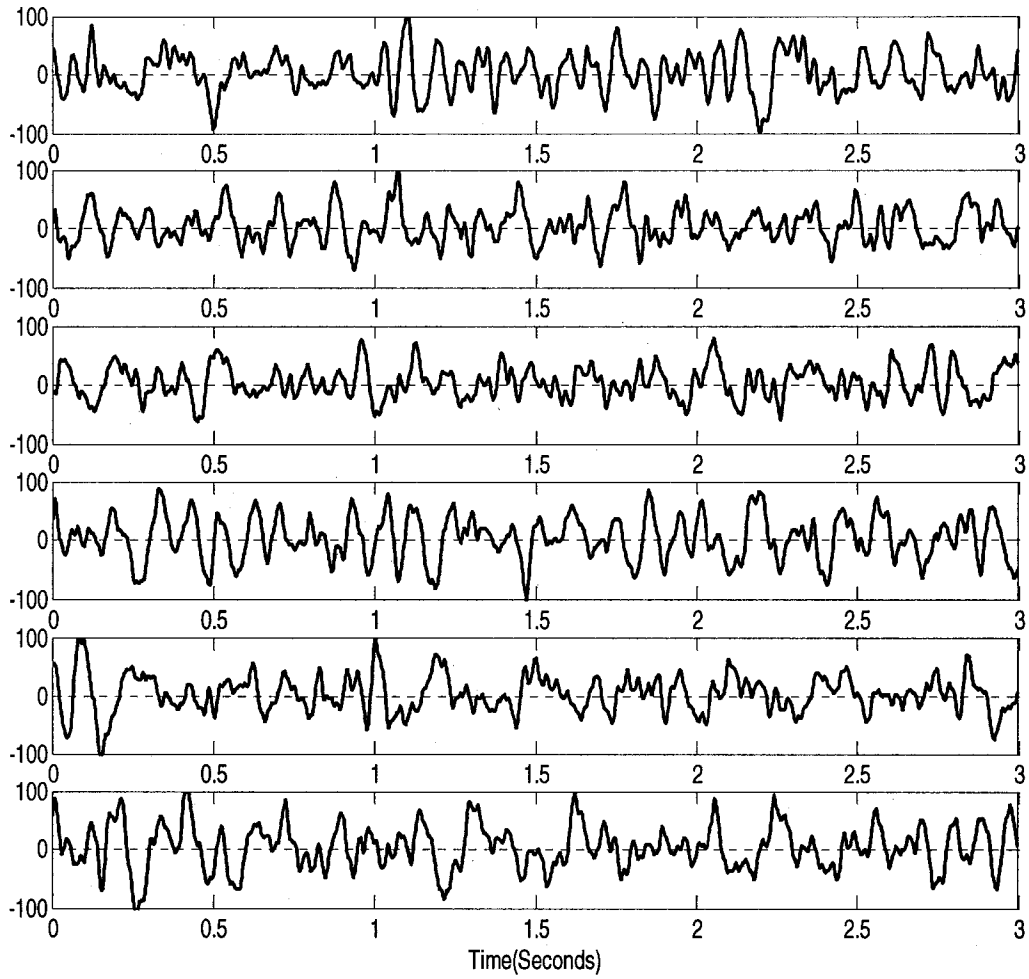

Figure 4.9 Sample time traces for 3 trials of eyes open and eyes closed data recorded at O1, 3.5 mm from scalp with LI probe. From the top: eyes open trial 1, eyes closed trial 1, eyes open trial 10, eyes closed trial 10, eyes open trial 20, eyes closed trial 20.

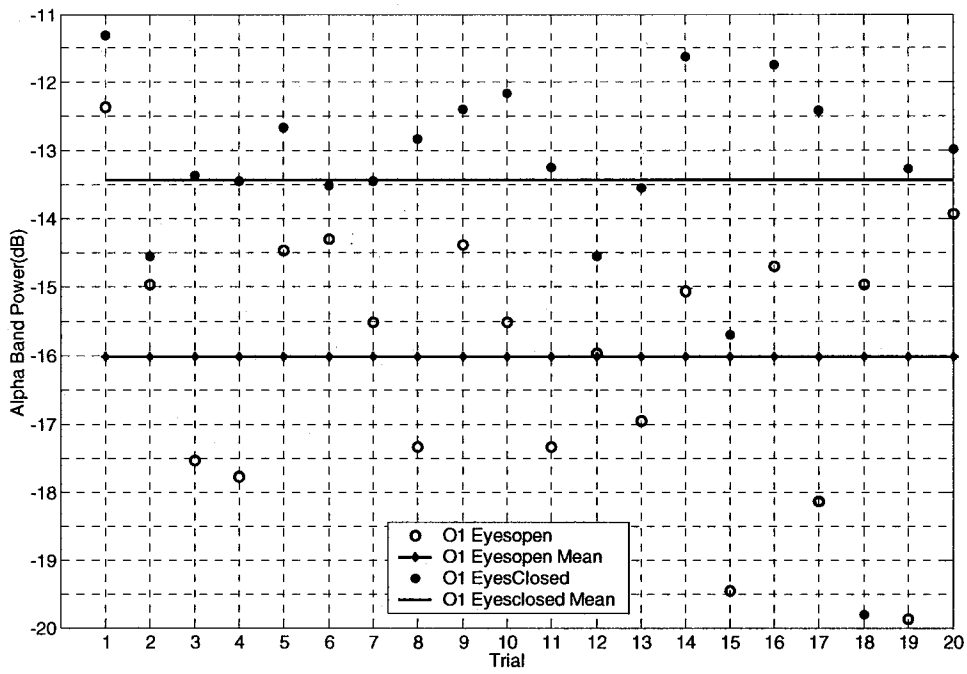

(a)

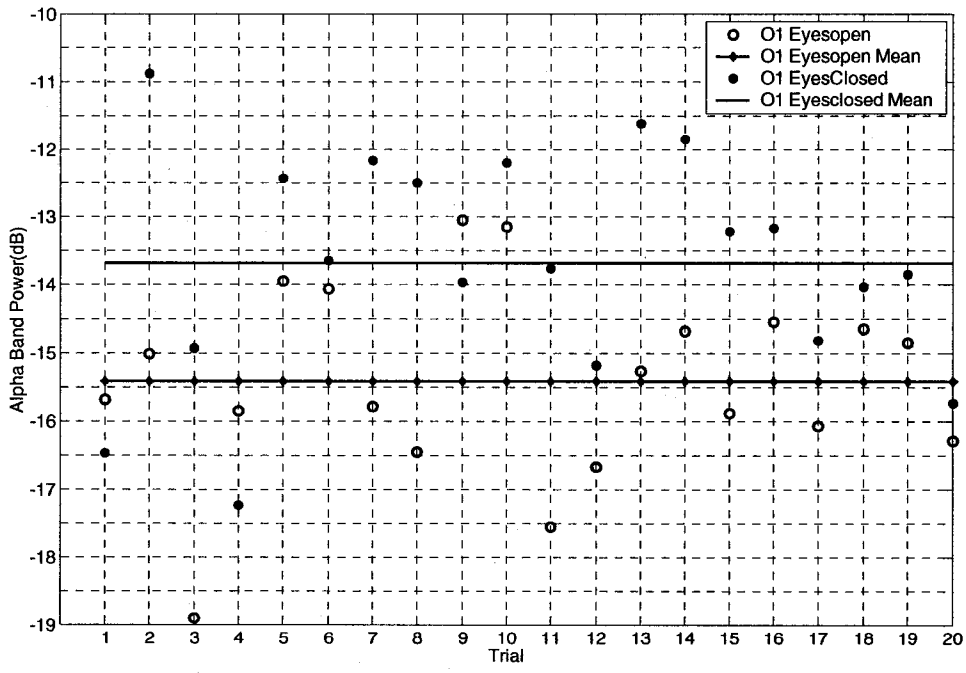

(b)

Figure 4.10 Total Alpha Band Power vs. Trial recorded at O1, 4.0 mm from scalp
(a) Training Set **(b)** Test Set

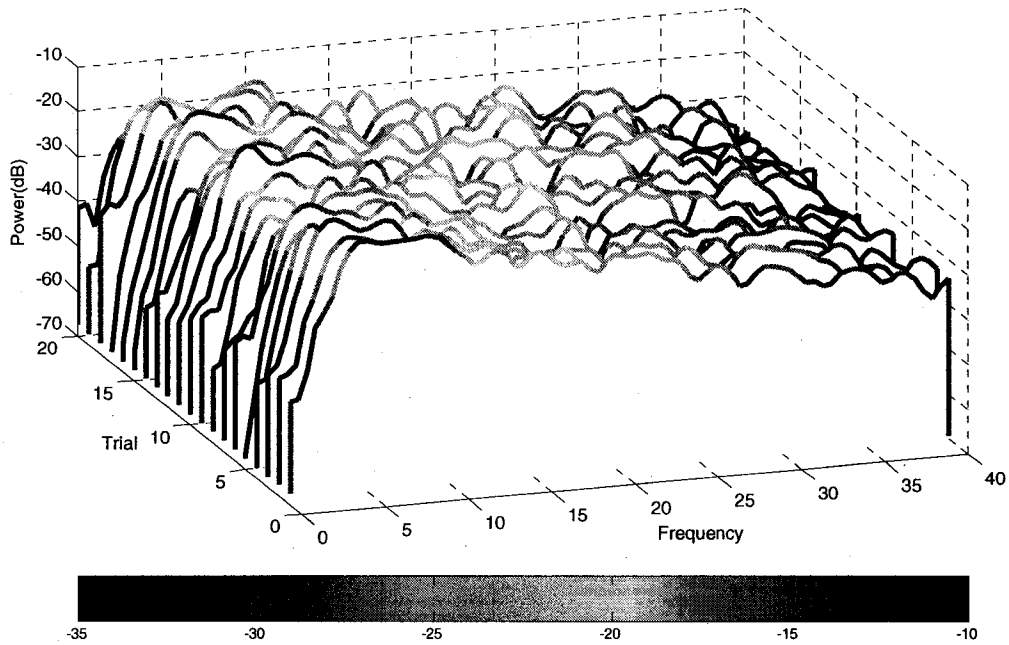

(a)

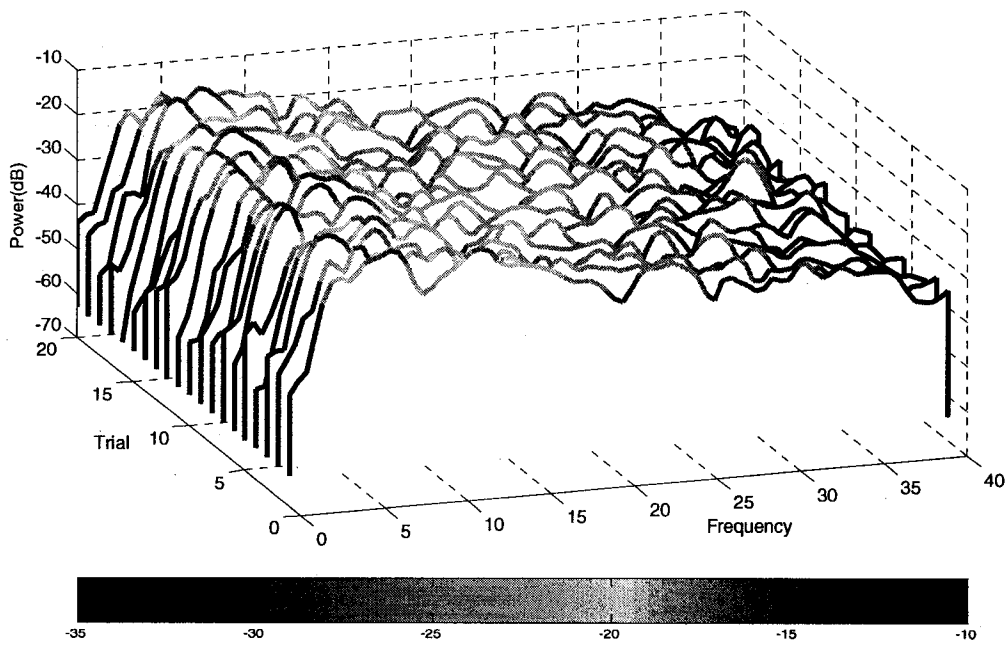

(b)

Figure 4.11 PSD Estimates vs. Trial recorded at O1, 4.0 mm from scalp.
(a) Eyes Closed **(b)** Eyes Open

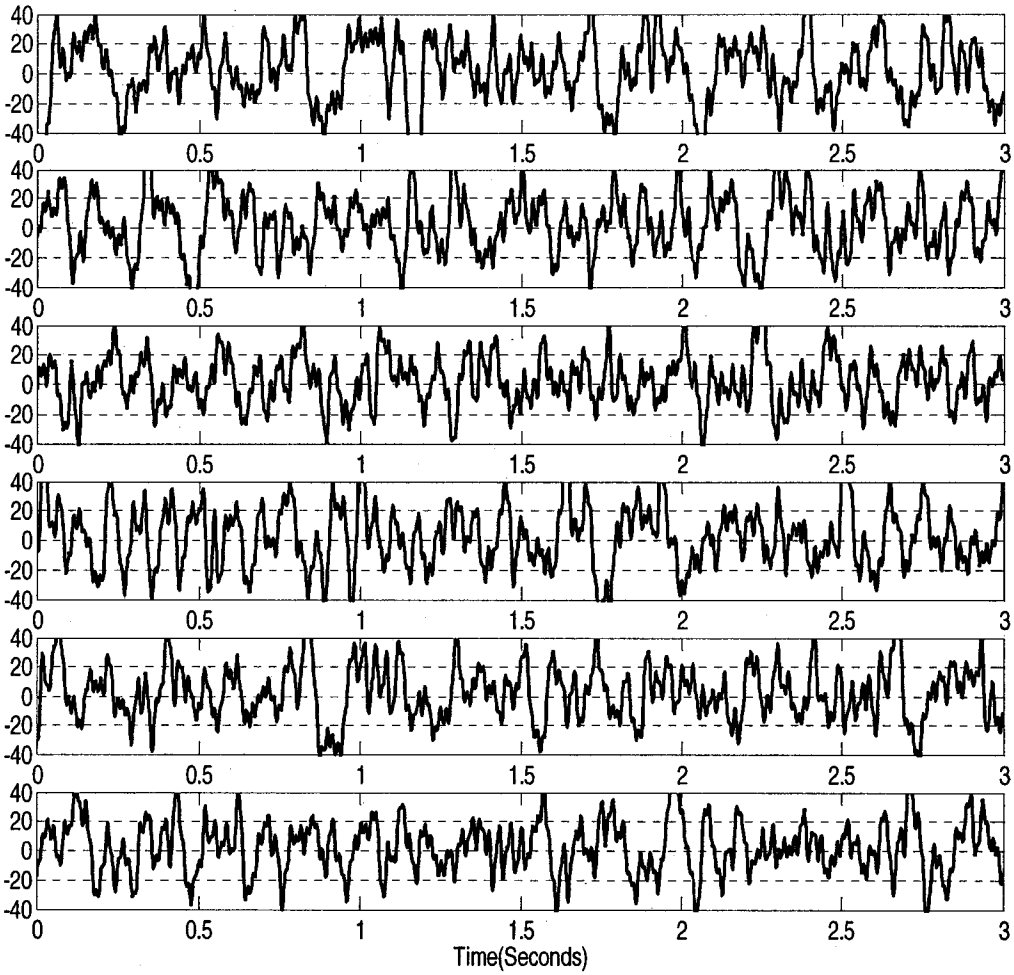

Figure 4.12 Sample time traces for 3 trials of eyes open and eyes closed data recorded at O1, 4.0 mm from scalp. From the top: eyes open trial 1, eyes closed trial 1, eyes open trial 10, eyes closed trial 10, eyes open trial 20, eyes closed trial 20.

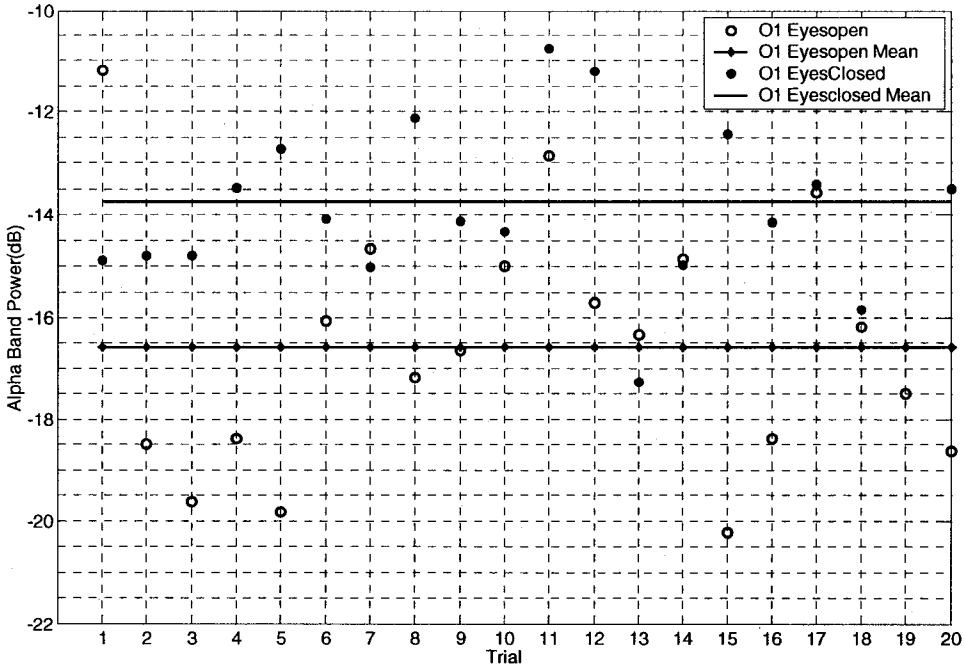

(a)

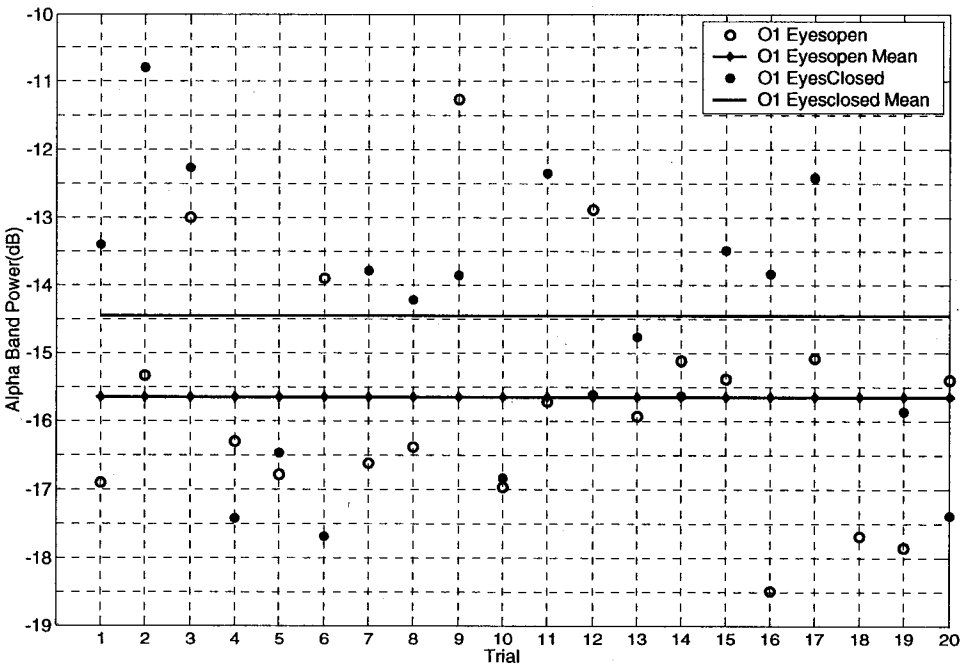

(b)

Figure 4.13 Total Alpha Band Power vs. Trial recorded at O1, 3.5 mm from scalp
(a) Training Set **(b)** Test Set

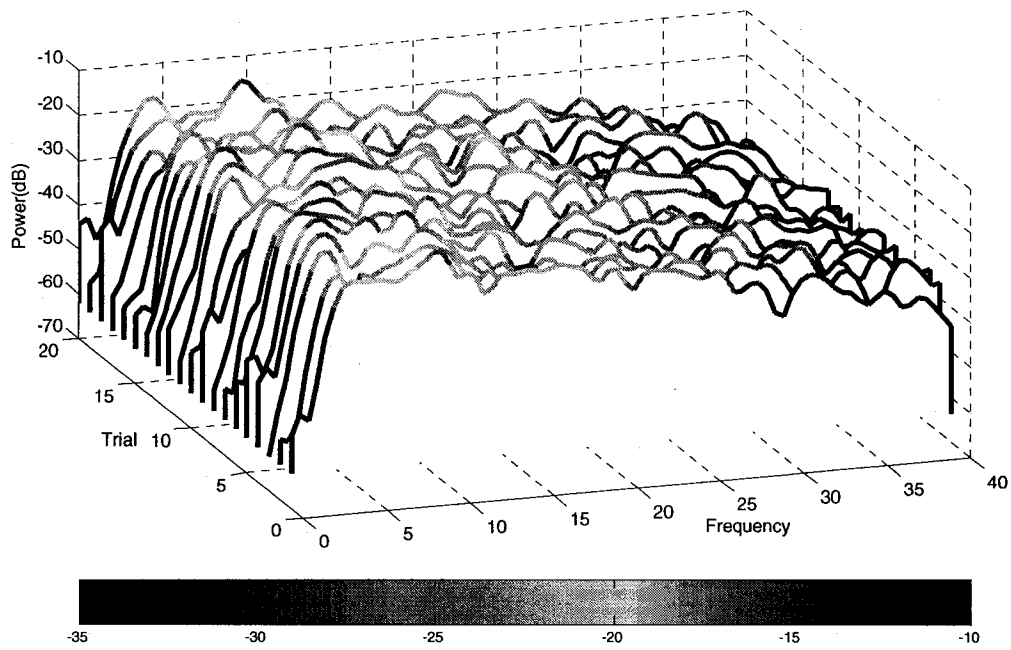

(a)

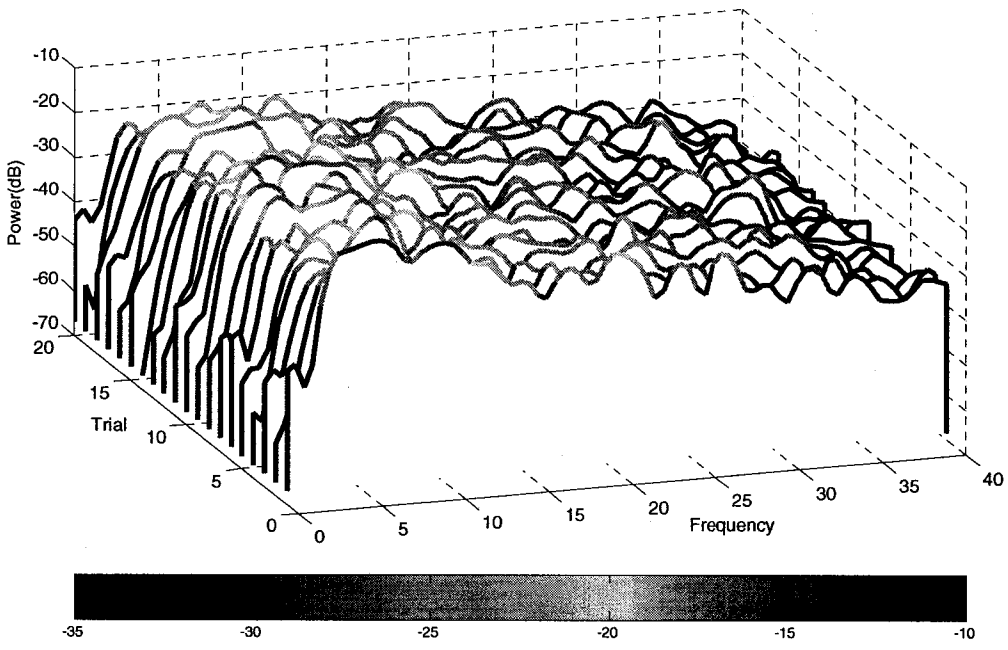

(b)

Figure 4.14 PSD Estimates vs. Trial recorded at O1, 3.5 mm from scalp.
(a) Eyes Closed **(b)** Eyes Open

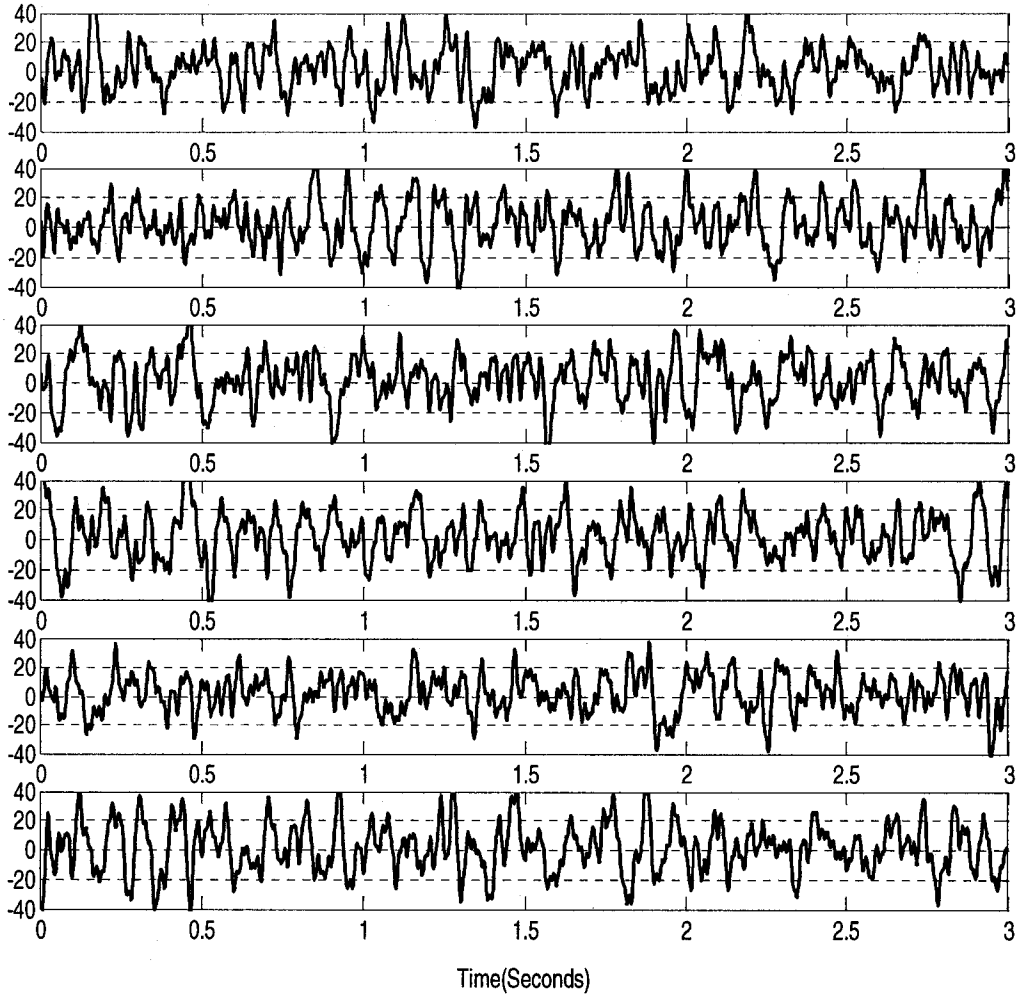

Figure 4.15 Sample time traces for 3 trials of eyes open and eyes closed data recorded at O1, 3.5 mm from scalp. From the top: eyes open trial 1, eyes closed trial 1, eyes open trial 10, eyes closed trial 10, eyes open trial 20, eyes closed trial 20.

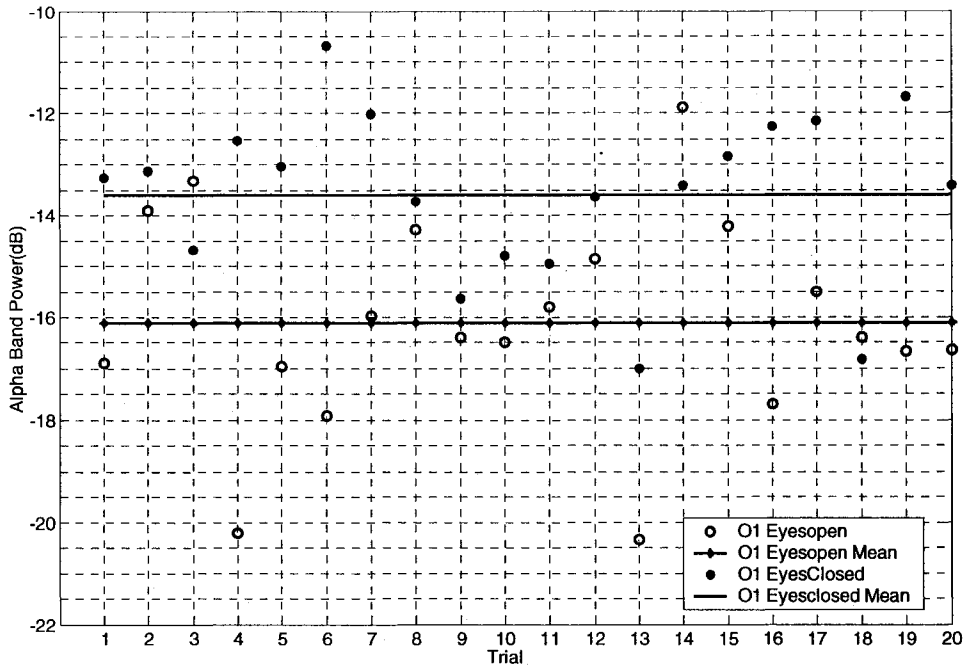

(a)

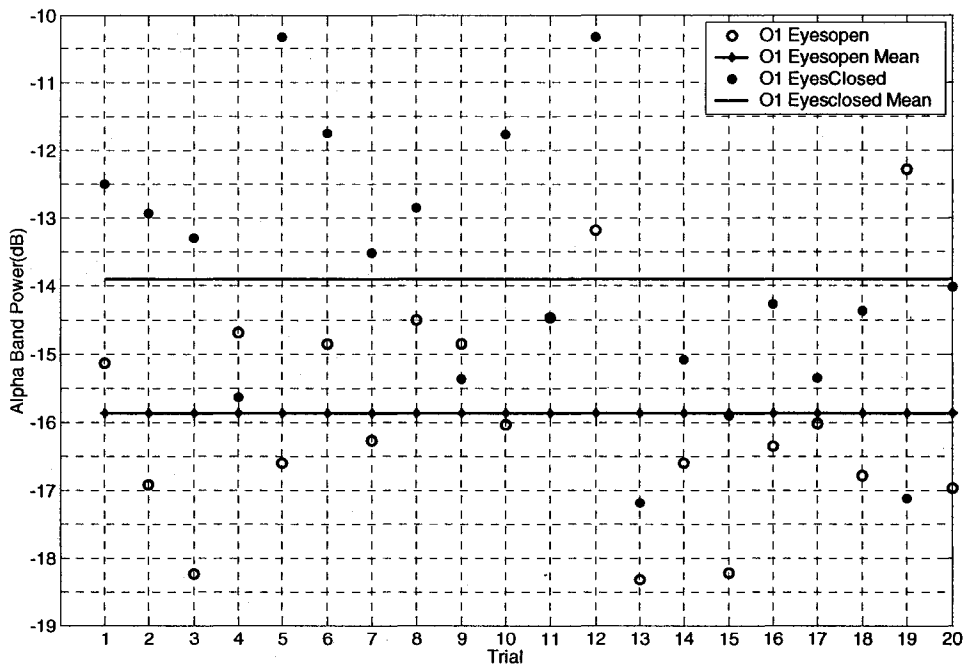

(b)

Figure 4.16 Total Alpha Band Power vs. Trial recorded at O1, 3.0 mm from scalp **(a)** Training Set **(b)** Test Set

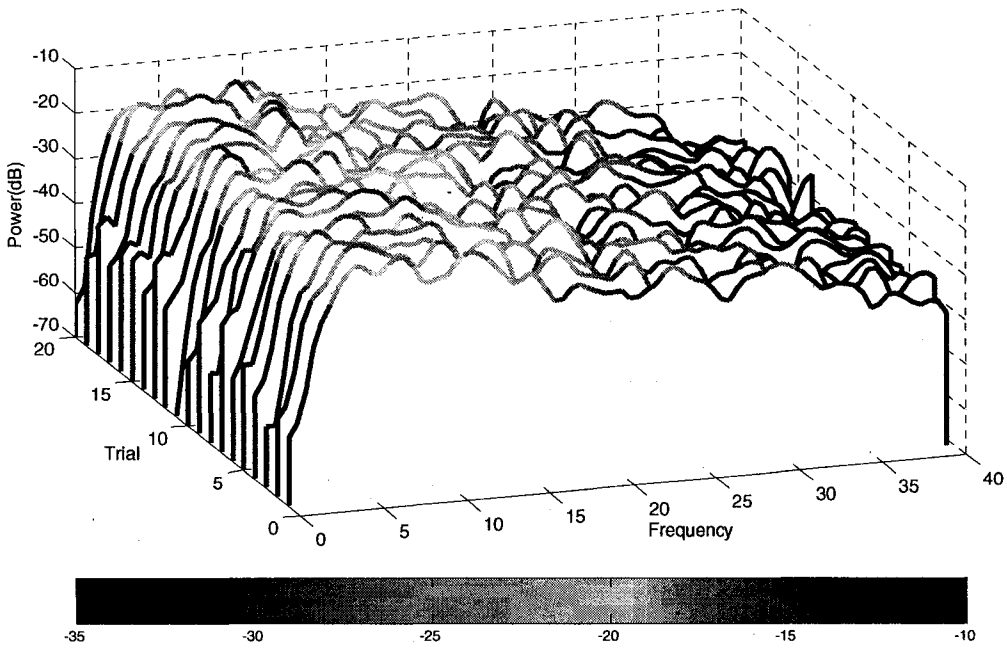

(a)

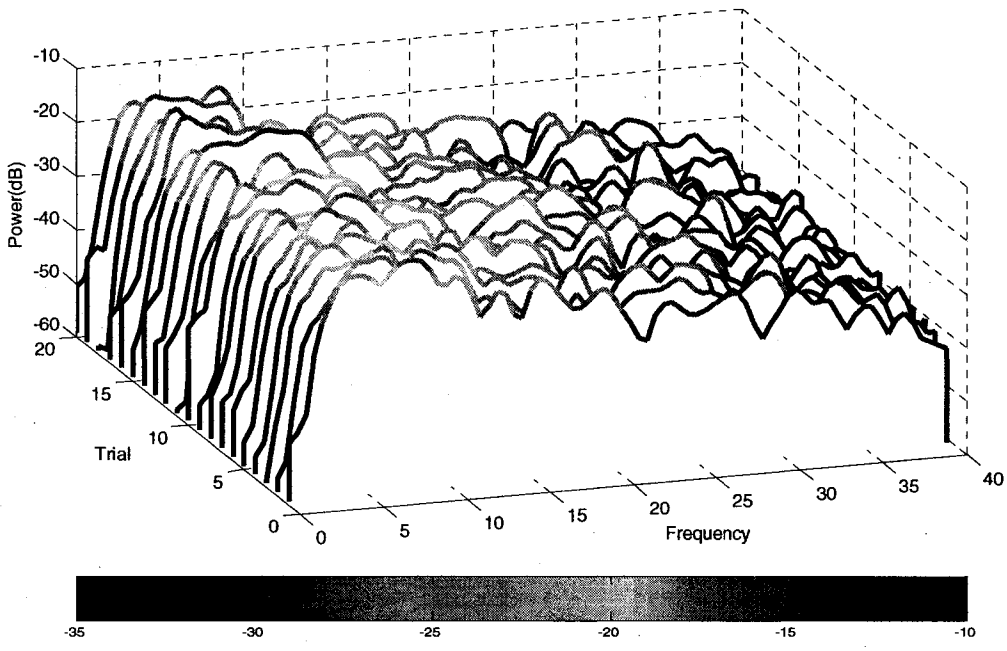

(b)

Figure 4.17 PSD Estimates vs. Trial recorded at O1, 3.0 mm from scalp.
(a) Eyes Closed **(b)** Eyes Open

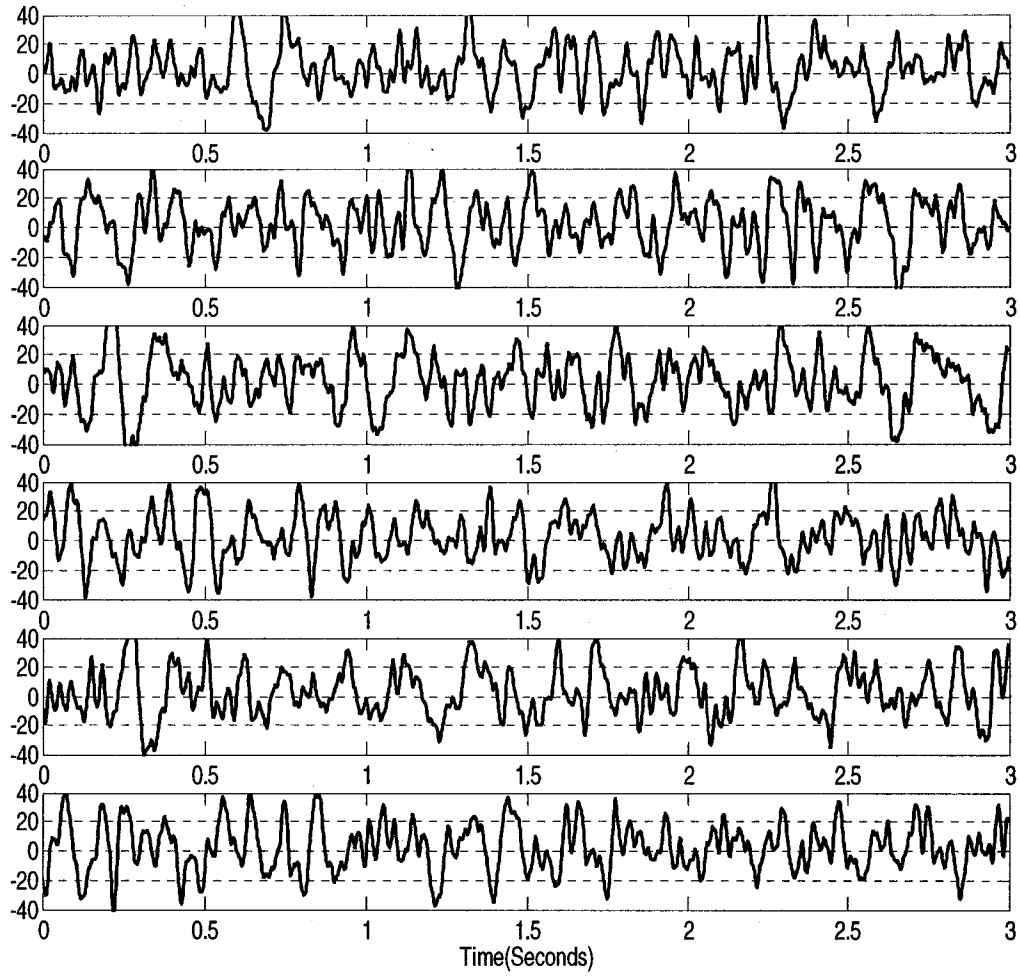

Figure 4.18 Sample time traces for 3 trials of eyes open and eyes closed data recorded at O1, 3.0 mm from scalp. From the top: eyes open trial 1, eyes closed trial 1, eyes open trial 10, eyes closed trial 10, eyes open trial 20, eyes closed trial 20.

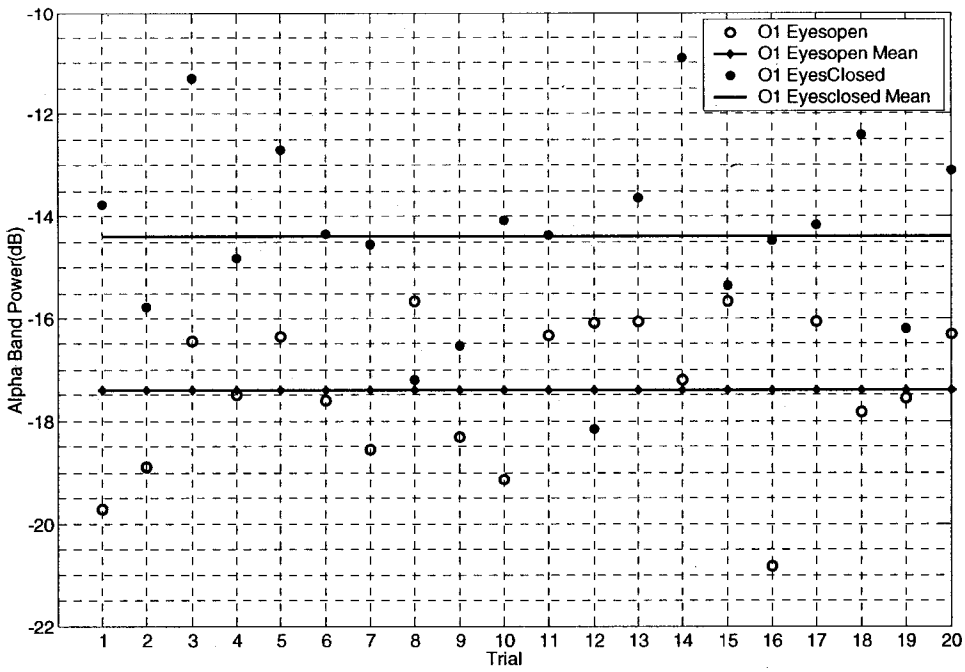

(a)

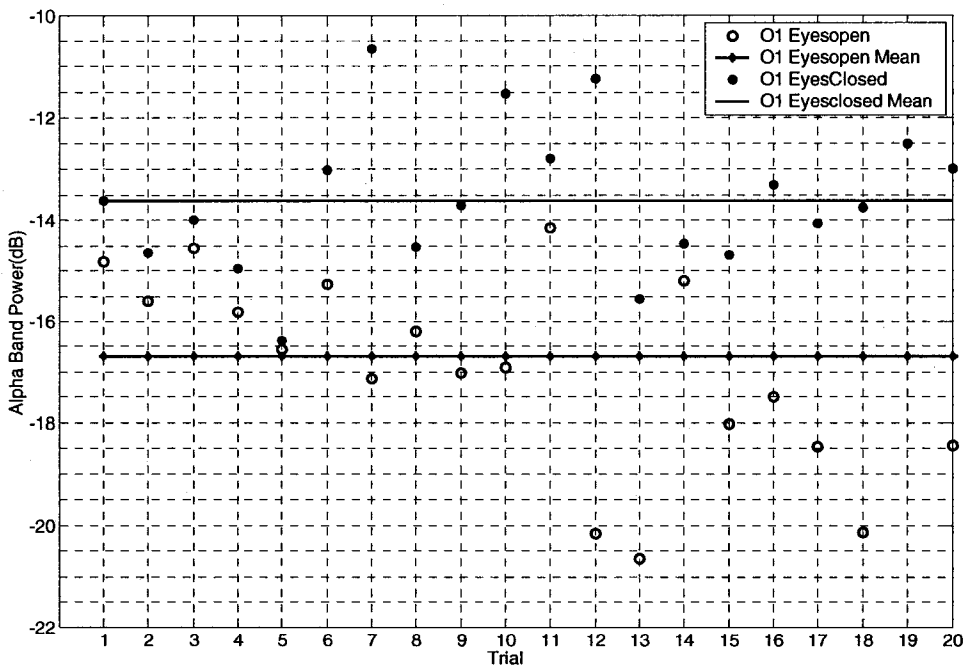

(b)

Figure 4.19 Total Alpha Band Power vs. Trial recorded at O1, 2.5 mm from scalp **(b)** Training Set **(b)** Test Set

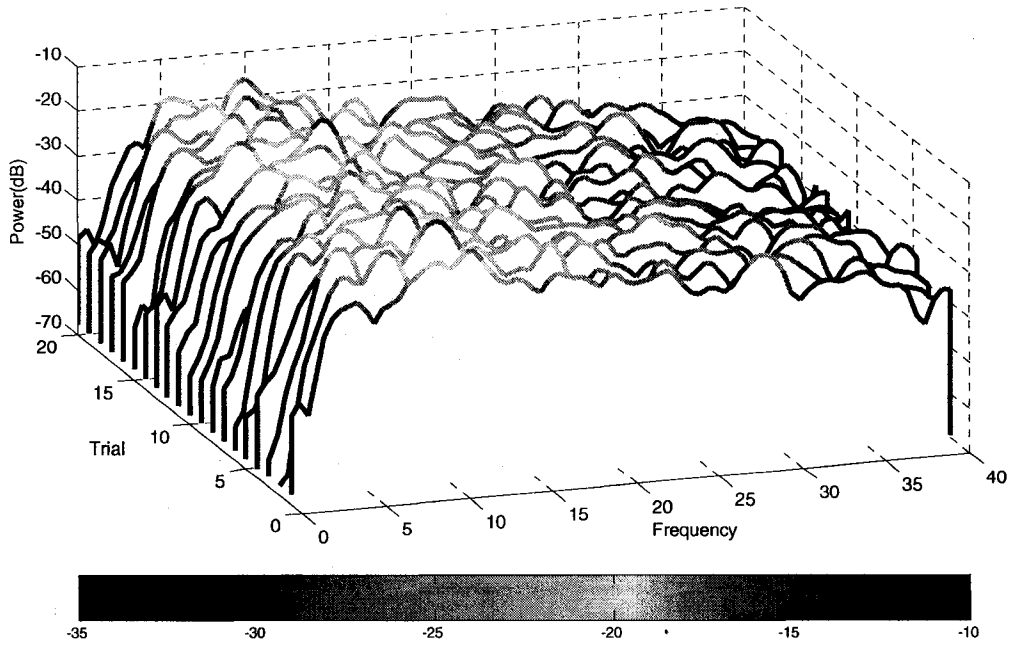

(a)

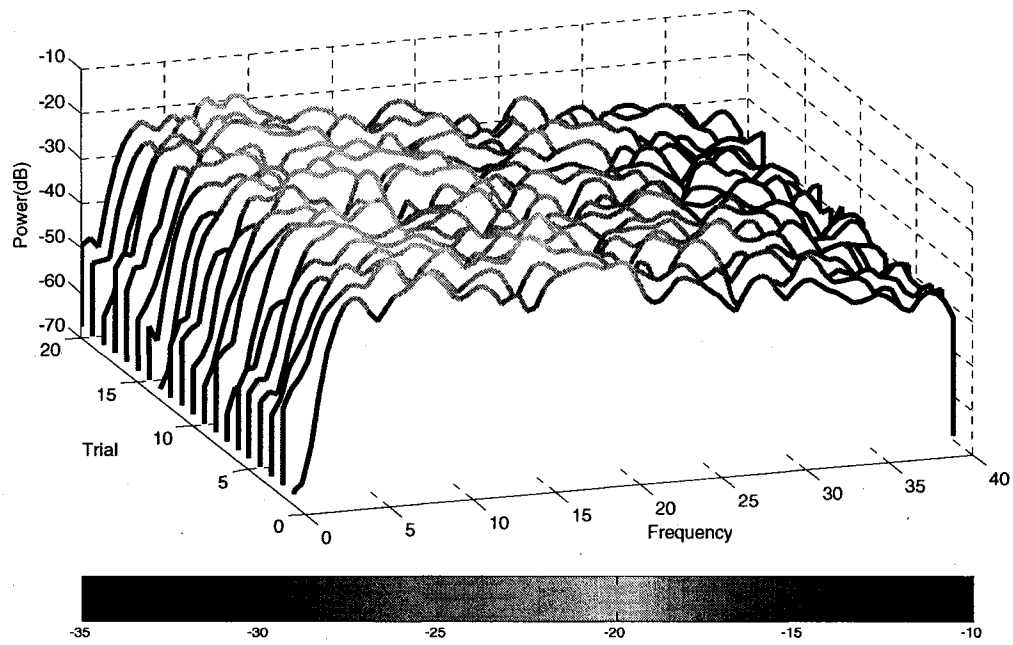

(b)

Figure 4.20 PSD Estimates vs. Trial recorded at O1, 2.5 mm from scalp.
(a) Eyes Closed **(b)** Eyes Open

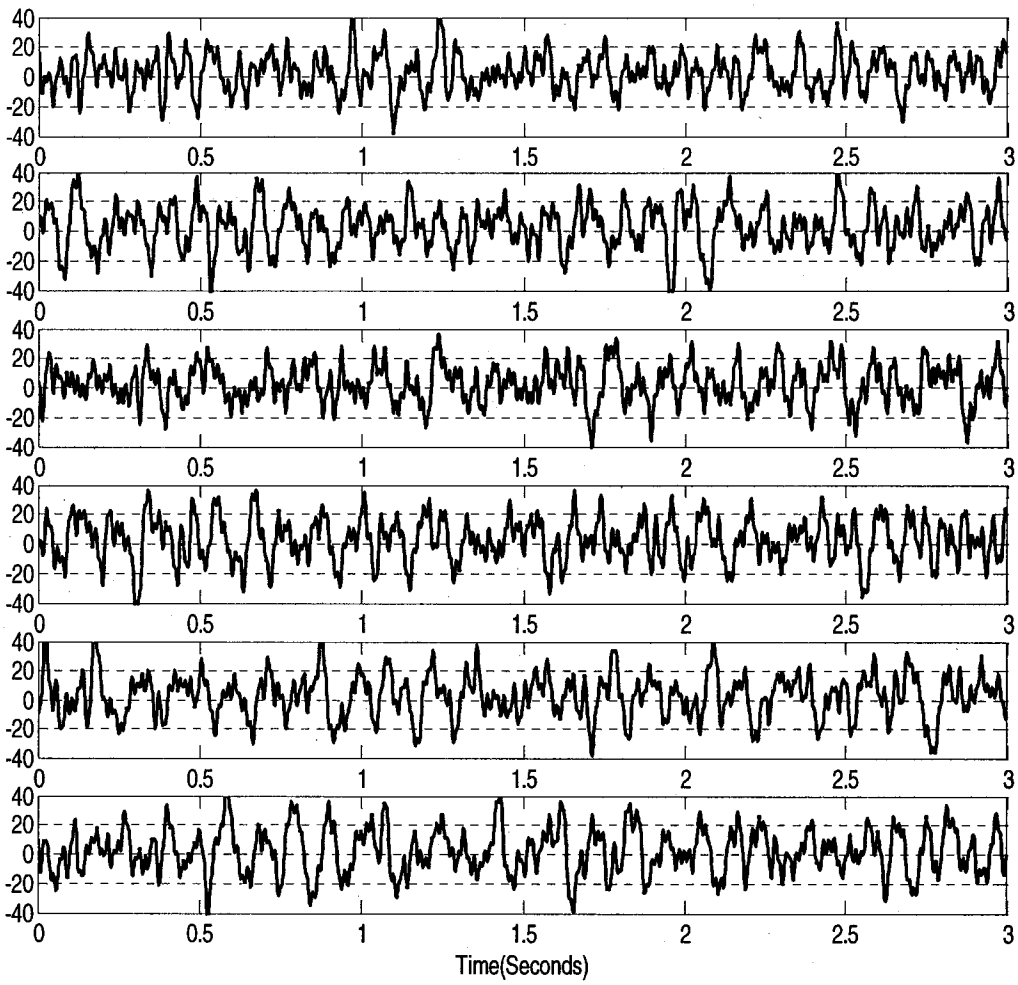

Figure 4.21 Sample time traces for 3 trials of eyes open and eyes closed data recorded at O1, 2.5mm from scalp. From the top: eyes open trial 1, eyes closed trial 1, eyes open trial 10, eyes closed trial 10, eyes open trial 20, eyes closed trial 20.

	HI @ 2.5 mm	HI @ 3.0 mm	HI @ 3.5 mm	LI @ 3.5 mm	HI @ 4.0 mm	Wet
TP	**19**	**13**	**12**	**14**	**14**	**20**
TN	**12**	**15**	**16**	**19**	**12**	**20**
FP	**8**	**5**	**4**	**1**	**8**	**0**
FN	**1**	**7**	**8**	**6**	**6**	**0**
% Correct	**77.5%**	**70%**	**70%**	**82.5%**	**65%**	**100%**

(a) Total alpha power, no overlap

	HI @ 2.5 mm	HI @ 3.0 mm	HI @ 3.5 mm	LI @ 3.5 mm	HI @ 4.0 mm	Wet
TP	**17**	**14**	**14**	**15**	**16**	**20**
TN	**15**	**17**	**15**	**20**	**10**	**20**
FP	**5**	**3**	**5**	**0**	**10**	**0**
FN	**3**	**6**	**6**	**5**	**4**	**0**
% Correct	**80%**	**77.5%**	**72.5%**	**87.5%**	**65%**	**100%**

(b) Total alpha power, 50% overlap

Table 4.2 HI and LI Probe Classification Data for total alpha power using time sample of 3 seconds. TP=true positive, TN= true negative, FP=false positive, FN=false negative (a) Without overlapping time windows (b) With 50% overlapping time windows

4.4 Motion Artifact and Differential Measurements

As one may expect, the non-contact EEG probe, due to its high sensitivity, is very susceptible to motion artifact. If the motion artifact signal has a high correlation between two closely spaced probes, most of the motion artifact can be eliminated. This section investigates the effect on the acquired EEG signal by motion artifact induced with head movement and the correlation of motion artifact in two probes located at O1 and O2. The sensitivity to alpha rhythm detection using a differential (bipolar) recording is also investigated in the same manner as the unipolar recordings documented in the previous section. Prior to testing for motion artifacts, both probes were tested for cross-talk. As a test, an input level of 50 uVrms, at 8 and 12 Hz, was injected into one channel while the other electrode was shielded. The lack of peaks in the PSD estimate of the shielded electrode indicates minimal crosstalk.

The following different head movements were investigated for motion inducing effects with both probes located at O1 and O2, 3.5mm from the scalp: forward head motion 30° in the x-z plane, backward head motion -30° in the x-z plane, and right twisting head movement 30° in the x-y plane (Z axis out top of head, x-axis out nose and y-axis out right ear). Movements from and to the upright position were approximately one second in duration The results of this investigation are documented in figures 4.23 and 4.24 along with an additional test resulting from a head tap in figure 4.24a. Data for differential recordings at O1 and O2 is documented in figures 4.25-4.29. Classification of the test data set in 4.25b is 87.5% and 67.5% for the secondary test set in figure 4.28.

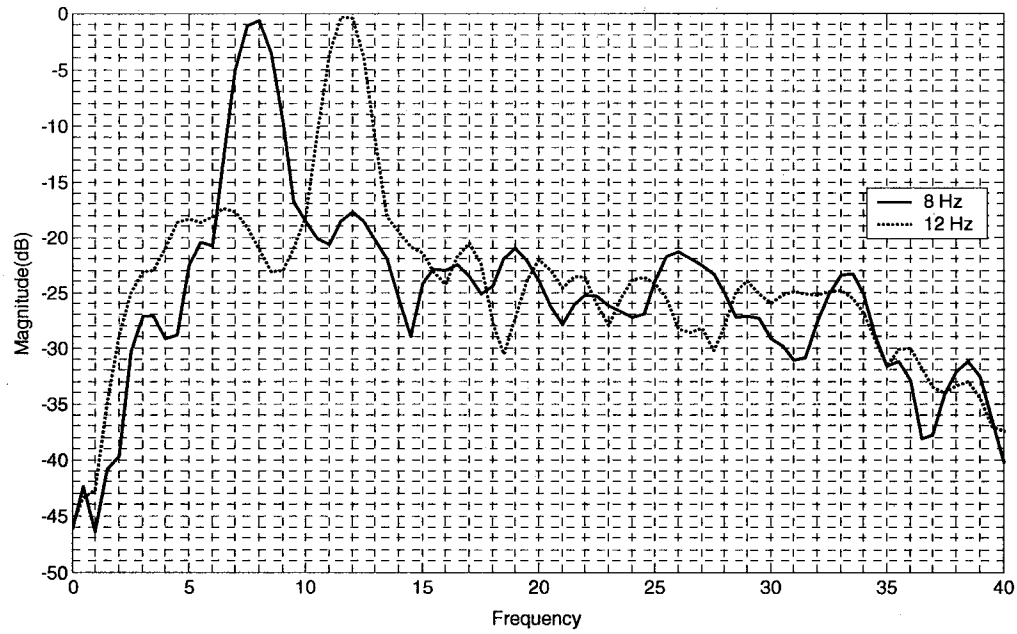

(a)

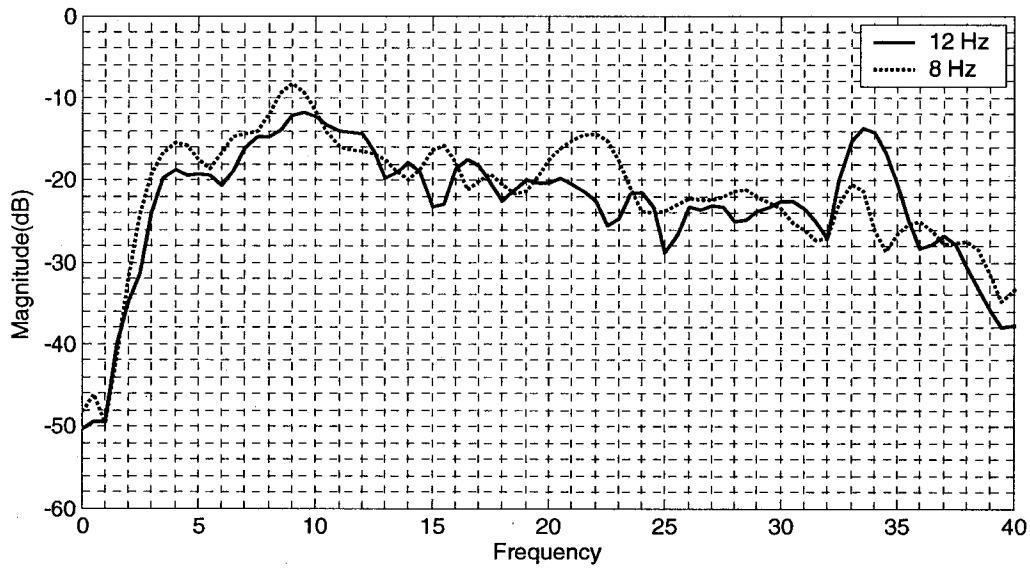

(b)

Figure 4.22 Cross-talk test for two HI probes (a) Signal probe (b) Shielded probe

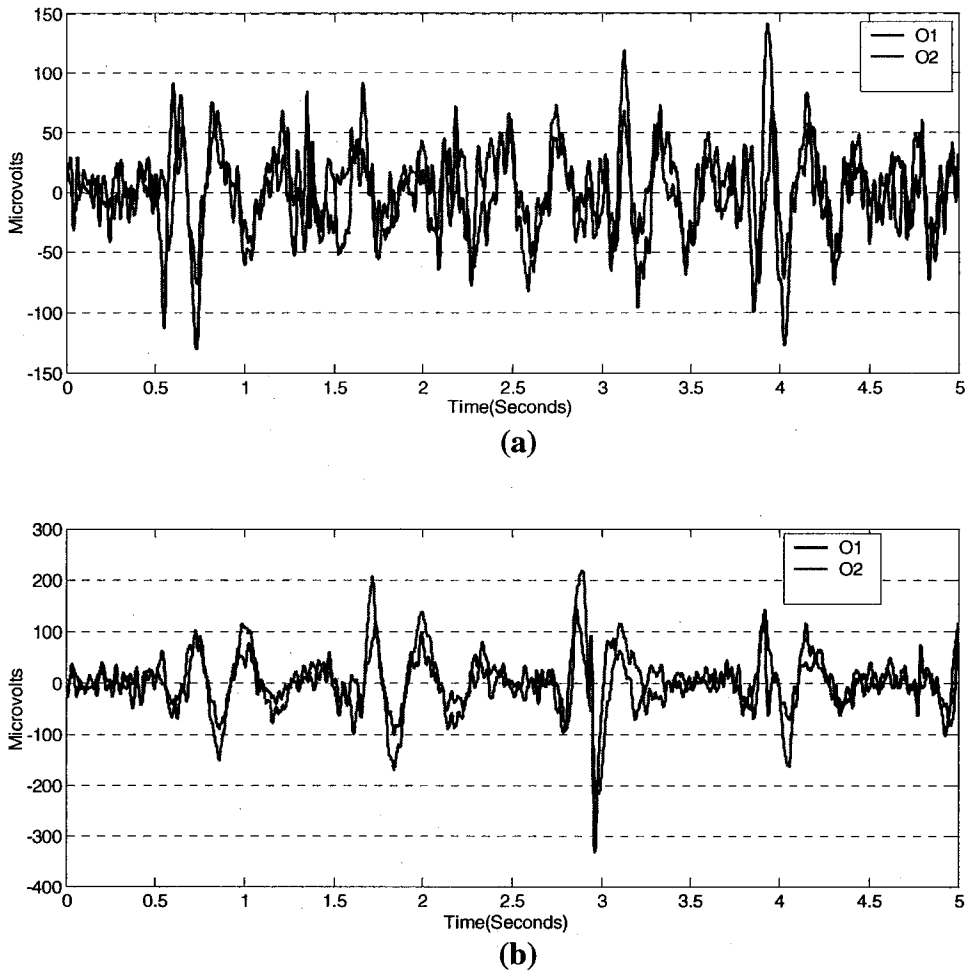

Figure 4.23 Measurement at O1 and O2 demonstrating motion artifact induced in both probes (a) Forward head movement (b) Backward head movement

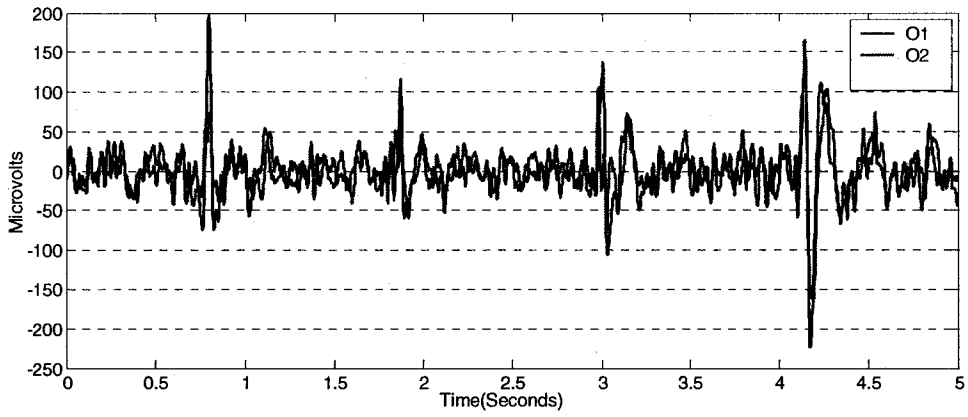

(a)

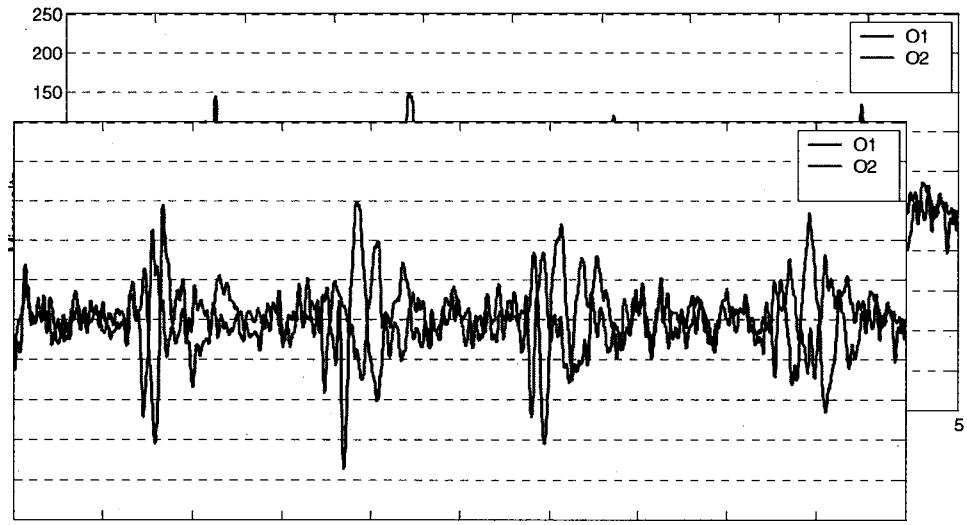

Figure 4.24 Measurement at O1 and O2 demonstrating motion artifact induced in both probes (a) Head tap (b) Right head twist

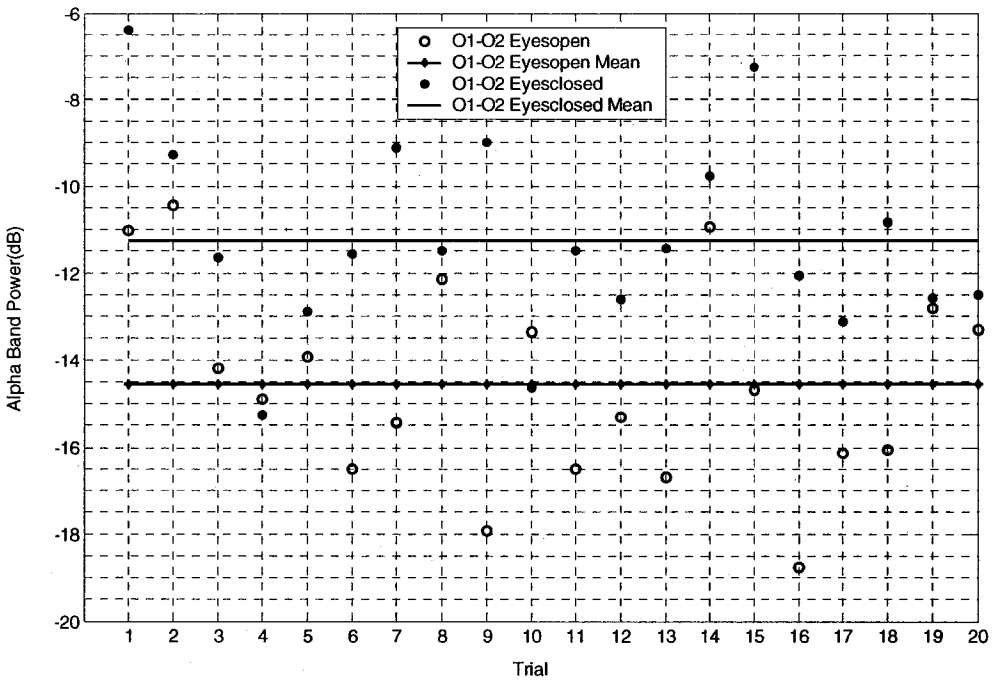

(a)

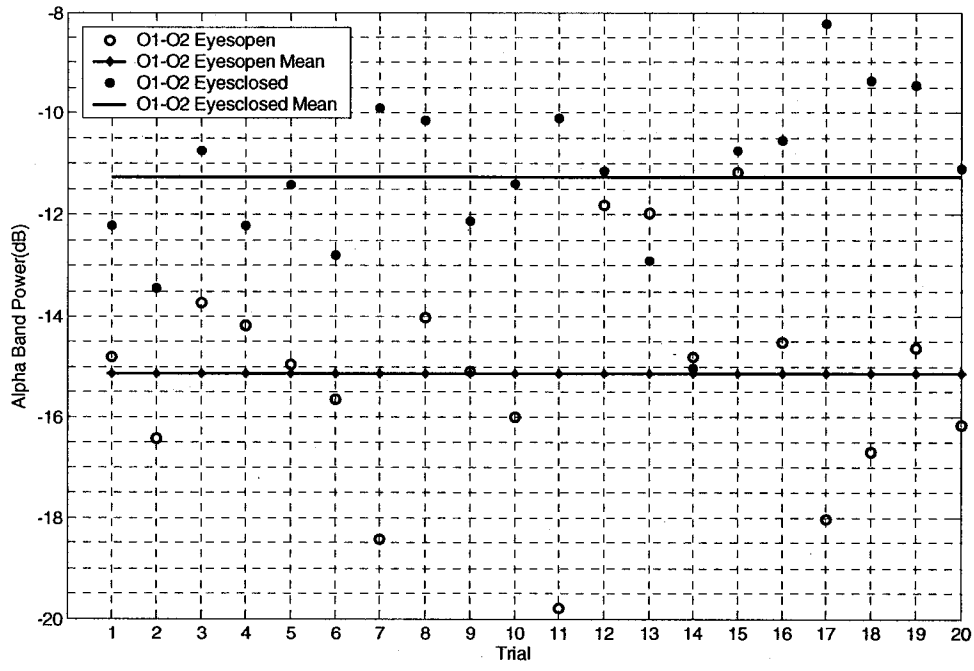

(b)

Figure 4.25 Total Alpha Band Power vs. Trial recorded differentially at O1 and O2, 3.5 mm from scalp **(a)** Training Set **(b)** Test Set

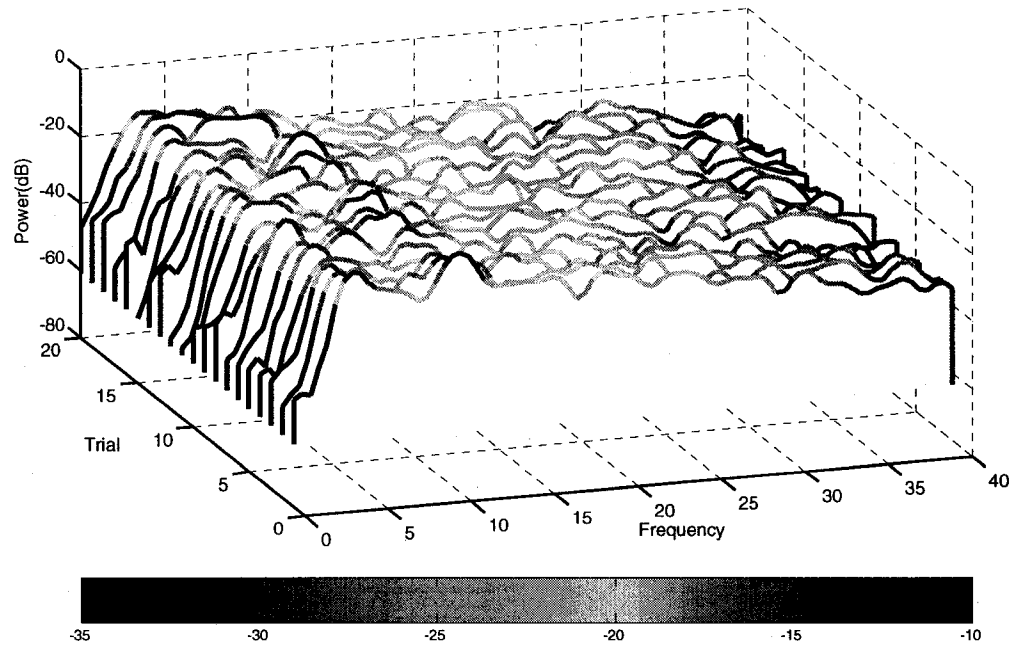

(a)

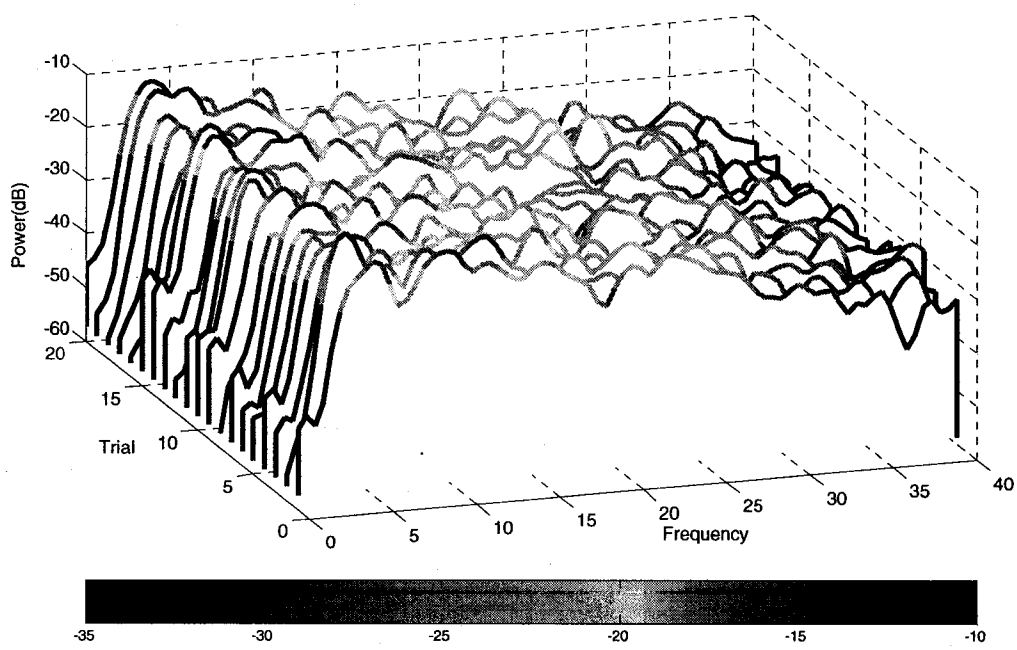

(b)

Figure 4.26 PSD Estimates vs. Trial from training set of figure 4.25a.
(a) Eyes Closed **(b)** Eyes Open

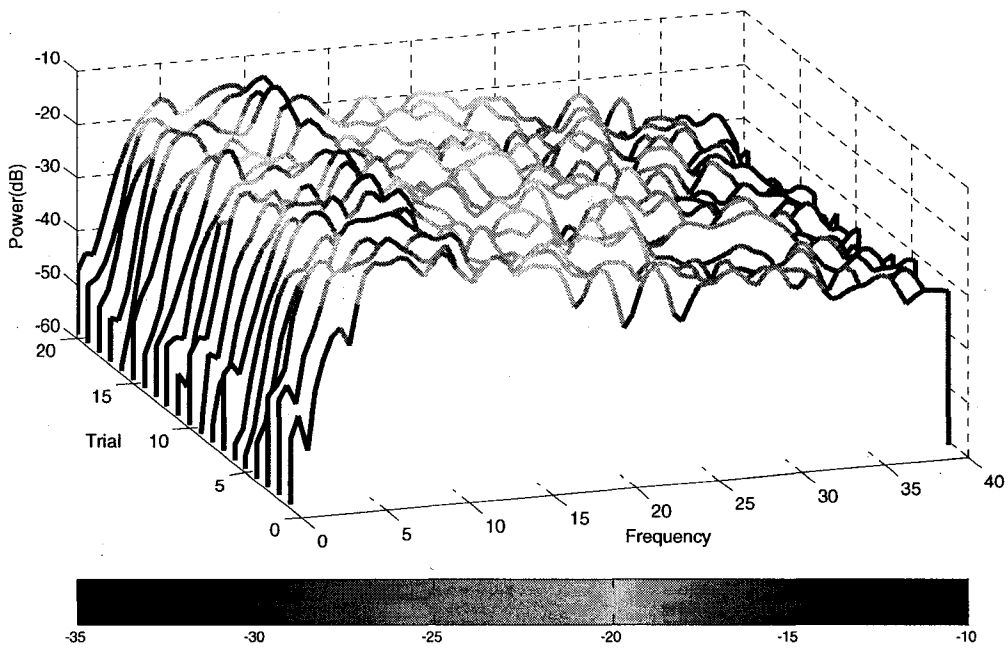

(a)

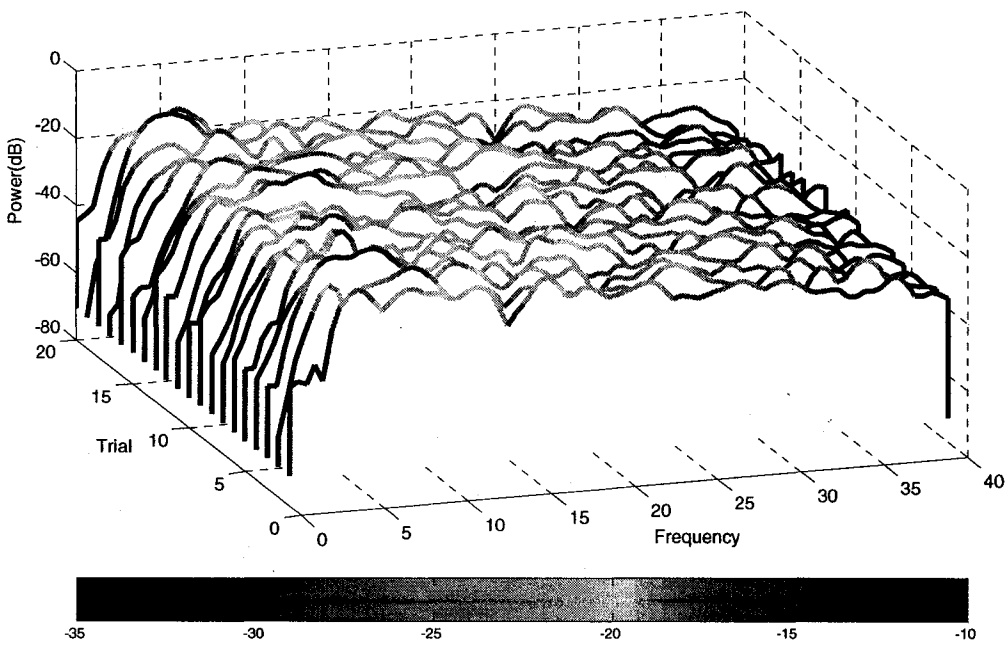

(b)

Figure 4.27 PSD Estimates vs. Trial from test set of figure 4.25b.
(a) Eyes Closed **(b)** Eyes Open

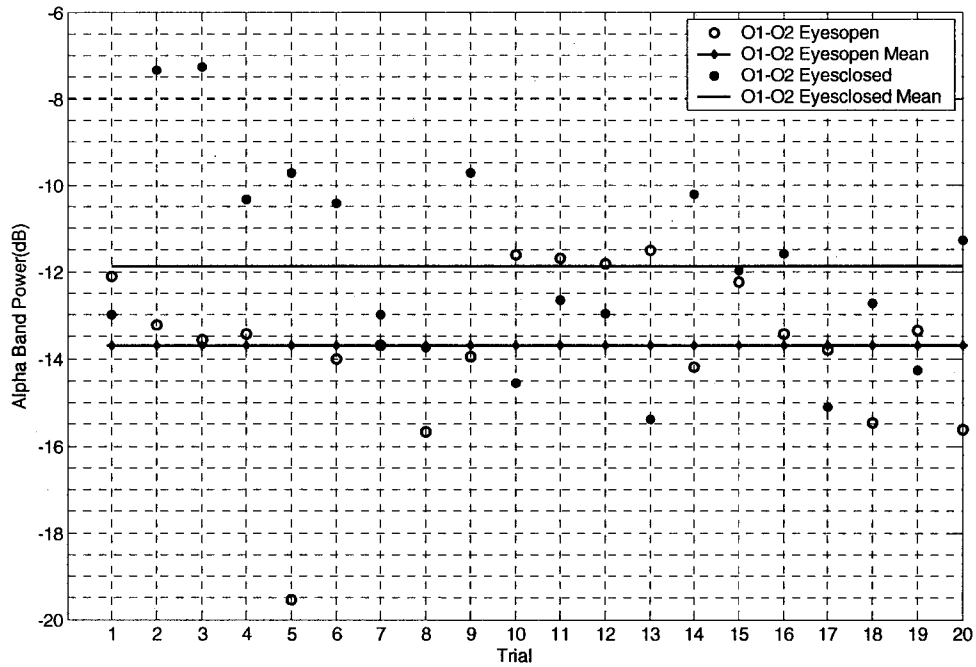

Figure 4.28 Total Alpha Band Power vs. Trial for secondary test set recorded differentially at O1 and O2, 3.5 mm from scalp.

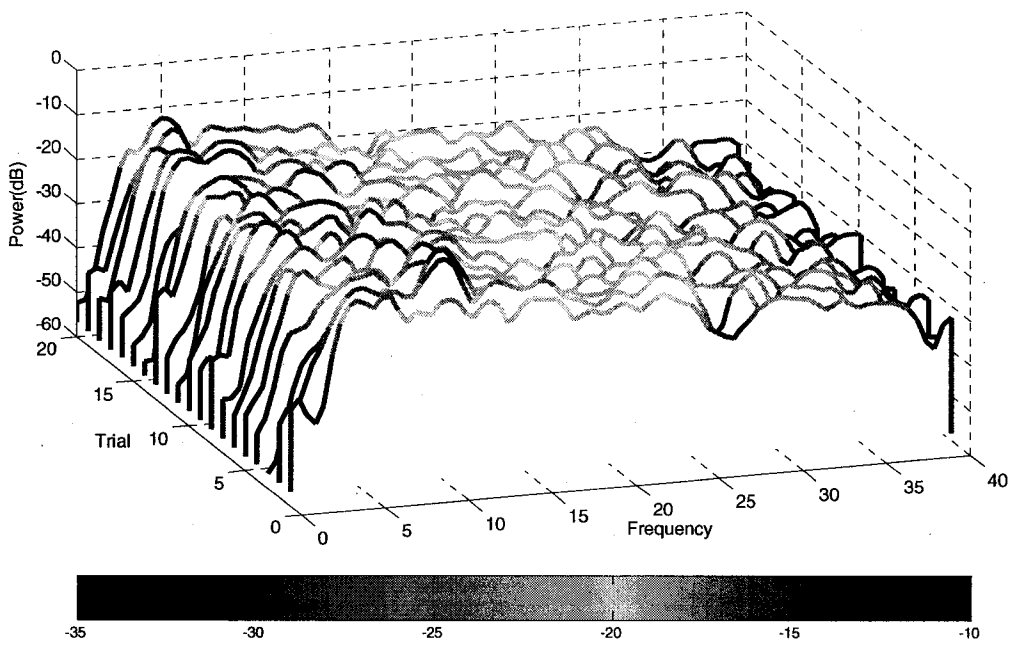

(a)

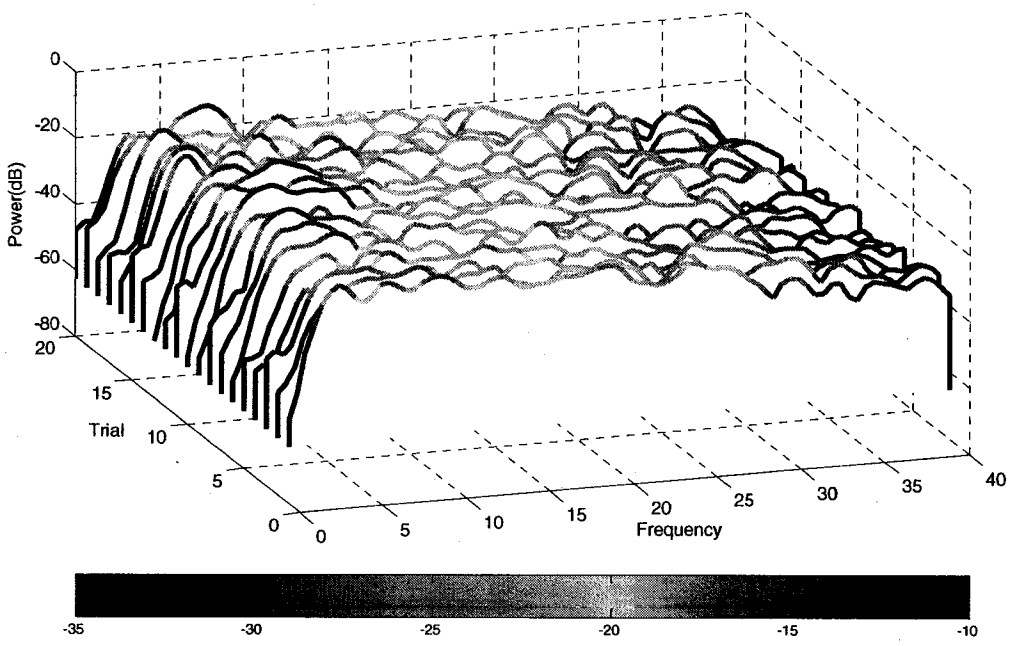

(b)

Figure 4.29 PSD Estimates vs. Trial from secondary test set of figure 4.28. **(a)** Eyes Closed **(b)** Eyes Open

CHAPTER V

DISCUSSION

5.1 Wet Electrode vs. Non-Contact Probe Performance

If the data is looked at collectively for the unipolar recordings only, there are a total of 10 data sets of 20 trials each for a total of 200 trials of non-contact alpha rhythm measurement. Out of these 200 samples, 174, or 87%, indicate an increase in alpha power with eyes closed-38 out of 40 or 95% for the LI probe and 136 out of 160 or 85% for the HI probe (documented in figures 4.7-4.21). These results, although promising, must be compared with the wet electrode trials in figures 4.4 and 4.5. As one can see, the non-contact trials show considerable variability compared to the wet electrode trials. This is due to two factors: low-frequency thermal noise, low-frequency current noise, and motion artifact. Evidence for this is shown in the PSD plots for the non-contact trials and the ECG samples of figures 4.2a and 4.3a. The PSD plots clearly show substantial power in the theta band (4-8 Hz) as compared to the wet electrode PSD plots which show minimal power in the theta band. Most of this is due to thermal and current noise but some is certainly attributable to low-frequency motion artifact as shown in figure 4.3a. Note in this figure, if compared to 4.2a, that hair is certainly a factor for motion artifact. Also note that the frequency of this artifact is approaching the alpha band (8-13 Hz) of interest, especially for the LI probe (red line in figure 4.3a) Motion artifact occurs after the QRS complex of the ECG wave which indicates artifact of cardiac origin. In fact, a pressure pulse is produced throughout the body every time the heart beats. The non-contact probes were certainly not immune to even this

small amount of motion. More than likely, this is triboelectric in origin resulting from small movement of hair fibers and is an area for further study. A reasonable approach would be to immobilize the hair fibers against the scalp using a solid spacer of the same size as the probe sensor plate. Another area of study, not mentioned in this dissertation, is the effect of hair moisture on the measurement.

Due to the variability of the non-contact measurements, the probes were further tested for repeatability by dividing the overall probe test into training and test sets in order to verify day-to-day repeatability. This type of test provides some insight into the robustness of the measurement. More specifically, it gives clues to how the measurements may change if the probe is not at the exact location as it was the prior day. The overall classification accuracy for the wet electrode, LI probe, and HI probe is documented in table 4.3. Note the following from table 4.3:

1. The wet electrode is perfect at 100%
2. The HI probe shows an increase in classification accuracy as it moves closer to scalp.
3. The LI probe shows higher classification accuracy than the HI probe at the same probe-scalp spacing.

To interpret these findings, one must keep in mind the fundamental differences in the non-contact probes and wet electrodes. The primary difference is that the wet electrode, since it makes a low ohmic contact, is inherently of lower noise than the non-contact types. In fact, the low noise is evident in the plots of figures 4.4a and 4.4b showing eyes-open power levels under -19 dB. The other distinguishing trait has to do with sensitivity to source location. The wet EEG electrode senses the potential at its location on the scalp. This potential results from

tangential current flow on the scalp surface. The actual source may exist some distance from the electrode site and some current from this distal source may flow beneath the electrode. Therefore, the measurement from the wet electrode is not localized and placement is not critical to detecting source activity. It is critical, however, to the HI non-contact probe. The only way this probe may detect any signal is if it is directly over the source. In addition, it must be over a radial source because it is most sensitive to the normal component of the electric field. As opposed to the HI probe, the LI probe "sees" a larger area of scalp since it is forcing more field lines to terminate on the probe. This is a result of maintaining the probe at the reference potential and was diagramed in figure 2.9. As a result, the classification accuracy is higher for the LI probe as compared to the HI probe. Utilizing the LI probe is difficult, however, due to its susceptibility to motion artifact and was abandoned as a reasonable approach for non-contact EEG measurement (See figures 4.2 and 4.3).

The HI probe is by no means completely immune to motion artifact. Ballistocardiographic artifact is induced in the HI probe measurement as shown in figure 4.3a. Motion artifact was investigated further and is documented in figures 4.23 and 4.24. Note from these figures that artifact generated from forward and backward head movement in figure 4.23 was more closely correlated in both channels as compared to the right head twisting motion documented in figure 4.24b that showed little correlation. There is currently no explanation for this and is suitable for further study. One approach to this problem would be to incorporate an accelerometer on the probe to determine the true forces acting on the probe. Additional alpha rhythm detection tests were performed to determine if a differential recording (bipolar) improved classification accuracy as compared to the unipolar measurements. The results improved to 87.5% from 70% with the unipolar recordings for

3.5mm scalp-probe spacing and are documented in figures 4.25-4.27. However, a secondary test set was acquired one day later and the classification accuracy reduced to 67.5%. This difference in classification accuracy is most likely due to probe placement. Additional testing with more controlled probe placement conditions is also another area for further study.

5.2 Measurement Limitations

Although the ideal recording scenario is one without any contact, this research utilized a contact on the left ear for reference. This was found to be absolutely necessary to obtain stable EEG recordings due to the low-level field strengths involved (~10μV/cm). With the reference localized on the head, the measurement of the electric field is more localized. If the reference is distal (away from the body) to the recording point (near the body), large potentials can be recorded due to stray environmental fields. This may or may not be an issue if the recordings are made differentially since most of the "noise" fields can be cancelled. In fact, differential recording using an off-body reference is possible when recording the ECG due to the large field strength. Using an off-body reference becomes especially problematic when hair exists between the probe and scalp. This could be due to stray electric fields caused by triboelectric charge generation between hair fibers.

The measurement bandwidth was maintained at 4 to 30 Hz for all recordings which was necessary to maintain reasonably low noise levels while being able to incorporate most of the EEG bandwidth. Testing in the theta band (4-8 Hz) was not attempted due to the practicality of setting up controlled experiments for it would inevitably involve sleeping subjects. As noted in chapter 2, even with a 4 Hz cut-off frequency, the theoretical signal to noise ratio for a signal level of 10uV and a source capacitance of 700 femtofarads is -7.45 dB. If current

noise is eliminated, the S/N ratio climbs just slightly to -6.28 dB so thermal noise contributes the most to the poor S/N. In fact, if the thermal noise is removed, the S/N ratio is approximately 0 dB. Therefore, future improvements to the amplifier should focus on removal of the biasing resistance. This would be approached by utilizing a switch to intermittently reset the amplifier input to maintain the amplifier in its linear range. With 30 fA of biasing current, as is the case with the OPA129, the switch may only have to be activated every minute. This switch, however, must exhibit a very high off-resistance. Note from the table below that an off-resistance of at least 10 Tohms ($10x10^{12}$) is necessary for an S/N ratio close to 0 dB. A promising implementation of this switch may be a microrelay using MEMS technology. Recently published off-resistance specifications for this type of device are more than 10 Tohms [71].

Biasing Resistance	**S/N Ratio**
500 Gohms	-7.45 dB
1 Tohm	-5.38 dB
10 Tohms	-1.8 dB
20 Tohms	-1.5 dB

Table 5.1 Signal-to-noise ratios of the high-impedance probe with 700 fF source capacitance and a 10 uVrms signal for various values of biasing resistance.

5.3 Research Summary

This dissertation has documented the successful measurement of the human alpha rhythm from the occipital region of the head without making contact at the sensing site. The measurements were made through hair at the O1 and O2 sites within 4.0mm of the scalp. There are several main points of this research that may be summarized as follows:

1. The human alpha rhythm can be detected through hair without scalp contact using commercially available electronic components at room temperature.
2. Measurements can be made with a high or low-impedance front-end amplifier.
3. The high-impedance probe is more suitable in this application being more immune to motion artifact especially when interfacing with hair.

The above results were obtained under certain limiting conditions and can be summarized as follows:

1. Measurements were made by limiting the detection bandwidth to the 4-30 Hz range thereby excluding the 0.5 to 4 Hz delta range.
2. Three seconds of data were utilized to obtain an acceptable power spectral estimate.
3. Measurements are not strictly without contact since a reference point was maintained on the left ear for measurement stability.

Several future areas of research have also been suggested:

1. Investigation of hair-electrode interface and induced noise.
2. Additional studies with more control on probe placement.
3. Additional studies to investigate motion artifact with possible utilization of accelerometer.
4. Investigating optimal methods for eliminating amplifier biasing resistance.

LIST OF REFERENCES

[1] A.Searle and L. Kirkup. "A Direct Comparison of Wet, Dry, and Insulating Bioelectric Recording Electrodes", *Physiological Measurement*, vol. 21, pp.271-283, 2000.

[2] R. Srinivasan, D. Tucker, M. Murias. "Estimating the Spatial Nyquist of the Human EEG", *Behavior Research Methods, Instruments, and Computers*,1998, 30(1), pp.8-19.

[3] L. Greischar. "Effects of Electrode Density and Electrolyte Spreading in Dense Array Electroencephalographic Recording", *Clinical Neurophysiology*, 2004, 115, pp. 710-720.

[4] A. Mendiratta. "Clinical Neurophysiology of Epilepsy", *Current Neurology and Neuroscience Reports*, 2003, 3, pp.332-340.

[5] T. Jung, S. Makeig, M. Stensmo, and T. Sejnowski. "Estimating Alertness from the EEG Power Spectrum", *IEEE Transaction on Biomedical Engineering,* 1997, 44, pp. 60-69.

[6] R. Alvarez, F. del Pozo, E. Hernando, E. Gomez, and A. Jimenez. "Real time Monitoring of the Human alertness Level", *Proceedings of SPIE*, 2003, 5102, pp.135-144.

[7] www.isnr.org

[8] Special Issue on Brain-Machine Interfaces, *IEEE Transactions in Biomedical Engineering*, vol. 51, pp.881-1081, June 2004.

[9] http://www.wadsworth.org/resnres/wolpaw.htm

[10] S.K.L. Lal and A. Craig. "Electroencephalography Activity Associated with Driver Fatigue: Implications for a Fatigue Countermeasure Device", *Journal of Psychophysiology*, 2001, 15, pp. 183-189.

[11] S.K.L. Lal, A. Craig, P. Boord, L. Kirkup, and H. Nguyen. "Development of an Algorithm for an EEG-based Driver Fatigue Countermeasure", *Journal of Safety Research*, 2003, 34, pp. 321-328.

[12]B. Taheri, "An Active Micromachined Scalp Electrode array for EEG Signal Recording", Ph.D. dissertation, University of California Davis,1994.

[13] B. Taheri, R.T. Knight, R.L. Smith. "A Dry Electrode for EEG Recording", *Electroencephalography and Clinical Neurophysiology*, 1994, 90, pp.376-383.

[14] B. Taheri, R.T. Knight, R.L. Smith. "An Active, Microfabricated, Scalp Electrode array for EEG Signal Recording", *Sensors and Actuators*, 1996, 54, pp.606-611.

[15] D. Cohen. "Magnetoencephalography: detection of the Brain's Electrical Activity with a Superconducting Magnetometer, *Science*, 1972,175, pp. 664-666.

[16] D. Cohen, E. Halgren. Magnetoencephalography (Neuromagnetism), Encyclopedia of Neuroscience, 3rd edition 2003, Elsevier.

[17] A. Lopez, P.C. Richardson. "Capacitive Electrocardiographic and Bioelectric Electrodes", *IEEE Transactions in Biomedical Engineering*, 1969,16, page 99.

[18] A. Potter, L Menke. "Capacitive Type of Biomedical Electrode", *IEEE Transactions in Biomedical Engineering*, 1970, 17, pp. 350-351.

[19] C.H. Lagow, K. J. Sladek, P.C. Richardson. "Anodic Insulated Tantalum Oxide Electrocardiograph Electrodes", *IEEE Transactions in Biomedical Engineering*, 1971, 18, pp.162-164.

[20] R.M. David, W.M. Portnoy. "Insulated Electrocardiogram Electrodes", *Medical and Biological Engineering*, 1972, 10, pp. 742-751.

[21] www.egi.com

[22] NIH Grant Number 5R44MH055410-03, 1999.

[23] Geodesic Sensor Net Technical Manual, Electrical Geodesics, Inc., Nov 17, 2004, pg. 75.

[24] A.J. Clippingdale, R.J. Prance, T.D. Clark, H. Prance, and T.P. Spiller. "Ulta-High Impedance Voltage probes and Non-Contact Electrocardiography", Sensors: Technology, Systems and Applications, K.T. V. Gratttan editor, Hilger 1991, pp. 469-472.

[25] http://www.sussex.ac.uk/Units/pei/main/research/f_bodyelectrodynamics.shtml

[26] A.J. Clippingdale, R.J. Prance, T.D. Clark, C. Watkins. "Ultrahigh Impedance Capacitively Coupled Heart Imaging array", *Review of Scientific Instruments*, vol. 65, pp. 269-270, 1994.

[27] C.J. Harland, T.D. Clark, R.J. Prance. "Remote Detection of Human Electroencephalograms Using Ultrahigh Input Impedance Electric Potential Sensors", *Applied Physics Letters*, vol. 81, pp.3284-3286, 2002.

[28] R.J. Prance, A. Debray, T.D. Clark, H. Prance, M. Nock, C.J. Harland, A.J. Clippingdale. "An Ultra-Low-Noise Electrical Potential Probe for Human-Body Scanning", *Measurement Science and Technology*, vol. 11, pp. 291-297, 2000.

[29] C.J. Harland, T.D. Clark, R.J. Prance. "Electric Potential probes- New Directions in the Remote Sensing of the Human Body", *Measurement Science and Technology,* vol. 13, pp. 163-169, 2002.

[30] http://www.srico.com/

[31] S.A. Kingsley, S. Sriram, A. Pollick, and J. Marsh. "Photrodes for Physiological Sensing", *Proceedings of SPIE*, vol. 5317, pp. 158-166, 2004.

[32] .A. Kingsley, S. Sriram, A. Pollick, and J. Marsh. "Revolutionary Optical Sensor for Physiological Monitoring in the Battlefield", *Proceedings of SPIE*, vol. 5403, pp. 68-77, 2004.

[33] United States Patent Number 6,871,084. March 22, 2005

[34] Hole, J.W., Human Anatomy and Physiology, 5th ed., Wm. C. Brown, pp. 346-349, 1990.

[35] Kandel, E.R., Schwartz, J.H., Jessell, T.M.(eds.), Principles of Neural Science, 3rd ed., Appleton & Lange, pp. 18-22, 1991.

[36] Ibid, pp.123-243.

[37] Guyton, A.C., Hall J.E., Textbook of Medical Physiology, 10th ed., W.B. Saunders, 2000.

[38] Hole, J.W., Human Anatomy and Physiology, 5th ed., Wm. C. Brown, pp. 386-387, 1990.

[39] Nunez, P.L., Neocortical Dynamics and Human EEG Rhythms, New York: Oxford University Press, pg. 105, 1995.

[40] Kandel, E.R., Schwartz, J.H., Jessell, T.M.(eds.), Principles of Neural Science, 3rd ed., Appleton & Lange, pg. 292, pg. 779, 1991.

[41] Lopes da Silva, F., Rotterdam, A.V., Biophysical Aspects of EEG and Magnetoencephalogram Generation. In Niedermeyer, E., Lopes da Silva, F.(eds.), Electroencephalography: Basic Principles, Clinical Applications and Related Fields, 5th Edition, Lippincott Williams and Wilkins, pp. 107-108, 2005.

[42] Nunez, P.L., Electric Fields of the Brain: The Neurophysics of the EEG, New York: Oxford University Press, pp. 20-21, 1981.

[43] Cooper, R., Winter, A.L., Crow, H.J., Walter, W.G., "Comparison of Subcortical, Cortical and Scalp Activity Using Chronically Indwelling Electrodes in Man", *Electroencephalography and Clinical Neurophysiology*, Vol. 18, pp. 217-228, 1965.

[44] Nunez, P.L., Electric Fields of the Brain: The Neurophysics of the EEG, New York: Oxford University Press, pp. 164-168, 1981.

[45] Lopes da Silva, F., Rotterdam, A.V., Biophysical Aspects of EEG and Magnetoencephalogram Generation. In Niedermeyer, E., Lopes da Silva, F.(eds.), Electroencephalography: Basic Principles, Clinical Applications and Related Fields, 5th Edition, Lippincott Williams and Wilkins, pp. 107-108, 2005.

[46]Nunez, P.L., Mind, Brain, and Electroencephalography. In Nunez, P.L.(ed.), Neocortical Dynamics and Human EEG Rhythms, New York: Oxford University Press, pg. 158-161, 1995.

[47] Lopes da Silva, F., Rotterdam, A.V., Biophysical Aspects of EEG and Magnetoencephalogram Generation. In Niedermeyer, E., Lopes da Silva, F.(eds.), Electroencephalography: Basic Principles, Clinical Applications and Related Fields, 5th Edition, Lippincott Williams and Wilkins, pg. 167, 2005.

[48] Nunez, P.L., Mind, Brain, and Electroencephalography. In Nunez, P.L.(ed.), Neocortical Dynamics and Human EEG Rhythms, New York: Oxford University Press, pg. 181-186, 1995.

[49] Lopes da Silva, F., Rotterdam, A.V., Biophysical Aspects of EEG and Magnetoencephalogram Generation. In Niedermeyer, E., Lopes da Silva, F.(eds.), Electroencephalography: Basic Principles, Clinical Applications and Related Fields, 5th Edition, Lippincott Williams and Wilkins, pg. 170, 2005.

[50] Ibid., pg.174

[51] Ibid., pg.169

[52] D. Halliday, R. Resnick, Fundamentals of Physics, 2nd Edition, John Wiley & Sons, Inc., pg 422, 1981.

[53] F.M. Serry, K. Kjoller, J.T. Thornton, R.J. Tench, and D. Cook. "Electric Force Microscopy, Surface Potential Imaging, and Surface Electric Modification with the Atomic Force Microscope(AFM)", Veeco Instruments Inc., Application Note 27, 2004.

[54] A.N. Cleland and M.L. Roukes, "A nanometer-scale mechanical electrometer", *Nature*, Vol. 392, pp. 160-162, 1998.

[55] L. Duvillaret, S. Rialland, and J.L. Coutaz, "Electro-optic sensors for electric field measurement. I. Theoretical comparison among different modulation techniques", *Journal of Optical Society of America*, Vol. 19, No. 11, pp 2692-2702, 2002.

[56] D.M. Taylor, P.E. Secker, Industrial Electrostatics: Fundamentals and Measurements, Research Studies Press Ltd., pg. 130-131, 1994.

[57] Ibid., pp. 136-153.

[58]] R. Srinivasan, D. Tucker, M. Murias. "Estimating the Spatial Nyquist of the Human EEG", *Behavior Research Methods, Instruments, and Computers*, 1998, 30(1), pp.8-19.

[59] www.ohmcraft.com

[60] OPA129 Data Sheet, Burr-Brown, July, 1994.

[61] AD549 Data Sheet, Analog Devices, 2005.

[62] OPA129 Data Sheet, Burr-Brown, July, 1994.

[63] OPA129 Data Sheet, Burr-Brown, July, 1994.

[64] www.ohmcraft.com, High Resistance Chip Resistors, 2004.

[65] Nunez, P.L., Electric Fields of the Brain: The Neurophysics of the EEG, New York: Oxford University Press, pg. 28, 1981.

[66] H.H. Jasper. "The Ten-Twenty Electrode System of the International Federation", *Electroencephalography and Clinical Neurophysiology*, vol. 10, pp. 371-375, 1958.

[67] J. Malmivuo and R. Plonsey, Bioelectromagnetism, Oxford University Press, pg. 259, 1995.

[68] R.G. Lyons, Understanding Digital Signal Processing, Prentice Hall, pg. 93, 2001.

[69] OPA129 Data Sheet, Burr-Brown, July, 1994.

[70] L. K. Baxter, Capacitive Sensors: Design and Applications, Institute of Electrical and Electronic Engineers, Inc., pp.154-159, 1997.

[71] H.A.C. Tilmans et.al., "A Fully-Packaged Electromagnetic Microrelay", MEMS'99, Oralndo, Florida, USA, Jan. 17-21, 1999.